Title

Exploring the Early Universe and Dark Matter with the Cosmic Microwave Background

Permalink

https://escholarship.org/uc/item/88d4c0c9

Author

Spisak, Jacob Warrick

Publication Date

2024

Peer reviewed|Thesis/dissertation

UNIVERSITY OF CALIFORNIA SAN DIEGO

Exploring the Early Universe and Dark Matter with the Cosmic Microwave Background

A dissertation submitted in partial satisfaction of the
requirements for the degree Doctor of Philosophy

in

Physics

by

Jacob Warrick Spisak

Committee in charge:

Professor George Fuller, Chair
Professor Brian Keating, Co-Chair
Professor Alexey Arefiev
Professor Raphael Flauger

2024

The Dissertation of Jacob Warrick Spisak is approved, and it is acceptable in quality and form for publication on microfilm and electronically.

University of California San Diego

2024

TABLE OF CONTENTS

vi

vii

LIST OF TABLES

Lukas, you were a second mentor to me these last few years. Although I will never forgive you for getting me addicted to coffee, I will miss you coming over to my office to get an espresso and chat three times a day. You helped me transition from experimentalist to (sort-of) theorist, and really are a great friend.

To the Lindner group at the Max Planck Institute for Nuclear Physics in Heidelberg, thank you for welcoming me into your group for three months. I survived the bitter German winter through your hospitality and large quantities of German beer.

To the Physics and Astronomy departments, thank you for providing me a home for six years. I'd like to thank in particular Raphael Flauger, from whom I learned a lot about cosmology, and Karin Sandstrom, from whom I learned a lot about the interstellar medium, and to whom I am eternally grateful for buying a Tangerine tree for the balcony garden, my true love during my time at UCSD. I hope that my academic legacy will be judged not by citation count, but by the number of citrus and passionfruit harvested from the 4th floor balcony of SERF.

Thank you to all my other friends at UCSD: Zuben, Evan, Randall, and my office mates, Ryan and Dan. Randall, you were as good of a randomly selected roommate as an incoming Ph.D. candidate could ask for. Dan, you are a great teacher, and your passion for outreach and science communication is inspiring.

A special thank you goes out to my girlfriend, Melissa. You have been by my side for the extreme highs and lows of this time in my life. Even though we had to make a relationship from Los Angeles to San Diego work for nearly four years, you never failed to brighten my day. I love you, and I can't wait to start our new life together.

Finally, I want to thank my family. It is wonderful to have most of my extended family here in San Diego: my grandparents Jo, Bob, and Gudrun, my aunts and uncles Shannon and Lenny and Carole and Terry, and my cousins Jeremy and Mikaela. Thanks to my other awesome relatives scattered across the world as well: Sheri, Luke, Olivia, Maya, Frida, and David, and Tom, Em, and Charlotte. I really do have a wonderful family, and I love you all. To my brother and sister, Sam and Anna, thanks for being there for my entire life. You basically had to, but still,

I appreciate it. You've both been perfectly adequate siblings.

To mom and dad: you really are the best parents that a son could ask for. I imagine you probably knew there was a good chance I would end up in a career in science early on, and after just 23 years of school, that dream has come to pass. These six years have been some of the most rewarding, but also the most challenging, in my life, and you really supported me when I needed it most. The fact that you both stayed up until 1am the night before my defense to listen to me practice my entire talk says it all. I love you.

Chapter 2, in full, is a reprint of material that has been submitted for publication and appears in preprint as: George M. Fuller, Lukáš Gráf, Amol V. Patwardhan, and Jacob Spisak. Dark population transfer mechanism for sterile neutrino dark matter, 2024. I was the primary investigator and author of this paper.

Chapter 3, in full, is a reprint of the material as it appears in Shunsuke Adachi, Tylor Adkins, Kam Arnold, Carlo Baccigalupi, Darcy Barron, Kolen Cheung, Yuji Chinone, Kevin T. Crowley, Josquin Errard, Giulio Fabbian, Chang Feng, Raphael Flauger, Takuro Fujino, Daniel Green, Masaya Hasegawa, Masashi Hazumi, Daisuke Kaneko, Nobuhiko Katayama, Brian Keating, Akito Kusaka, Adrian T. Lee, Yuto Minami, Haruki Nishino, Christian L. Reichardt, Praween Siritanasak, Jacob Spisak, Osamu Tajima, Satoru Takakura, Sayuri Takatori, Grant Paul Teply, and Kyohei Yamada. Constraints on axionlike polarization oscillations in the cosmic microwave background with polarbear, August 2023. I was the primary investigator and author of this paper.

Chapter 4, in part, is currently being prepared for submission for publication and appears in preprint as: Nicholas Galitzki, Tran Tsan, Jake Spisak, Michael Randall, Max Silva-Feaver, Joseph Seibert, Jacob Lashner, Shunsuke Adachi, Sean M. Adkins, Thomas Alford, Kam Arnold, Peter C. Ashton, Jason E. Austermann, Carlo Baccigalupi, Andrew Bazarko, James A. Beall, Sanah Bhimani, Bryce Bixler, Gabriele Coppi, Lance Corbett, Kevin D. Crowley, Kevin T. Crowley, Samuel Day-Weiss, Simon Dicker, Peter N. Dow, Cody J. Duell, Shannon M. Duff, Remington G. Gerras, John C. Groh, Jon E. Gudmundsson, Kathleen Harrington, Masaya

Hasegawa, Erin Healy, Shawn W. Henderson, Johannes Hubmayr, Jeffrey Iuliano, Bradley R. Johnson, Brian Keating, Ben Keller, Kenji Kiuchi, Anna M. Kofman, Brian J. Koopman, Akito Kusaka, Adrian T. Lee, Richard A. Lew, Lawrence T. Lin, Michael J Link, Tammy J. Lucas, Marius Lungu, Aashrita Mangu, Jeffrey J McMahon, Amber D. Miller, Jenna E. Moore, Magdy Morshed, Hironobu Nakata, Federico Nati, Laura B. Newburgh, David V. Nguyen, Michael D. Niemack, Lyman A. Page, Kana Sakaguri, Yuki Sakurai, Mayuri Sathyanarayana Rao, Lauren J. Saunders, Jordan E. Shroyer, Junna Sugiyama, Osamu Tajima, Atsuto Takeuchi, Refilwe Tanah Bua, Grant Teply, Tomoki Terasaki, Joel N. Ullom, Jeffrey L. Van Lanen, Eve M. Vavagiakis, Michael R Vissers, Liam Walters, and Yuhan Wang. The simons observatory: Design, integration, and testing of the small aperture telescopes, 2024. I was a first-tier author of this paper.

2018	B. S. in Physics, Minor in Mathematics, Rice University
2018–2024	Graduate Teaching Assistant, Department of Physics, University of California San Diego
2018–2024	Graduate Student Researcher, Department of Physics, University of California San Diego
2024	Ph. D. in Physics, University of California San Diego

PUBLICATIONS

* Denotes lead author

* Shunsuke Adachi, Tylor Adkins, Kam Arnold, Carlo Baccigalupi, Darcy Barron, Kolen Cheung, Yuji Chinone, Kevin T. Crowley, Josquin Errard, Giulio Fabbian, Chang Feng, Raphael Flauger, Takuro Fujino, Daniel Green, Masaya Hasegawa, Masashi Hazumi, Daisuke Kaneko, Nobuhiko Katayama, Brian Keating, Akito Kusaka, Adrian T. Lee, Yuto Minami, Haruki Nishino, Christian L. Reichardt, Praween Siritanasak, Jacob Spisak, Osamu Tajima, Satoru Takakura, Sayuri Takatori, Grant Paul Teply, and Kyohei Yamada. Constraints on axionlike polarization oscillations in the cosmic microwave background with polarbear, August 2023

* George M. Fuller, Lukáš Gráf, Amol V. Patwardhan, and Jacob Spisak. Dark population transfer mechanism for sterile neutrino dark matter, 2024

* Jacob Spisak, Edison Liang, Wen Fu, and Markus Boettcher. Relativistic shear boundary layer and the gamma-ray emission of GW170817. *The Astrophysical Journal*, 903(2):120, Nov 2020

Shunsuke Adachi, Tylor Adkins, Carlo Baccigalupi, Yuji Chinone, Kevin T. Crowley, Josquin Errard, Giulio Fabbian, Chang Feng, Takuro Fujino, Masaya Hasegawa, Masashi Hazumi, Oliver Jeong, Daisuke Kaneko, Brian Keating, Akito Kusaka, Adrian T. Lee, Anto I. Lonappan, Yuto Minami, Masaaki Murata, Lucio Piccirillo, Christian L. Reichardt, Praween Siritanasak, Jake Spisak, Satoru Takakura, Grant P. Teply, and Kyohei Yamada. Exploration of the polarization angle variability of the crab nebula with polarbear and its application to the search for axion-like particles, 2024

Nicholas Galitzki, Tran Tsan, Jake Spisak, Michael Randall, Max Silva-Feaver, Joseph Seibert, Jacob Lashner, Shunsuke Adachi, Sean M. Adkins, Thomas Alford, Kam Arnold, Peter C. Ashton, Jason E. Austermann, Carlo Baccigalupi, Andrew Bazarko, James A. Beall, Sanah Bhimani, Bryce Bixler, Gabriele Coppi, Lance Corbett, Kevin D. Crowley, Kevin T. Crowley, Samuel Day-Weiss, Simon Dicker, Peter N. Dow, Cody J. Duell, Shannon M. Duff, Remington G.

Gerras, John C. Groh, Jon E. Gudmundsson, Kathleen Harrington, Masaya Hasegawa, Erin Healy, Shawn W. Henderson, Johannes Hubmayr, Jeffrey Iuliano, Bradley R. Johnson, Brian Keating, Ben Keller, Kenji Kiuchi, Anna M. Kofman, Brian J. Koopman, Akito Kusaka, Adrian T. Lee, Richard A. Lew, Lawrence T. Lin, Michael J Link, Tammy J. Lucas, Marius Lungu, Aashrita Mangu, Jeffrey J McMahon, Amber D. Miller, Jenna E. Moore, Magdy Morshed, Hironobu Nakata, Federico Nati, Laura B. Newburgh, David V. Nguyen, Michael D. Niemack, Lyman A. Page, Kana Sakaguri, Yuki Sakurai, Mayuri Sathyanarayana Rao, Lauren J. Saunders, Jordan E. Shroyer, Junna Sugiyama, Osamu Tajima, Atsuto Takeuchi, Refilwe Tanah Bua, Grant Teply, Tomoki Terasaki, Joel N. Ullom, Jeffrey L. Van Lanen, Eve M. Vavagiakis, Michael R Vissers, Liam Walters, and Yuhan Wang. The simons observatory: Design, integration, and testing of the small aperture telescopes, 2024

K. Yamada, B. Bixler, Y. Sakurai, P. C. Ashton, J. Sugiyama, K. Arnold, J. Begin, L. Corbett, S. Day-Weiss, and N. Galitzki et al. The Simons Observatory: Cryogenic half wave plate rotation mechanism for the small aperture telescopes, 2023. Submitted to RSI

Kevin D. Crowley, Peter Dow, Jordan E. Shroyer, John C. Groh, Bradley Dober, Jacob Spisak, Nicholas Galitzki, Tanay Bhandarkar, Mark J. Devlin, and Simon Dicker et al. The Simons Observatory: A large-diameter truss for a refracting telescope cooled to 1 k. *Review of Scientific Instruments*, 93(5), May 2022

Ningfeng Zhu et al. The Simons Observatory Large Aperture Telescope Receiver. *Astrophys. J. Supp.*, 256(1):23, 2021

Tran Tsan, Nicholas Galitzki, Aamir M. Ali, Kam Arnold, Gabriele Coppi, Tamar Ervin, Logan Foote, Brian Keating, Jack Lashner, and Orlowski-Scherer et al. The effects of inclination on a two stage pulse tube cryocooler for use with a ground based Observatory. *Cryogenics*, 117:103323, July 2021

Maximilian H. Abitbol, David Alonso, Sara M. Simon, Jack Lashner, Kevin T. Crowley, Aamir M. Ali, Susanna Azzoni, Carlo Baccigalupi, Darcy Barron, Michael L. Brown, Erminia Calabrese, Julien Carron, Yuji Chinone, Jens Chluba, Gabriele Coppi, Kevin D. Crowley, Mark Devlin, Jo Dunkley, Josquin Errard, Valentina Fanfani, Nicholas Galitzki, Martina Gerbino, J. Colin Hill, Bradley R. Johnson, Baptiste Jost, Brian Keating, Nicoletta Krachmalnicoff, Akito Kusaka, Adrian T. Lee, Thibaut Louis, Mathew S. Madhavacheril, Heather McCarrick, Jeffrey McMahon, P. Daniel Meerburg, Federico Nati, Haruki Nishino, Lyman A. Page, Davide Poletti, Giuseppe Puglisi, Michael J. Randall, Aditya Rotti, Jacob Spisak, Aritoki Suzuki, Grant P. Teply, Clara Vergès, Edward J. Wollack, Zhilei Xu, and Mario Zannoni. The Simons Observatory: gain, bandpass and polarization-angle calibration requirements for B-mode searches. *Journal of Cosmology and Astroparticle Physics*, 2021(5):032, May 2021

Kenji Kiuchi, Shunsuke Adachi, Aamir M. Ali, Kam Arnold, Peter Ashton, Jason E. Austermann, Andrew Bazako, James A. Beall, Yuji Chinone, Gabriele Coppi, Kevin D. Crowley, Kevin T. Crowley, Simon Dicker, Bradley Dober, Shannon M. Duff, Giulio Fabbian, Nicholas Galitzki,

Joseph E. Golec, Jon E. Gudmundsson, Kathleen Harrington, Masaya Hasegawa, Makoto Hattori, Charles A. Hill, Shuay-Pwu Patty Ho, Johannes Hubmayr, Bradley R. Johnson, Daisuke Kaneko, Nobuhiko Katayama, Brian Keating, Akito Kusaka, Jack Lashner, Adrian T. Lee, Frederick Matsuda, Heather McCarrick, Masaaki Murata, Federico Nati, Yume Nishinomiya, Lyman Page, Mayuri Sathyanarayana Rao, Christian L. Reichardt, Kana Sakaguri, Yuki Sakurai, Joseph Sibert, Jacob Spisak, Osamu Tajima, Grant P. Teply, Tomoki Terasaki, Tran Tsan, Samantha Walker, Edward J. Wollack, Zhilei Xu, Kyohei Yamada, Mario Zannoni, and Ningfeng Zhu. Simons Observatory Small Aperture Telescope overview. In *Society of Photo-Optical Instrumentation Engineers (SPIE) Conference Series*, volume 11445 of *Society of Photo-Optical Instrumentation Engineers (SPIE) Conference Series*, page 114457L, December 2020

Brian J. Koopman, Jack Lashner, Lauren J. Saunders, Matthew Hasselfield, Tanay Bhandarkar, Sanah Bhimani, Steve K. Choi, Cody J. Duell, Nicholas Galitzki, Kathleen Harrington, Adam D. Hincks, Shuay-Pwu Patty Ho, Laura Newburgh, Christian L. Reichardt, Joseph Seibert, Jacob Spisak, Benjamin Westbrook, Zhilei Xu, and Ningfeng Zhu. The Simons Observatory: overview of data acquisition, control, monitoring, and computer infrastructure. In Juan C. Guzman and Jorge Ibsen, editors, *Software and Cyberinfrastructure for Astronomy VI*, volume 11452, pages 35 − 53. International Society for Optics and Photonics, SPIE, 2020

Aamir M. Ali, Shunsuke Adachi, Kam Arnold, Peter Ashton, Andrew Bazarko, Yuji Chinone, Gabriele Coppi, Lance Corbett, Kevin D. Crowley, Kevin T. Crowley, Mark Devlin, Simon Dicker, Shannon Duff, Chris Ellis, Nicholas Galitzki, Neil Goeckner-Wald, Kathleen Harrington, Erin Healy, Charles A. Hill, Shuay-Pwu Patty Ho, Johannes Hubmayr, Brian Keating, Kenji Kiuchi, Akito Kusaka, Adrian T. Lee, Michael Ludlam, Aashrita Mangu, Frederick Matsuda, Heather McCarrick, Federico Nati, Michael D. Niemack, Haruki Nishino, John Orlowski-Scherer, Mayuri Sathyanarayana Rao, Christopher Raum, Yuki Sakurai, Maria Salatino, Trevor Sasse, Joseph Seibert, Carlos Sierra, Maximiliano Silva-Feaver, Jacob Spisak, Sara M. Simon, Suzanne Staggs, Osamu Tajima, Grant Teply, Tran Tsan, Edward Wollack, Bejamin Westbrook, Zhilei Xu, Mario Zannoni, and Ningfeng Zhu. Small Aperture Telescopes for the Simons Observatory. *Journal of Low Temperature Physics*, April 2020

Maximilian H. Abitbol et al.). The Simons Observatory: Astro2020 Decadal Project Whitepaper. *Bull. Am. Astron. Soc.*, 51:147, 2019

ABSTRACT OF THE DISSERTATION

Exploring the Early Universe and Dark Matter with the Cosmic Microwave Background

by

Jacob Warrick Spisak

Doctor of Philosophy in Physics

University of California San Diego, 2024

Professor George Fuller, Chair
Professor Brian Keating, Co-Chair

This dissertation contains works spanning several topics in cosmology and astrophysics. They are tied together by themes of dark matter and the Cosmic Microwave Background, but with a highly varied methodology spanning theory, data analysis, and hardware. Chapter 2 introduces a novel production mechanism for sterile neutrino dark matter involving multiple interacting sterile neutrinos. Chapter 3 presents a search for axion-like particle dark matter using the CMB telescope POLARBEAR. Finally, Chapter 4 describes the building and testing of the Small Aperture Telescope for the next-generation CMB experiment the Simons Observatory.

Chapter 1

Introduction

In the past century or so cosmology has made impressive advances, developing a unified model of dark energy, cold dark matter, and baryons (ΛCDM) that can explain the evolution of the universe from one second after the big bang until the present day. It was 60 years ago that Penzias and Wilson first provided landmark evidence [155] for the big bang with the discovery of the Cosmic Microwave Background (CMB) - now dozens of experiments have measured its tiny temperature and polarization anisotropies to extreme precision, unveiling the nature of the primordial plasma that existed well before the formation of the first stars. A multitude of measurements, including the CMB, big bang nucleosynthesis (BBN), galaxy surveys, cosmic distance measurements, gravitational lensing, and others, have provided percent-level precision on ΛCDM model parameters. These varied tracers all (mostly) agree, and much further improvement currently takes the form of large-scale collaborations making increasingly precise measurements that probe the limits of this model.

Nevertheless, it can be argued that much of ΛCDM involves parameterizing our ignorance. A quarter of the energy budget of the universe is tied up in dark matter, whose identity has eluded physicists and astronomers for decades. Even less is known about dark energy, which dominates the universe today, constituting 70% of its total energy density. Evidence points to a period of inflation before the big bang, but a wide variety of inflationary models cannot be discriminated between using current data. It is unknown how the early universe produced an excess of matter

over antimatter. Many of these problems have overlap with particle physics, which has supplied a plethora of candidates to jointly explain issues in both fields.

This thesis will attempt to provide insight into a few of these topics, chief among them dark matter and the CMB. In doing so, it will involve a wide variety of theoretical and experimental methods, including pen and paper theory, statistical analyses, cryogenic telescopes, and building contracts with Chilean construction companies. Chapter 2 will present a mechanism for producing sterile neutrino dark matter in the early universe that evades traditional x-ray and mass bounds. Chapter 3 involves a search for axion-like particle dark matter using the time-dependent polarization rotation signature it imprints on the CMB. Finally, chapter Chapter 4, will describe efforts to build the next generation of CMB telescopes searching for evidence of inflation.

1.1 The Cosmic Microwave Background and a Brief History of the Early Universe

To understand the CMB it is helpful to briefly review the history of the early universe. Our narrative starts from just before the earliest event for which we have evidence, big bang nucleosynthesis. At this point, the universe is energetically dominated by a hot, dense plasma, composed of photons, electrons, positrons, neutrinos of all three flavors, protons, and neutrons, all in thermal equilibrium. The plasma is nearly homogeneous and isotropic, with only very small perturbations that are nevertheless very important, as they will become the seeds of galactic structure. The universe is rapidly expanding and cooling, and when the temperature drops below about 1 MeV (10^{10} K), when the universe is about 1 second old, nuclei begin to form, in a process that ultimately yields 75% Hydrogen, 25% Helium, and a smattering of other elements. It is the alignment of abundances of these elements today with the big bang nucleosynthesis predictions that provides the earliest evidence of this thermal state of the universe.

Around this same time the electrons and positrons annihilate, leaving only a small number

of electrons to maintain charge neutrality, and the neutrinos decouple from the rest of the plasma as the interactions that keep them in thermal equilibrium become inefficient. The plasma persists in this basic state for several hundred thousand years, as the perturbations grow in the form of sound waves in the baryon-photon plasma, which oscillate under the gravitational influence of the neutrinos and dark matter. The latter becomes increasingly important as time progresses, and begins to dominate the energy density of the universe about 50,000 years after the big bang.

The CMB is released when the universe is several hundred thousand years old. At this point, the temperature has dropped to a few tenths of an eV (a few thousand Kelvin), and the photons no longer have enough energy to keep the Hydrogen ionized, so the electrons and protons combine to form neutral Hydrogen. This event decouples the photons, as their scattering rate on neutral Hydrogen is quite small, and we observe this radiation today in the microwave at a temperature of 240 μeV, or 2.73 K [76]. It is still a nearly perfect blackbody, having travelled until the present day affected only by minor distortions and redshift. In the meantime, the perturbations grew large enough to collapse and form the stars, galaxies, dark matter halos, gas, etc. that populate the universe today.

Current experiments studying the CMB are mostly focused on its anisotropies, which contain a wealth of information about the primordial perturbations, the parameters of ΛCDM, and the post-recombination universe. Important for this thesis in particular is the faint polarization of the CMB, which is generated by during its release by Thompson scattering . It is convenient to chose as a basis for the polarization states parity-even E-modes and parity-odd B-modes, because the former are exclusively generated by Thompson scattering. The latter are known to be produced at a much lower level after recombination by gravitational lensing of E-modes, but also by a number of other, more exotic phenomena. For instance, any linear polarization rotation will turn E-modes into B-modes, which will be exploited in Chapter 3 to search for axion-like dark matter.

What happened before big bang nucleosynthesis? The cosmological history can be extrapolated backwards in time, to smaller sizes and higher temperatures, until eventually a

singularity is reached. There are, however, a number of problems with accepting this extrapolation at face value [194]. The horizon problem relates to how the universe came to be in thermal equilibrium: the CMB is isotropic to approximately one part in 10^5, and yet patches of the CMB that today correspond to an angular separation of more than a few degrees did not have time to come into casual contact (and thus equilibrate) by the time of recombination. The second problem is the flatness problem: the geometric curvature of the universe today is measured to good precision be zero [23], and because curvature increases with time, in the early universe it must have been extremely close to zero. Both problems thus present issues of initial conditions: why was the initial curvature of the universe nearly zero, and why were initial conditions everywhere nearly the same?

Both problems have a solution in the idea of inflation, a hypothesized period of exponential expansion of the early universe [94]. This expansion could drive any initial curvature value down to near zero, and casually connect all observed regions of the sky. Moreover, quantum fluctuations during inflation provide a explanation for the source of the primordial perturbations in the primordial plasma. However, while today inflation is the dominant explanation for what happened in the very early universe, there are a wide variety of models that realize inflation, and relatively little evidence to distinguish between them. A key target of modern experiments is the CMB B-mode signature predicted to be generated by inflationary gravitational waves. The search for inflationary B-modes is the primary motivation for the construction of the Small Aperture Telescopes of the Simons Observatory, whose construction is the topic of Chapter 4.

1.2 Axion-Like Particles and Cosmic Birefringence

Pseudoscalar fields, which show up in a variety of beyond-standard-model theories, have an astrophysically-relevant coupling to the electromagnetic field

$$\mathcal{L} = -\frac{1}{4} g_{\phi\gamma} \phi F_{\mu\nu} \tilde{F}^{\mu\nu}. \tag{1.1}$$

Here ϕ is the pseudoscalar, $g_{\phi\gamma}$ is the coupling constant, $F_{\mu\nu}$ is the electromagnetic field tensor and $\tilde{F}^{\mu\nu}$ is its dual. The effect of this coupling is to modify electromagnetic waves such that opposite-helicity photons (i.e. left and right circular polarization states) pick up opposite-sign phases. For a linearly polarized wave, this generates a rotation in polarization angle [96, 50],

$$\Delta\beta = \frac{1}{2}g_{\phi\gamma}(\phi(x_{\text{abs}}) - \phi(x_{\text{emis}}))$$

(1.2)

This effect has been dubbed "cosmic birefringence" due to its similarity to the effect a birefringent material has on the propagation of electromagnetic waves. A key feature of cosmic birefringence is that the net effect depends only on the field values at absorption and emission, and is independent of the intermediate field values.

Cosmic birefringence may be searched for using a variety of polarized astrophysical sources, and a source of a particular interest for this thesis is the CMB. Relative to other sources, the CMB has a big disadvantage in that its polarization is very faint, but also has a number of advantages that make it an attractive target. The CMB polarization signal is extremely well known theoretically, and also has been well measured by several telescopes. This allows for consistency checks, especially for a claimed detection. Furthermore, the CMB scan strategies are often already optimized for cosmic birefringence searches, and their polarization systematics are well understood. A number of different CMB experiments have conducted searches for isotropic, anisotropic, and time-dependent cosmic birefringence [11, 12, 17, 14, 13, 75, 142, 137].

Chapter 3 will be concerned with the search for cosmic birefringence generated by extremely low mass ($m_\phi \sim 10^{-22} - 10^{-20}$eV) pseudoscalars called axion-like particles, or axions for short (unlike the canonical QCD axion, we do not associate our axion with a solution to the strong CP problem [154, 153, 193, 195]). The cosmological evolution of the homogeneous component of ϕ is given by [130]

$$\ddot{\phi} + 3H\dot{\phi} + m_\phi^2\phi = 0,$$

(1.3)

assuming that the dominant term in the potential is the the mass term, $V(\phi) \approx \frac{1}{2}m_\phi^2\phi^2$. When $H >> m_\phi$, Hubble friction keeps ϕ fixed at a constant value and the axion acts as dark energy. When $H << m_\phi$ the field oscillates, the energy density decreases as $\rho \propto a^{-3}$ (where a is the scale factor), and the axion therefore acts as dark matter. At matter-radiation equality, the Hubble rate is $H \approx 10^{-28}$eV, and so axions than masses larger than this begin oscillation in radiation domination, and axions with masses smaller than this begin oscillation during matter domination. Depending on the mass, therefore, the axion may compose a significant fraction of dark energy or dark matter. In the crossover mass range the axion can have significant impacts on the power spectrum of primordial perturbations (completely independent of cosmic birefringence), and searches [105, 106] have used this impact to place exclusions across a mass range $10^{-33} \leq m_\phi \leq 10^{-24}$ eV.

In the mass range that will be considered in Chapter 3, the axion acts like dark matter for all relevant periods of cosmological history. The resulting dark matter is called "fuzzy dark matter" because it is so light that it has an astrophysically large de Broglie wavelength [113],

$$\lambda_{DB} \equiv \frac{2\pi}{m_\phi v} = 0.48\text{kpc} \left(\frac{10^{-22}\text{eV}}{m_\phi}\right)\left(\frac{250\text{km/s}}{v}\right), \tag{1.4}$$

where v is the velocity dispersion of the halo. Fuzzy dark matter suppresses and modifies small-scale structure formation, and this provides a potential exotic solution to longstanding problems at small scales within the cold dark matter paradigm [114]. Chapter 3 will describe a search for a cosmic birefringence signature generated by axions in the fuzzy dark matter regime.

1.3 Sterile Neutrinos

Sterile neutrinos are hypothetical right-handed fermions that are neutral under the electromagnetic, weak, and strong forces. They are the counterpart of standard model (SM) neutrinos (hereafter also called 'active' neutrinos), which are left-handed and charged under the weak interaction. A primary reason to consider the existence of sterile neutrinos lies in the unresolved

problem of neutrino masses. Neutrinos are massless in the SM, yet it has now been definitely established by decades of experiments that neutrinos do have mass. These experiments rely on the phenomena of neutrino oscillations: a neutrino produced as one flavor may be measured as a different flavor later on, demonstrating that the neutrino flavor states and the mass states (i.e. propagation eigenstates) are not the same. The oscillation length depends on the square of the difference between the neutrino masses, and in this way two mass squared differences have been measured, $\Delta m_{21}^2 = 7.39^{+0.21}_{-0.20} \times 10^{-5} \text{eV}^2$ and $\Delta m_{32}^2 = 2.449^{+0.032}_{-0.030} \times 10^{-3} \text{eV}^2$ [196]. This establishes the existence of at least two non-zero mass states. Furthermore, cosmological observations suggest that the sum of all neutrino masses is less than 120 meV [23], which would mean that neutrinos are more than six orders of magnitude lighter than the next lightest fermion. These puzzles, among others, make the neutrino sector a prime candidate for new physics.

The addition of sterile neutrinos allows two new gauge-invariant and renormalizable mass terms,

$$\mathscr{L}_{\text{mass}} = -F_{\alpha i}\overline{L}_\alpha N_i \Phi - \frac{M_i}{2}\overline{N}_i^C N_i + \text{h.c.}. \tag{1.5}$$

Here L_α is the standard-model lepton doublet, with corresponding Yukawa couplings $F_{\alpha i}$ and the SM Higgs doublet Φ. Any number of sterile neutrino states N_i may be added. The first term yields a mass term (the Dirac mass) after electroweak symmetry breaking in the same way as the other SM fermions. The second term is called the Majorana mass term and is unique to neutrinos. In the Seesaw mechanism the neutrino masses are suppressed via the ratio of the small Dirac mass and the large Majorana masses, and can therefore example the observed smallness of the neutrino masses [64, 47].

In addition to its motivation from puzzles in the neutrino sector, a sterile neutrino with a small active-sterile mixing makes an excellent dark matter candidate. It has small enough interactions with the SM to act as dark matter, and for the right masses it has a plausible production mechanism in the early universe. In the simplest case it also has relatively few parameters - one mixing angle controls its production, lifetime, and generates an astrophysical

observable in the form of an electromagnetic line. There are many ways to produce sterile neutrino dark matter, but the most basic is a process known as scattering-induced decoherence. Consider the case in which there is only one active neutrino of flavor α (e, μ, or τ), and one sterile neutrino N. The unitary transformation between the mass states and flavor states is given by a rotation matrix

$$|\nu_\alpha\rangle = \cos(\theta)|\nu_1\rangle + \sin(\theta)|\nu_2\rangle \tag{1.6}$$

$$|N\rangle = -\sin(\theta)|\nu_1\rangle + \cos(\theta)|\nu_2\rangle. \tag{1.7}$$

In the regime of interest the mixing angle θ is small, so that one mass state $|\nu_1\rangle$ is mostly active, and the other $|\nu_2\rangle$ is mostly sterile. Because of this, in a slight abuse of notation we will refer to the mass associated with $|\nu_2\rangle$ as m_N and call it the mass of the sterile neutrino.

To understand scattering-induced decoherence, recall that in the early universe plasma above a temperature of about 1 MeV, the active neutrinos were thermally coupled to the SM plasma. Heuristically, each scattering event can be thought of as a measurement of the neutrino flavor. As the active neutrinos oscillate they pick up a small sterile component, so at each scattering event there is some small probability to generate a sterile neutrino. In this way, a population of sterile neutrinos may be steadily built up in the early universe. See Figure 1.1. This process is described through a Boltzmann equation [2] (see also Section 2.7),

$$\left(\frac{\partial}{\partial t} - Hp\frac{\partial}{\partial p}\right) f_N = \frac{1}{2}\Gamma_\alpha P(\nu_\alpha \to N)(f_{\nu_\alpha} - f_N), \tag{1.8}$$

where the probability to transform an active neutrino into a sterile neutrino is

$$P(\nu_\alpha \to N) = \frac{1}{2}\frac{\Delta^2 \sin^2(2\theta)}{\Delta^2 \sin^2(2\theta) + \left(\frac{\Gamma_\alpha}{2}\right)^2 + (\Delta\cos(2\theta) - V_\alpha)^2}. \tag{1.9}$$

Here H is the Hubble rate, f_N and f_{ν_α} are the sterile and active neutrino distribution

functions, Γ_α is the scattering rate of active neutrinos of flavor α on the primordial plasma, and $\Delta \approx \frac{m_N^2}{2p} \cdot \left(\frac{\Gamma_\alpha}{2}\right)^2$ is the quantum damping factor, which ensures that production is suppressed if the neutrinos do not have time between scattering events to build up a sterile component via oscillation. V_α is the in-medium potential that the active neutrinos acquire in the plasma.

It can be seen that (1.8) is simply proportional to the active neutrino scattering rate multiplied by the conversion probability. Production is suppressed at very high plasma temperatures by quantum damping and the in-medium potential, both of which drive the conversion probability to zero, and at low temperatures by the declining efficiency of active neutrino scattering.

The fact that this process can build up the correct amount of dark matter for certain masses and mixing angles was pointed out by Dodelson and Widrow [68]. This Dodelson-Widrow mechanism gives the right relic abundance for $\sim$ keV masses with the approximate relation [2]

$$\Omega h^2 \approx 0.3 \left(\frac{\sin^2(2\theta)}{10^{-10}}\right) \left(\frac{m_N}{100\text{keV}}\right)^2. \tag{1.10}$$

The Dodelson-Widrow mechanism is bounded by several constraints: see Figure 1.2. The upper edge of the mass range is set by the requirement that the sterile neutrino's lifetime is much larger than the age of the universe. The relevant decay channel is the rate into three active neutrinos, which is [33]

$$\Gamma_{3\nu} = \frac{1}{192\pi^3} G_F^2 m_N^5 \sin^2(\theta). \tag{1.11}$$

This rate goes like five powers of mass, while the RHS of (1.10) goes like two powers of mass, which prevents any sterile neutrino with a mass greater than about 1 MeV from being a Dodelson-Widrow candidate. The lower edge of the mass range is set by the requirement that dark matter not be too hot, which suppresses the formation of small scale structure. This constraint depends on the energy spectrum of the sterile neutrino, which in turn depends on the formation mechanism. The Dodelson-Widrow mechanism generates a particularly hot energy spectrum, as can be seen in Figure 1.2.

Another decay channel provides a means of detection: radiative decay. This channel,
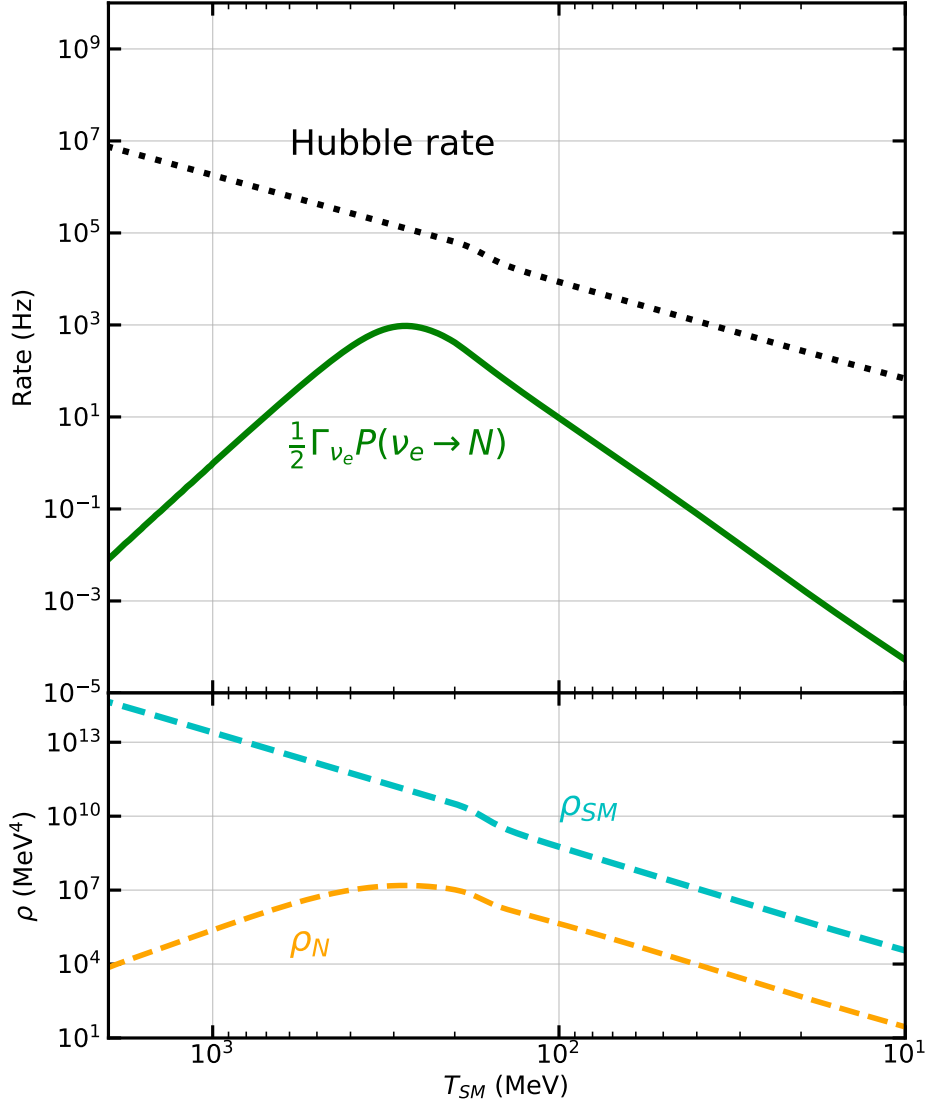
Figure 1.1. An example of the Dodelson-Widrow mechanism. The sterile neutrino is produced in the early universe through scattering-induced decoherence in the correct abundance to make all of the dark matter. The x-axis shows the temperature of the SM plasma, and the top panel shows the production rate in green, which is always less than the Hubble rate to avoid thermal equilibrium. The bottom panel shows the energy density of the sterile neutrino and the SM plasma. The sterile neutrino parameters are $m_N = 10$ keV and $\sin^2(2\theta) = 3 \times 10^{-9}$, and the production rate is evaluated at p=3T.

which yields an active neutrino and a photon, is loop-suppressed and therefore subdominant to $\Gamma_{3\nu}$. The rate is [150]

$$\Gamma_{\nu\gamma} = 6.8 \times 10^{-33}\text{s}^{-1} \left(\frac{m_N^5}{1\text{keV}} \right) \left(\frac{\sin^2(2\theta)}{10^{-10}} \right) \tag{1.12}$$

The resulting photon is at an energy equal to one-half the rest mass, which for keV sterile neutrinos puts it in the x-ray. This has lead to a large number of over the last two decades for a decay line. Currently, x-ray searches have essentially ruled out the viable Dodelson-Widrow parameter space, as can be seen in Figure 1.2 (Also seen is that recent structure bounds, which have improved significantly over that time period, now actually disfavor much of the range as well).

A popular modification to the Dodelson-Widrow scenario is the Shi-Fuller mechanism [173], wherein scattering-induced decoherence production is enhanced by the presence of a non-zero lepton flavor asymmetry. Unlike the baryon asymmetry, which is well measured and extremely small at $\eta = 6 \times 10^{-10}$ [23], it is possible that much larger primordial lepton flavor asymmetries existed. The presence of such an asymmetry adds an additional, opposite-sign term to the in-medium potential, which can resonantly enhance the production rate at mass level crossings. This allows for the dark matter abundance to be produced at a smaller mixing angle for a given sterile neutrino mass. Additionally, it produces a colder energy spectrum, which relaxes the low mass end of the constraints. With recent x-ray observations, however, most of the space for the Shi-Fuller mechanism has also been ruled out.

A plethora of other mechanisms for producing sterile neutrino dark matter exist, all of which require additional degrees of freedom. In Chapter 2, I will discuss a novel mechanism that uses two or more sterile neutrinos and a variation of the Dodelson-Widrow mechanism to achieve the correct dark matter density while evading the x-ray and mass bounds.
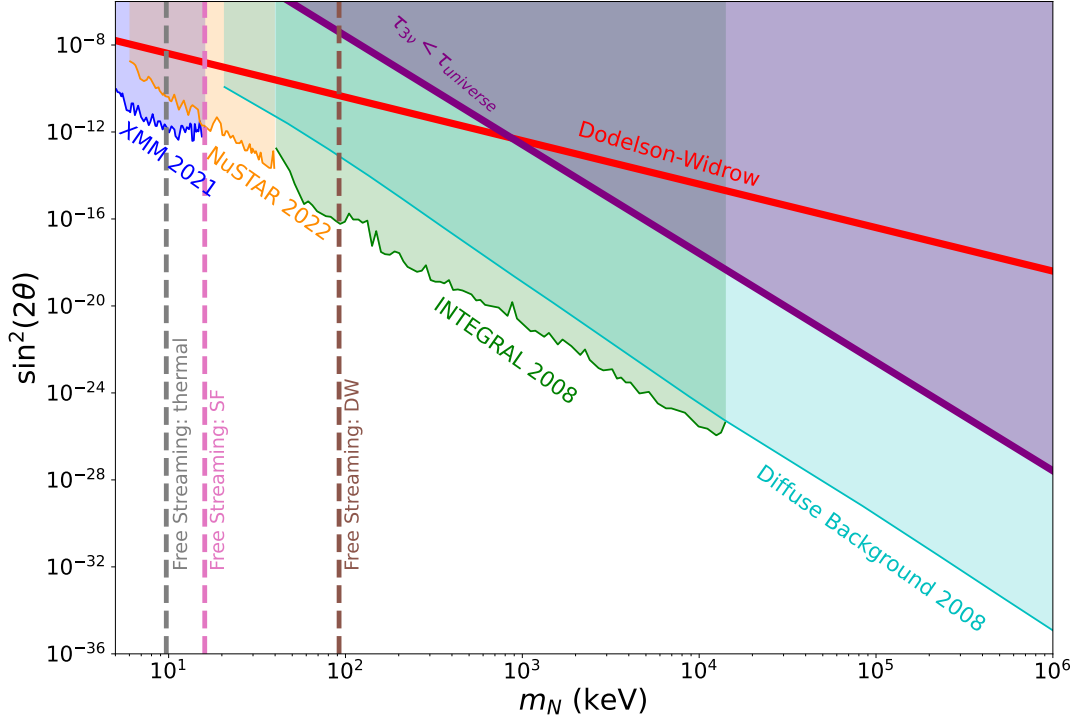
Figure 1.2. Bounds on sterile neutrino mass and mixing angle. X-ray and γ-ray constraints are from the SPI spectrometer (on board the INTEGRAL space telescope) measurements of the Milky Way dark matter halo [42], SPI, COMPTEL, and EGRET measurements of the isotropic diffuse photon background [202], XMM-Newton measurements of the Milky Way dark matter halo [77], and NuSTAR observations [165]. The parameter space is bounded at low masses from small-scale structure constraints from strong gravitational lensing and Milky Way Satellite Galaxies [141] applied to energy spectra from the Dodelson-Widrow and Shi-Fuller mechanisms, as well as a generic fermion dark matter candidate with two degrees of freedom and a thermal spectrum. The purple region indicates where the lifetime for decay into three active neutrinos is less than the age of the universe. The red line indicates the slice of parameter space for the Dodelson-Widrow mechanism (for mixing with the electron neutrino).

Chapter 2

Dark population transfer mechanism for sterile neutrino dark matter

2.1 Abstract

We present a mechanism for producing a cosmologically-significant relic density of one or more sterile neutrinos. This scheme invokes two steps: First, a population of "heavy" sterile neutrinos is created by scattering-induced decoherence of active neutrinos; Second, this population is transferred, via sterile neutrino self-interaction-mediated scatterings and decays, to one or more lighter mass ($\sim 10\,\mathrm{keV}$ to $\sim 1\,\mathrm{GeV}$) sterile neutrinos that are far more weakly (or not at all) mixed with active species and could constitute dark matter. Dark matter produced this way can evade current electromagnetic and structure-based bounds, but may nevertheless be probed by future observations.

2.2 Introduction

An outstanding issue at the heart of physics and astronomy is the identity of the dark matter (DM). Among the many beyond-Standard-Model (BSM) candidates for DM, the neutrino sector offers an alluring possibility: a Standard Model (SM) singlet "sterile" neutrino. However, the simplest mechanisms for producing a dark matter-relevant relic density of these particles are challenged by X-ray and large scale structure observations (e.g., [2, 4, 69, 126, 1, 18, 41, 62,

13

8, 203, 69] and references therein). In this chapter we propose a mechanism for producing a relic density of sterile neutrinos that may be able to evade current bounds, yet may be probed by future observations.

The standard Dodelson-Widrow mechanism [68] for sterile neutrino dark matter production requires only a vacuum mixing between the sterile and active (SM) neutrinos. At ultra-high temperatures in the early Universe, this mixing is medium-suppressed, but subsequently, at lower temperatures, $T \sim \text{GeV}$, a cosmologically significant abundance of sterile neutrinos can be built-up via active neutrino scattering-induced decoherence. However, the same mixing that enables this freeze-in production scenario also provides a sterile neutrino radiative decay channel into a photon and an active neutrino [150]. Demanding a relic density of a long-lived DM candidate in this scheme picks out a $m_{\text{s}} \sim \text{keV}$ mass-scale associated with the sterile state. That implies a decay-generated X-ray line at an energy $E_\gamma = m_{\text{s}}/2$ that is nicely matched to the energy sensitivity range of the X-ray observatories, enabling them to provide stringent constraints [4].

Other production mechanisms for sterile neutrino DM abound, but all require additional new physics on top of the minimalist mass and vacuum mixing parameters of Dodelson-Widrow. Some propose the sterile neutrino DM abundance to stem from decays of heavier particles [172, 157, 135, 175] or primordial black holes [55], while being relatively agnostic about the active-sterile coupling. Similarly, the correct sterile neutrino population can be achieved via thermalization [95], dilution of their initially produced overabundance [151], or, e.g., via SIMP-like freeze-out [100]. Other production scenarios focus on altering the active-sterile mixing. One example is the Shi-Fuller mechanism [173, 2, 123, 122, 91, 190, 110] wherein the in-medium active-sterile mixing is resonantly enhanced by a cosmic lepton number asymmetry, which may be generated through the asymmetric decay of heavier sterile states (à la νMSM: e.g., [27, 29, 30, 172, 171] and many more). Another invokes vacuum parameters mediated by scalar [36, 37, 38] or axion-like [35] fields.

Intriguing dynamics can be achieved by bringing self-interactions into the picture. Strongly self-interacting active neutrinos can boost sterile neutrino production and, hence,

result in the required DM relic abundance at smaller mixing angles [65, 57]. On the other hand, self-interactions among the sterile neutrinos themselves can lead to resonantly enhanced production, which has been investigated in the case of a heavy mediator [118] and more recently also in the light mediator limit [45, 31].

These considerations lead us to a scheme that utilizes the advantages of both active neutrino scattering-induced decoherence and sterile neutrino self interactions. Though there could be many sterile states, in a dark sector for example [3], we can illustrate the key features of our mechanism by considering sterile neutrino DM production in the presence of two sterile species with a dark self-interaction channel. This simple scenario may be further motivated by the experimental observations requiring at least two non-zero active neutrino masses.

2.3 Dark Sector Dynamics

The basic idea of this mechanism is the following: (1) The heavier of the two sterile neutrinos has a small mixing with active neutrinos, enabling scattering-induced decoherence to populate this heavier sterile state; (2) Before the heavy sterile neutrino population can decay back into the SM by virtue of its mixing, self-interactions within the sterile sector engender a population transfer to the lighter sterile neutrino state. (3) The population of the lighter sterile state (or states) created this way persists until the present and can be the dark matter or a component of it, provided its mixing with the active neutrinos is sufficiently small.

The background evolution of the SM plasma and the dark sector are governed by the following set of equations:

$$\frac{d\rho_{\mathrm{SM}}}{dt} = -3H(\rho_{\mathrm{SM}} + P_{\mathrm{SM}}) - \frac{d\rho_{\mathrm{inj}}}{dt}, \tag{2.1}$$

$$\frac{d\rho_{\mathrm{DS}}}{dt} = -3H(\rho_{\mathrm{DS}} + P_{\mathrm{DS}}) + \frac{d\rho_{\mathrm{inj}}}{dt}, \tag{2.2}$$

$$H^2 = \frac{8\pi G}{3}(\rho_{\mathrm{SM}} + \rho_{\mathrm{DS}}), \tag{2.3}$$

where $\rho_{\text{SM/DS}}$ and $P_{\text{SM/DS}}$ are the energy density and pressure in the SM plasma and dark sector, respectively, and H is the Hubble parameter. The first two equations describe energy conservation within each sector, with the exception of a small amount of energy transfer $d\rho_{\text{inj}}/dt$ from the SM plasma into the dark sector. The last equation is simply the Friedmann equation in a flat universe.

The energy injected into the dark sector via scattering-induced decoherence is [2]

$$\frac{d\rho_{\text{inj}}}{dt} = \int \frac{d^3p}{(2\pi)^3} E f_{\nu_\alpha}^{(\text{eq})} \frac{\Gamma_\alpha}{2} P(\nu_\alpha \to N_1), \tag{2.4}$$

where $P(\nu_\alpha \to N_1)$ is the probability that an active neutrino of flavor $\alpha = e, \mu$, or τ, energy E and momentum p has converted into N_1, the heavier sterile neutrino. It depends on the mixing between N_1 and ν_α; here we will assume that the mixing occurs only with one flavor, characterized by a single vacuum mixing angle θ. While in our calculations we treat the active-sterile mixing as a free parameter, it nevertheless arise in specific models, e.g., Seesaw mass models [64, 47].

The scattering rate of an active neutrino on the SM plasma with a temperature T_{SM} is

$$\Gamma_\alpha(p, T_{\text{SM}}) = C_\alpha(p, T_{\text{SM}}) G_F^2 p T_{\text{SM}}^4, \tag{2.5}$$

where $C_\alpha(p, T_{\text{SM}})$ is a temperature-dependent coefficient and G_F is the Fermi coupling constant. Assuming that the SM neutrinos follow a thermal Fermi-Dirac energy distribution with zero chemical potential for $T_{\text{SM}} \gg 1\,\text{MeV}$, one has $f_{\nu_\alpha}^{(\text{eq})}(E, T_{\text{SM}}) = (e^{E/T_{\text{SM}}} + 1)^{-1}$. We ignore Pauli-blocking effects and the conversion of sterile neutrinos back into active neutrinos, thereby decoupling the energy injection rate from the dynamics within the dark sector. See the appendix for additional details.

In general, the evolution of the sterile neutrinos is described by a set of coupled Boltzmann equations. However, if we restrict ourselves to the regime where the dark sector quickly reaches thermal equilibrium with itself as a result of self-interactions, then the dark sector's energy

density and pressure are completely determined by its temperature, T_{DS}, and the masses of the dark sector constituents. This eliminates the need to evolve the individual Boltzmann equations, and (2.1)-(2.4) form a set of coupled equations for T_{DS}, T_{SM}, and the scale factor as functions of time. To good approximation, the latter two quantities can be solved for independently of T_{DS}, since the energy injected into the dark sector is relatively small. To solve for T_{DS}, we numerically evolve (2.2) from a starting plasma temperature T_{SM} at which scattering-induced decoherence is highly suppressed, with zero initial abundance for both sterile states.

To demonstrate how the mechanism could work, we choose the dark sector to consist of two sterile neutrinos N_1 (heavy) and N_2 (light) with a scalar mediator ϕ:

$$\mathcal{L} \supset \frac{g_\phi^{ij}}{2} \overline{N}_j^C N_i \phi + \text{h.c.}, \tag{2.6}$$

where $i, j = 1, 2$. For simplicity, we take all $g_\phi^{ij} = g_\phi$ to be equal, and take the heavy-mediator limit wherein $G_\phi \equiv g_\phi^2 / m_\phi^2$ is the effective interaction strength. Note that taking this limit makes the whole discussion quite general, as it allows us to be agnostic about the specific UV origin of the self-interaction.

Thermal equilibrium and population transfer within the dark sector may be achieved through various combinations of self-interaction processes, namely, 2-to-2 scatterings, 1-to-3 decays, and potentially 2-to-4 scatterings. These rates scale as follows (see the appendix for a more detailed discussion):

$$\Gamma_{\phi, 2\to 2} \propto \beta G_\phi^2 p T^4 \tag{2.7}$$

$$\Gamma_{\phi, 1\to 3} \propto G_\phi^2 m_N^5 / \gamma(p) \tag{2.8}$$

$$\Gamma_{\phi, 2\to 4} \propto G_\phi^2 T^4 \Gamma_{\phi, 2\to 2}. \tag{2.9}$$

Here, T and β are the temperature and a suppression factor, respectively, parameterizing a Fermi-Dirac-like distribution for the sterile neutrino(s): $f(E, T) \simeq \beta / (e^{E/T} + 1)$. $\Gamma_{\phi, X \to Y}$
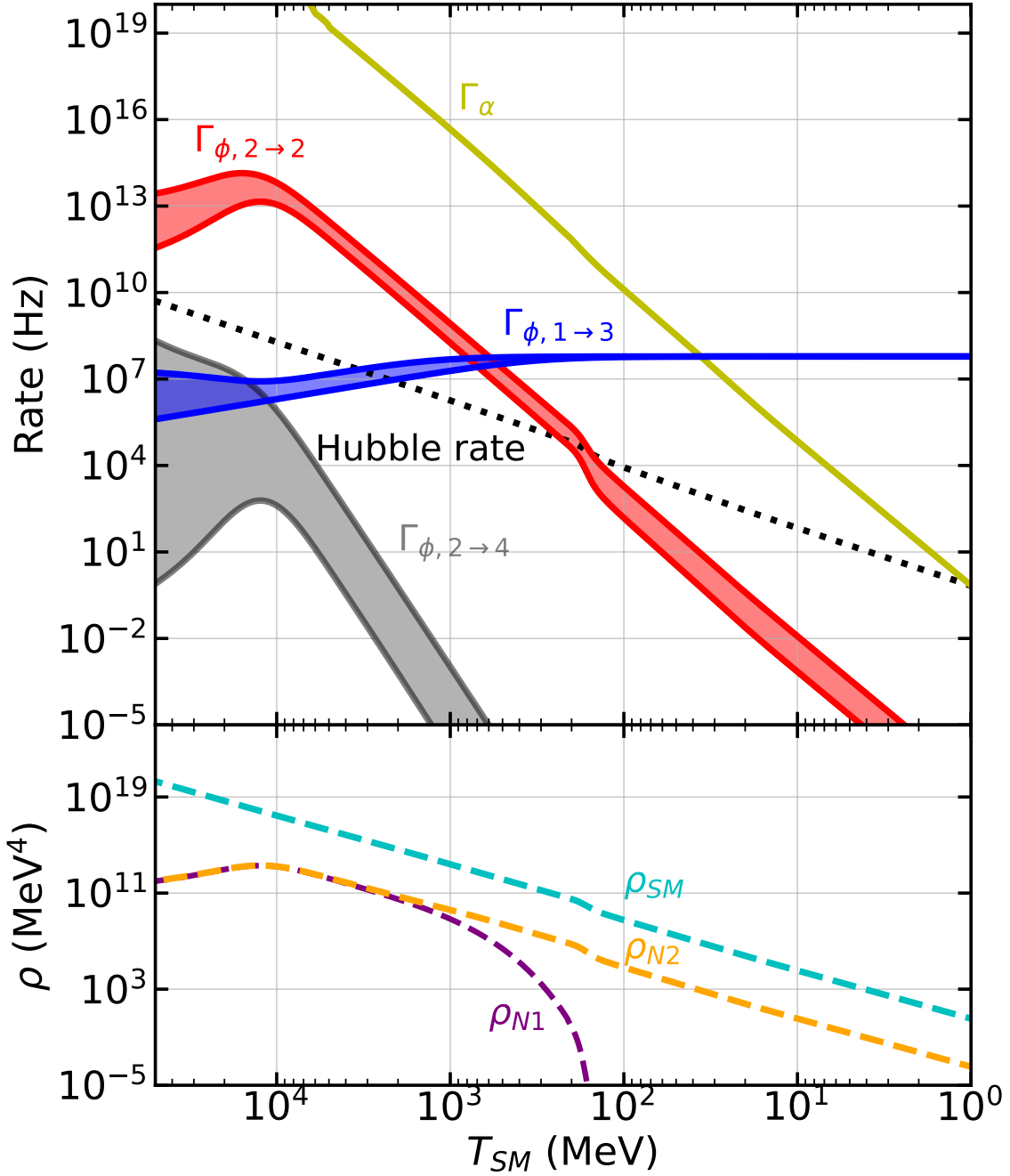
Figure 2.1. *Bottom panel*: Evolution of SM and sterile neutrino energy densities as a function of SM plasma temperature $T_{\rm SM}$. In this scenario, thermalization within the dark sector, and population transfer from the heavier (N_1) to the lighter (N_2) sterile neutrino, are achieved through contemporaneous 2-to-2 scatterings and 1-to-3 decays. *Top panel*: Rates of various processes [(2.3), (2.5), and (2.7)–(2.9)], as indicated. The width of the colored bands represents the variation of the rates as the dark sector thermalizes (see text for details). Here, $m_{N_1} = 1\,{\rm GeV}$, $\sin^2(2\theta) = 10^{-15}$, $G_\phi = 0.1\,G_F$, $\alpha = {\rm electron}$, and all rates are evaluated at $p = 3T$.

18

refers to a ϕ-mediated process with X sterile neutrinos in the initial state and Y sterile neutrinos in the final state. $\gamma(p)$ in (2.8) is the Lorentz factor for a heavy sterile neutrino with momentum p, accounting for a time-dilation of its lifetime.

These may be evaluated in two regimes of interest: *without* and *with* dark sector internal thermalization. Without thermalization, a suppressed Fermi-Dirac form with $T = T_{SM}$ and $\beta \ll 1$ is a reasonable approximation to the N_1 distribution generated by active neutrino scattering-induced decoherence. Subsequently, if the dark sector internally thermalizes, the distribution functions instead assume *un-supressed* Fermi-Dirac forms (i.e., with $\beta = 1$) parameterized by a *dark sector temperature* T_{DS}. Assuming an empty dark sector to begin with, and subsequent energy conservation within the dark sector as it thermalizes, one must have

$$g^{\star}_{DS} T^4_{DS} = g^{\star}_{N_1} \beta T^4_{SM}, \tag{2.10}$$

and therefore $T_{DS} < T_{SM}$. Here, $g^{\star}_{N_1}$ and $g^{\star}_{DS}$ are respectively the number of degrees of freedom of the heavy sterile N_1, and in the dark sector overall. For a typical momentum $p \simeq 3T$, $\Gamma_{\phi,2\to2}$ and $\Gamma_{\phi,2\to4}$ are proportional to T^5 and T^9, respectively. Therefore, the decrease in temperature from T_{SM} to T_{DS} outweighs the increase of β from $\ll 1$ to $\beta = 1$, leading to an overall reduction in the rates post-thermalization. The decay rate for the heavy sterile neutrino in the plasma rest frame is always larger after dark sector thermalization because $T_{DS} < T_{SM}$.

To assess the prospects of dark sector internal thermalization, these rates may be compared to the Hubble rate, $H = \sqrt{8\pi g^{\star}_{SM}/3}(T^2/m_{pl})$, where $g^{\star}_{SM}$ is number of relativistic degrees of freedom in the SM plasma. On the other hand, to avoid resonant overproduction due to the additional in-medium potential provided by the self-interaction, we require that $\Gamma_{\phi,2\to2} < \Gamma_\alpha$ [118]. We also require that $g_\phi < 1$ to stay in the perturbative regime. These requirements may be simultaneously satisfied over some range of G_ϕ values, given a sterile neutrino mass m_{N_1} and vacuum mixing angle θ.

This mechanism is illustrated for a particular choice of parameters in Fig. 2.1. For both

$\Gamma_{\phi,2\to2}$ and $\Gamma_{\phi,2\to4}$, the upper and lower edges of each band reflect the rate expressions without and with dark sector internal thermalization, respectively. For $\Gamma_{\phi,1\to3}$ the situation is reversed. N_1 is produced via scattering-induced decoherence, and initially the dark sector has not achieved internal thermal equilibrium due to a lack of number-changing processes. This changes once $\Gamma_{\phi,1\to3} > H$: this process increases the number of sterile neutrinos, and the 2-to-2 processes, which are initially much faster than the decays, ensure the N_1 and N_2 populations equilibrate with roughly equal number densities. Note that SM decay branches for N_1 are subdominant for these parameter choices compared to the dark decays (see the appendix). As the dark sector thermalizes, the rates switch to the opposite sides of the bands[1]. Eventually, N_1 becomes non-relativistic and is Boltzmann-suppressed, transferring N_1 into N_2. 1-to-3 decays, which eventually become faster than 2-to-2 processes, further aid this transfer. N_2 then persists until the present day as a component of dark matter.

An alternative scenario can achieve this dark sector internal thermalization through 2-to-4 processes. Although these are relevant only at high temperatures and for a much smaller slice of the parameter space than the previous example, they would allow for smaller N_1 masses. This is because $\Gamma_{\phi,1\to3} \propto N_1^5$, and so smaller masses have a lower 1-to-3 rate that may not be significant at high enough T_{SM} to overlap with 2-to-2 processes.

2.4   Parameter Space

Under the assumption that the dark sector thermalizes internally, the parameter space in which all of the dark matter is produced is shown in Fig. 2.2. The left panel shows contours of the final dark sector temperature relative to the SM temperature. In the viable parameter space this ratio is less than one for two reasons: the active-sterile mixing is too small to thermalize the dark sector with the SM, and the SM plasma is heated by the disappearance of relativistic degrees of freedom as the temperature drops. The right panel of Fig. 2.2 shows contours of the

---

[1]Unless a freeze-out ($\Gamma_\phi < H$) occurs in the midst of thermalization, in which case, the rate for that process never quite reaches the opposite edge of the band.
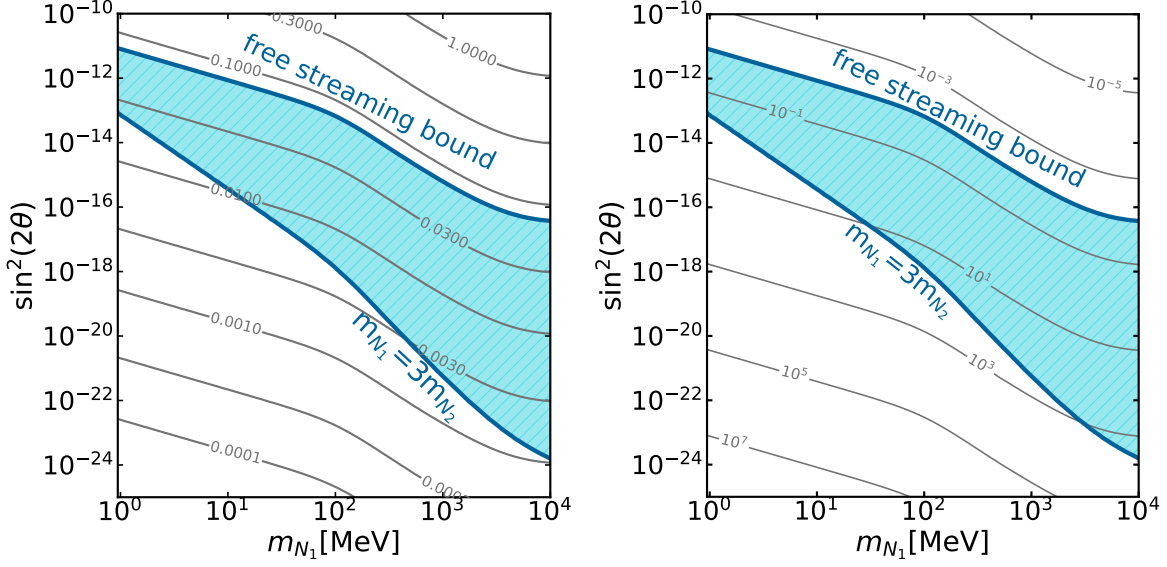
Figure 2.2. Across a parameter space of the heavy sterile neutrino rest-mass (m_{N_1}) and its mixing angle with the active neutrinos ($\sin^2(2\theta)$), the following contours are shown. *Left*: The ratio of the dark sector temperature to the standard model temperature, i.e., T_{DS}/T_{SM}, stemming from the energy injected into the dark sector from scattering-induced decoherence, under the assumption that the dark sector thermalizes with itself. The blue region is where all observational and theoretical bounds are satisfied. *Right*: The mass of N_2 (in MeV) required to account for all of the dark matter in this scenario.

required mass m_{N_2} necessary to make all of the dark matter, given the dark sector temperatures shown in the left panel. It is assumed that the N_1 relic population is converted to N_2 via 2-to-2 scattering, although the results do not qualitatively change as long as the number density is roughly preserved, e.g., if 1-to-3 decays occur instead.

The lower boundary on the colored region in the parameter space shown in Fig. 2.2 comes from the condition that N_1 have a large enough mass to decay into three N_2, i.e. $m_{N_1} > 3m_{N_2}$, which is the regime we restrict ourselves to in this work. The upper boundary of the color region follows from dark matter free streaming considerations, explained below. We choose the upper limit of the N_1 mass range in Fig. 2.2 such that $T_{SM} \gg m_{N_1}$ during the scattering-induced decoherence production period, ensuring N_1 is produced relativistically.

2.5 Discussion

A key feature of this mechanism is that it allows for a larger sterile neutrino dark matter mass. Normally, the mass of the sterile neutrino is bounded from above by the requirement that the dark matter does not decay too fast via its active-sterile mixing. In the proposed mechanism, however, the mixing angle of the dark matter candidate sterile neutrino does not affect its relic abundance, and can therefore be arbitrarily small. On the flip side, this mechanism provides discovery potential for current and future X-ray and γ-ray missions across a much wider range of sterile neutrino masses and mixings. Depending on the mass of N_1, the dark matter mass m_{N_2} in our mechanism can range from $\sim 10\,\mathrm{keV}$–$1\,\mathrm{GeV}$. Many X-ray telescopes have explored some of this parameter space (e.g., [44, 163, 128, 192, 40, 109, 185, 107, 108, 78]), which will be further probed by the upcoming telescopes ATHENA [143] and XRISM [197]. This also motivates searches for dark matter lines at higher energies, beyond the typical range for sterile neutrino dark matter, using telescopes such as NuSTAR [98, 162, 156, 146, 164, 166], HEX-P [129], Fermi-GBM [145] and INTEGRAL-SPI [201, 43]. Moreover, heavier N_2 masses allow for decay channels involving additional particles such as electrons, muons, and pions [82], which may generate a more complicated electromagnetic signature than a narrow line.

On the opposite end, the lower bound on the sterile neutrino DM mass is set by the requirement that free-streaming dark matter should not wash out small-scale structure, that is, its average kinetic energy must not be too large. Since dark sector internal thermalization ensures $T_{\mathrm{DS}} < T_{\mathrm{SM}}$, the sterile neutrino average energy can be considerably lower than in a purely scattering-induced decoherence scenario, resulting in a weaker lower mass bound. For a thermally equilibrated species accounting for all of the dark matter, since $\rho_{\mathrm{DM}} \sim g^\star m T_{\mathrm{DS}}^3$, fixing the mass m and the number of degrees of freedom $g^\star$ also fixes the temperature and therefore the energy spectrum. Small-scale structure observations can therefore place a lower limit on the mass of a thermal dark matter candidate. The current bound is $9.7\,\mathrm{keV}$ at 95% C.L. [141]. For comparison, the corresponding bound for the Dodelson-Widrow scenario can be as strong as

92 keV [203].

The heavy sterile neutrino may in principle be detected in laboratory searches, but unfortunately the mixing angles shown in Fig. 2.2 are too small for any current or upcoming experiments to detect (see Ref. [39] for a review). Furthermore, a number of such experiments rely on detecting the sterile neutrino's SM decay products, which would not be effective in the scenario considered here. However, a possibility that may deserve future exploration is the case where decays into SM products dominate over the dark decay branch. This would necessitate larger mixing angles in order to produce the observed relic abundance, potentially allowing for detection in experiments close to the preferred parameter space shown in Fig. 2.2, such as HUNTER [131] and TRISTAN [136, 20]. Such scenarios could have significant implications for neutrino decoupling and big bang nucleosynthesis [70, 82, 87, 159, 7], pre-big bang nucleosynthesis cosmology [89, 90, 88, 57], as well as energy transport in core-collapse supernovae [83, 54]. The lighter sterile neutrino N_2, if it also mixes with the active neutrinos, could be resonantly produced in a supernova core, affecting the explosion dynamics [101, 102, 24]. To faithfully assess the impact of sterile neutrinos in these environments, a careful consideration of dynamical feedback effects in their production is important [182, 160].

A possible direction for future work could be to explore the case of a lighter dark sector mediator. This would result in more complicated dynamics, including resonances in scattering rates and the possibility of producing the mediator itself. In fact, a lighter mediator with just one sterile neutrino can produce the correct relic abundance at some masses by modifying the typical scattering-induced decoherence production process [45, 31]. Sterile neutrinos with strong self-interactions mediated by lighter scalar fields may reproduce the regimes preferred by scenarios of self-interacting dark matter [179, 167, 188, 86, 132, 19] addressing the small structure problems [138, 148, 149]. Moreover, for certain masses and mixings, a resonance in the sterile neutrino scattering rate could cause dips in the diffuse supernova neutrino background [32].

The phenomenology of sterile neutrino dark matter with additional particle species and/or secret interactions in the dark sector can be quite rich. An extension of this mechanism may

include multiple light sterile species. This could correspond, for example, to a tower of massive Kaluza-Klein modes [3], or other rich dark sectors. If the heaviest of these species is the only one produced in significant abundance through scattering-induced decoherence, its decays into the lighter sterile neutrinos may lead to an arbitrarily cold dark matter spectrum (i.e. for arbitrarily large $g^\star_{\mathrm{DS}}$, see (2.10)). Such a scenario also would potentially provide a multitude of targets, at different masses and mixing angles, for future electromagnetic searches. We conclude that the future of this dark subject could be bright.

2.6   Acknowledgments

Chapter 2, in full, is a reprint of material that has been submitted for publication and appears in preprint as: George M. Fuller, Lukáš Gráf, Amol V. Patwardhan, and Jacob Spisak. Dark population transfer mechanism for sterile neutrino dark matter, 2024. I was the primary investigator and author of this paper.

2.7 Appendix: Scattering-Induced Decoherence

The purpose of this section is to explain how the energy injection rate from the SM plasma into the dark sector is calculated.

The Boltzmann equation that describes the production of a sterile neutrino N via scattering-induced decoherence due to mixing with a single active species α, in the absence of any sterile neutrino self-interaction, is [2]

$$\left(\frac{\partial}{\partial t} - Hp\frac{\partial}{\partial p}\right) f_N = \frac{1}{2}\Gamma_\alpha P(\nu_\alpha \to N)(f_{\nu_\alpha} - f_N). \tag{2.11}$$

f_N and f_{ν_α} are the sterile and active neutrino distribution functions, respectively, and the other variables are as described in the main text. All variables on the RHS depend on time and momentum. The probability to transform an active neutrino into a sterile neutrino is

$$P(\nu_\alpha \to N) = \frac{1}{2}\frac{\Delta^2 \sin^2(2\theta)}{\Delta^2 \sin^2(2\theta) + \left(\frac{\Gamma_\alpha}{2}\right)^2 + (\Delta\cos(2\theta) - V_\alpha)^2}. \tag{2.12}$$

Here $\Delta \approx \frac{m_N^2}{2p}$, θ is the vacuum active-sterile mixing angle, and $\left(\frac{\Gamma_\alpha}{2}\right)^2$ is the quantum damping factor. The key inputs to the calculation, besides the sterile neutrino mass and mixing angle, are the active neutrino scattering rate Γ_α and in-medium potential V_α, both of which depend on the neutrino momentum p and SM plasma temperature T_{SM}.

The active neutrino scattering rate for $T_{\text{SM}} \in [1\text{ MeV}, 10\text{ GeV}]$ is taken from publicly available data files described in section 3 of reference [28]. For $T_{\text{SM}} \in [5\text{ GeV}, 150\text{ GeV}]$, rates are taken from publicly available data files described in section 2 of reference [92]. Note that for this temperature range the approximate scaling $\Gamma_\alpha \propto pT_{\text{SM}}^4$ breaks down and $C_\alpha(p, T_{\text{SM}})$ varies by several orders of magnitude.

The in-medium potential (with negligble lepton number) for $1\text{ MeV} \ll T_{\text{SM}} \ll T_{\text{EW}}$, where T_{EW} is the electroweak scale, is [147]:

$$V_\alpha(p,T) = -\frac{8\sqrt{2}G_F p}{3m_Z^2}\left(n_{\nu_\alpha}\langle E_{\nu_\alpha}\rangle + n_{\bar{\nu}_\alpha}\langle E_{\bar{\nu}_\alpha}\rangle\right)$$
$$-\frac{8\sqrt{2}G_F p}{3m_W^2}\left(n_{l_\alpha}\langle E_{l_\alpha}\rangle + n_{\bar{l}_\alpha}\langle E_{\bar{l}_\alpha}\rangle\right). \tag{2.13}$$

(2.13) represents a leading-order expansion of the W and Z propagators, which works well for calculations involving keV sterile neutrino masses because the production rate peaks around a SM temperature $T_{\text{peak}} \approx 133 \text{ MeV} \left(\frac{m_N}{1\,\text{keV}}\right)^{\frac{1}{3}}$ [2]. For larger masses, production occurs at higher temperatures and the leading-order expansion is no longer a good approximation. In fact, the potential is positive above the EW scale, and the sign change induces a resonance which enhances the production rate [22]. Above the EW scale, the potential takes the form [158]

$$V_a = (3g^2 + g'^2)T_{\text{SM}}^2/(32p), \tag{2.14}$$

where g and g' are the SU(2)$_L$ and U(1)$_Y$ SM gauge couplings, respectively. The two regimes in equations 2.13 and 2.14 may be smoothly connected by the full integral form of the potential described in appendix A of reference [22], which we summarize below. The full form of the potential after EW symmetry breaking is

$$V_\alpha(p,T) = -\pi\alpha_w(B(0,m_Z)/\cos^2(\theta_W)+$$
$$B(m_{l_\alpha},m_W)(2+m_{l_\alpha}^2/m_W^2)). \tag{2.15}$$

Here m_{l_α} is the mass of the charged lepton of flavor α, θ_W is the electroweak mixing angle, and

$$B(m_f,m_A) = \frac{1}{p^2}\int \frac{dk}{8\pi^2}\left[\left(\frac{k\delta m^2}{2E_A}L_2^+(k) - \frac{4pk^2}{E_A}\right)f_B(E_A)\right.$$
$$\left. + \left(\frac{k\delta m^2}{2E_f}L_1^+(k) - \frac{4pk^2}{E_f}\right)f_F(E_f)\right]. \tag{2.16}$$

26

Here $\delta m^2 = m_A^2 - m_f^2$, $f_{B/F}(E_i)$ are Bose-Einstein or Fermi-Dirac distribution functions with energy $E_i = \sqrt{k^2 + m_i^2}$, and

$$L_{1/2}^+(k) = \ln\left(\left|\frac{[\delta m^2 + 2p(k+E_{f/A})][\delta m^2 + 2p(k-E_{f/A})]}{[\delta m^2 - 2p(k+E_{f/A})][\delta m^2 - 2p(k-E_{f/A})]}\right|\right) \tag{2.17}$$

The transition from (2.15) to (2.14) may be achieved by taking $m_{Z,W}^2(T) = m_{Z,W}^2(1 - T^2/T_{\mathrm{EW}}^2)$. At temperatures far below T_{EW}, (2.15) reduces to (2.13).

With the addition of a sterile neutrino self-interaction, the Boltzmann equation for the heavy sterile neutrino may be written as [118]

$$\left(\frac{\partial}{\partial t} - Hp\frac{\partial}{\partial p}\right)f_{N_1} = \frac{1}{2}\Gamma_{\mathrm{tot}}P(\nu_\alpha \to N_1)(f_{\nu_\alpha} - f_{N_1}) + \mathscr{C}_s. \tag{2.18}$$

The total scattering rate is $\Gamma_{\mathrm{tot}} = \Gamma_\alpha + \Gamma_{\phi,2\to2}$, a collision term $\mathscr{C}_s$ describing sterile-only processes has been added, and the potential also gains an additional term from the self-interaction. Furthermore, there is an additional Boltzmann equation for N_2 coupled to (2.18). However, two important facts allow us to ignore these complications: 1) we are in the regime where $\Gamma_{\phi,2\to2} \ll \Gamma_\alpha$ (in order to avoid resonant overproduction [118]), and 2) the dark sector never comes close to being in thermal equilibrium with the SM plasma. The former means that the sterile neutrino contributions to the total scattering rate and potential can be ignored. The latter means we may ignore the impact of the dark sector on the SM and conversions from sterile neutrinos back into active neutrinos, ie $f_{\nu_\alpha} - f_N$ may be replaced by $f_{\nu_\alpha}^{(\mathrm{eq})}$. Therefore the energy injection rate from the SM into the dark sector takes the form shown in the main text, and is decoupled from the dynamics of the dark sector, which simplifies the analysis of the dark sector considerably.

2.8 Appendix: Sterile Neutrino Interaction Rates

The purpose of this section is to explain the values of the sterile neutrino self-interaction rates used in the main text.

The relativistic 2-to-2 sterile neutrino scattering rate is taken to be [118]

$$\Gamma_{\phi,2\to2} \approx 0.03\beta G_\phi^2 pT^4. \tag{2.19}$$

This rate assumes that the sterile neutrino distribution functions are Fermi-Dirac-like $f(E,T) \simeq \beta/(e^{E/T}+1)$, ignores Pauli blocking, and uses average thermal momentum values $p \approx 3.15T$.

The 1-to-3 decay rate ($N_1 \to 3N_2$) is

$$\Gamma_{\phi,1\to3} = \frac{G_\phi^2 m_{N1}^5}{1024\pi^3} \tag{2.20}$$

in the rest frame of N_1 and the limit where m_{N2} is set to zero. To determine if the decay channels enabled by active-sterile mixing are important, this may be compared to the rate for sterile neutrino decay into three *active* neutrinos via active-sterile mixing [33],

$$\Gamma_{3\nu_{\text{active}}} = \frac{G_F^2 m_{N1}^5}{192\pi^3} \sin^2(\theta). \tag{2.21}$$

For larger m_{N_1} other decay channels enabled by active-sterile mixing come into play [82], but for $m_{N1} \leq 10\,\text{GeV}$ the total decay rate is always $\lesssim 20\Gamma_{3\nu_{\text{active}}}$ [66]. Decays into SM products, therefore, are subdominant to the dark sector decay $\Gamma_{\phi,1\to3}$ if $\sin^2(\theta)G_F^2/G_\phi^2 \ll 10^{-2}$. Since the preferred mixing angles we consider are $\sin^2(2\theta) < 10^{-10}$, this is satisfied as long as G_ϕ isn't several orders of magnitude smaller than G_F.

We *approximate* the 2-to-4 rate via naive dimensional analysis as

$$\Gamma_{\phi,2\to4} \sim G_\phi^2 T^4 \Gamma_{\phi,2\to2}. \tag{2.22}$$

It is important to note that an accurate calculation of the numerical prefactor would be required in order to definitively establish the parameter space in which full thermalization is achieved through 2-to-4 processes (rates for some scalar-mediated interactions involving ¿4 neutrinos, including 4-to-2 annihilation, were calculated in reference [100]). If this scenario is of particular interest, a more detailed rate calculation may be a fruitful topic for future work.

Chapter 3

Constraints on axion-like polarization oscillations in the cosmic microwave background with POLARBEAR

3.1 Abstract

Very light pseudoscalar fields, often referred to as axions, are compelling dark matter candidates and can potentially be detected through their coupling to the electromagnetic field. Recently a novel detection technique using the CMB was proposed, which relies on the fact that the axion field oscillates at a frequency equal to its mass in appropriate units, leading to a time-dependent birefringence. For appropriate oscillation periods this allows the axion field at the telescope to be detected via the induced sinusoidal oscillation of the CMB linear polarization. We search for this effect in two years of POLARBEAR data. We do not detect a signal, and place a median 95% upper limit of $0.65°$ on the sinusoid amplitude for oscillation frequencies between $0.02 \, \text{days}^{-1}$ and $0.45 \, \text{days}^{-1}$, which corresponds to axion masses between $9.6 \times 10^{-22} \, \text{eV}$ and $2.2 \times 10^{-20} \, \text{eV}$. Under the assumptions that 1) the axion constitutes all the dark matter and 2) the axion field amplitude is a Rayleigh-distributed stochastic variable, this translates to a limit on the axion-photon coupling $g_{\phi\gamma} < 2.4 \times 10^{-11} \, \text{GeV}^{-1} \times (m_\phi/10^{-21} \, \text{eV})$.

3.2 Introduction

The nature of dark matter, particularly its non-gravitational interactions, remains one of the biggest open questions in cosmology and particle physics. One possibility that has recently received significant attention is low-mass bosonic dark matter [71, 130, 113]. The canonical example is the original QCD axion, a pseudo-Nambu Goldstone boson associated with the spontaneous breaking of a U(1) symmetry proposed to solve the strong CP problem. [154, 153, 193, 195]. More generally, a broader class of pseudoscalar fields with small masses and couplings to the standard model have been considered. These are often called axion-like-particles and are not necessarily solutions to the strong CP problem; nevertheless, we will refer to them as axions in this work for brevity. String theory generically predicts the existence of many such axions populating a wide range of masses and couplings, which is sometimes called the axiverse [26, 184]. Axions with astrophysically large de Broglie wavelengths ($\lambda \sim 1\,\text{kpc}$ for axion mass $m_\phi \sim 10^{-22}\,\text{eV}$) are a particularly intriguing dark matter candidate because of their ability to act as fuzzy dark matter, which can potentially resolve conflicts between small-scale predictions of cold dark matter models and observations [114, 111].

One way to detect axions is via their interaction with electromagnetism. Laboratory experiments such as ADMX [48] and ABRACADABRA [119], for example, exploit the coupling between axions and magnetic fields to set limits on the axion dark matter in the QCD mass range. Reference [115] provides an overview of experimental approaches. It is well known that the coupling between the electromagnetic field and a pseudoscalar field generates an effective birefringence, rotating linearly polarized light [96, 50]. The axion is well modelled as a classical field, which, when the axion mass is less than the Hubble rate, oscillates at a frequency equal to its mass. Fedderke et. al. [74], hereafter F19, pointed out two novel effects in the CMB caused by this oscillation and birefringence. The first is the suppression of the overall CMB polarization signal due to averaging over many axion oscillation periods during recombination, which was constrained in F19. The second is a coherent, all-sky oscillation of the CMB's linear polarization

due to the oscillation of the axion field *at the telescope*. This effect can be constrained when the oscillation period is appropriate for CMB experiments, e.g. hours to years, corresponding to masses in the $10^{-19}\,\text{eV} - 10^{-22}\,\text{eV}$ range. This also happens to be the mass range in which the axion can act as fuzzy dark matter [114]. In this work, we search for this effect using data from the POLARBEAR experiment.

This signal has been constrained by other CMB experiments: BICEP/Keck, in [14, 13] (the latter hereafter BK22), and the South Pole Telescope (SPT) in [75] (hereafter SPT22). Our analysis is similar to these analyses, with two primary differences. The first is that we estimate the CMB polarization angle using C_ℓ^{EB} power spectra rather than in Q/U pixel space. This allows us to use the theoretical C_ℓ^{EE} power spectrum from precisely measured cosmological parameters as a polarization template rather than coadded Q/U maps, and also facilitates easier systematic error checks. The second is that we model the amplitude of the axion field at the telescope as a stochastic, Rayleigh-distributed variable rather than assuming a fixed value corresponding to the mean Milky-Way halo density [79]. The need for this approach was pointed out in [53] and weakens the median constraint on the axion-photon coupling constant by a factor of 2.2 in our analysis.

The birefringence signature generated by axion dark matter can be constrained by other astrophysical polarized sources, and many other authors have used this effect to place constraints in a similar mass range using pulsars, active galactic nuclei, protoplanetary disks, Sagittarius A*, and black hole superradiance [80, 49, 127, 117, 34, 200, 56, 52]. The CMB, however, has several attractive features that make it ideal for this type of analysis. The signal is entirely due to the axion field at the telescope, so we do not require any modelling of the field at the source (during the release of the CMB). The template polarization signal from the CMB has minimal time-dependent contamination and is extremely well measured across many experiments. Finally, POLARBEAR and other CMB instruments have a long history of precision CMB polarization measurements with well-understood noise properties. These factors all serve to mitigate the systematic error in this analysis.

32

In addition to birefringence-based measurements, bounds from cosmological structure like the Lyman-α forest and Milky Way satellites have placed constraints on the minimum allowed axion mass [116, 168, 140] if it is fuzzy dark matter. A constraint on the minimum allowed mass has also been derived from the impact of dynamical heating on the velocity dispersions of ultra-faint dwarf galaxies [61]. These bounds strongly constrain the allowed parameter space for fuzzy dark matter, but are subject to different systematic and modelling uncertainties than birefringence analyses. Upper bounds on the axion-photon coupling which are constant in the mass range we consider have been derived from axion-photon conversion in the Sun, supernova 1987A, quasar H1821+643 and in the intracluster medium [51, 152, 177, 46].

To perform this analysis we use the first two seasons of data from the POLARBEAR experiment, which measured the polarization of the CMB during 2012–2016. During the first two seasons of observations, POLARBEAR observed three small sky patches in order to measure gravitationally lensed *B*-modes. These results were presented in [170] (hereafter PB14) and [169] (hereafter PB17). The telescope has an angular resolution of 3.5 arcmin and reported measurements of the *B*-mode power spectrum up to multipoles of $\ell = 2100$ from the first two seasons, including the angular scales at which the CMB polarization signal is the strongest. POLARBEAR measurements have previously been used to constrain anisotropic birefringence and primordial magnetic fields [17]: this work is entirely seperate, however, because we are searching for *time-dependent* oscillations of the isotropic birefringence angle, whereas [17] considered time-independent birefringence.

The rest of the paper is organized as follows. In Section 3.3, we describe the POLARBEAR instrument and observations. In Section 3.4, we detail the analysis procedure used to generate CMB polarization angles and search for an axion signal. In Section 3.5 and 3.6, we describe the null tests and systematics estimates used to validate the dataset. The results are presented in Section 3.7, and the conclusion in Section 3.8.

3.3 First and Second Season Observations of the POLAR- BEAR **Instrument**

The POLARBEAR experiment consisted of a cryogenic receiver attached to a two-mirror reflective telescope, the 2.5 m Huan Tran Telescope. It was located at the James Ax Observatory in the Atacama Desert in Chile at an elevation of 5,190 m. The receiver contained 1,274 transition-edge sensors arranged into 637 polarization-sensitive pixels situated in 7 detector wafers on the focal plane, which was cooled to 0.3 K, and observed at a single frequency centered at 150 GHz. We will report data from the first and second season observations, which occurred from May 2012 to June 2013 and October 2013 to April 2014, respectively. More details about the POLARBEAR receiver and telescope can be found in [25] and [121].

The POLARBEAR observing strategy during the first and second seasons is described in detail in PB14 and PB17, and will be summarized here. Three separate sky patches were observed, each with an effective sky area of 7–9 square degrees. In this work, an "observation" will refer to a single, continuous measurement of one patch which lasts until the patch is no longer visible, typically 4–8 hours. Each observation consists of many 15-minute constant elevation scans (CESs). During one CES, the telescope scans back and forth in azimuth repeatedly at a constant elevation, and as the sky rotates, the entire patch is observed. The telescope then changes elevation and repeats the process. A typical observing day involves sequentially observing all three patches. This observing strategy allows us to probe oscillation periods longer than about 2 days.

During the first two seasons the telescope observed with a cryogenic half-wave plate (HWP) located on the sky-side of the lenses. During the first season it was periodically rotated between observations in order to mitigate systematic errors, and during the second season it remained fixed. In PB17, it was noted that this generated some uncertainty in the absolute polarization angle of the instrument during the first season and between the two seasons. This source of systematic error limits the maximum oscillation period we can assess to 50 days, as

discussed in Section 3.6.

3.4 Analysis Method

3.4.1 Expected Signal

Following F19, the axion-photon coupling in the Lagrangian can be written as

$$\mathscr{L} = -\frac{1}{4} g_{\phi\gamma} \phi F_{\mu\nu} \tilde{F}^{\mu\nu}, \tag{3.1}$$

where ϕ is the axion field, $g_{\phi\gamma}$ is the axion-photon coupling, $F_{\mu\nu}$ is the electromagnetic field tensor and $\tilde{F}^{\mu\nu}$ is its dual. Assuming that the amplitude is small enough so the potential is well-approximated by $V(\phi) = m_\phi^2 \phi^2 / 2$, the axion field at the telescope is well-described by $\phi(t) = \phi_0 \sin(m_\phi t + \theta)$. We treat the amplitude ϕ_0 and phase θ as constants because the duration of the experiment is much less than the axion coherence time, as discussed in Section 3.7.3. The polarization angle of the CMB due to the axion field at the telescope is then (F19)

$$\beta_{\text{CMB}}(t) = \frac{g_{\phi\gamma}\phi_0}{2} \sin(m_\phi t + \theta). \tag{3.2}$$

This can be conveniently parameterized as

$$\beta_{\text{CMB}}(t) = A \sin(2\pi f t + \theta). \tag{3.3}$$

This is a sinusoid with unknown amplitude A, frequency f, and phase θ. The basic unit of time in the POLARBEAR survey schedule is one observation of a single patch, which can last up to 8 hours. For each observation, therefore, we construct CMB maps and estimate a single angle, generating several hundred angles over the course of the two years of data. We will then form a likelihood to search for the presence of a sinusoidal signal in this data.

3.4.2 Angle Estimation Procedure

There are multiple ways to estimate a rotation angle from the observation maps. The most direct way is to search for the rotation in the Stokes Q and U parameter maps by comparing them to a template of Q and U maps containing only the unrotated CMB. This is the method employed in BK22 and SPT22. Another way is to transform the Q and U maps into E-mode and B-mode maps, then use a single-observation C_ℓ^{EB} spectrum to estimate a rotation angle. While the latter method has the disadvantage of requiring more computationally-intensive steps, we choose to implement it for the following reasons. The first is that we can use the extremely well-determined theoretical C_ℓ^{EE} from other experiments as our polarization template, rather than a Q/U template map created by coadding our observations. While the C_ℓ^{EE} template is affected by sample variance, this effect is not important for the ℓ range we use. The second advantage is that the power spectra approach is very similar to the approach taken in the construction of the full, coadded spectra in PB17. This lets us re-use most elements of this validated pipeline, including many of the same systematics estimates.

The method of estimating a time-independent rotation angle using the C_ℓ^{EB} power spectrum is well established [120], and has been used in many analyses, including PB17, to correct for an overall telescope miscalibration angle. The method we will employ to search for a *time-varying* rotation angle is similar, except that we must construct a spectrum for every observation. This will be used to estimate a single rotation angle for each observation, constant over the duration of the observation. We can then search for a time-varying signal in the timestream of these angles. For a single observation with CMB rotation angle α, in the absence of noise and foreground contamination (which are addressed in Section 3.4.5 and Section 3.6.3 respectively), the observed Fourier transformed E/B-mode coefficients are

$$E_{\ell m}^{\text{obs}} = \cos(2\alpha)E_{\ell m}^{\text{CMB}} - \sin(2\alpha)B_{\ell m}^{\text{CMB}} \tag{3.4}$$

$$B_{\ell m}^{\text{obs}} = \sin(2\alpha)E_{\ell m}^{\text{CMB}} + \cos(2\alpha)B_{\ell m}^{\text{CMB}}. \tag{3.5}$$

This analysis is sensitive to signals of amplitude $\approx 1°$, so we use the small angle approximation

$$E_{\ell m}^{\text{obs}} = E_{\ell m}^{\text{CMB}} - 2\alpha B_{\ell m}^{\text{CMB}} \tag{3.6}$$

$$B_{\ell m}^{\text{obs}} = 2\alpha E_{\ell m}^{\text{CMB}} + B_{\ell m}^{\text{CMB}}. \tag{3.7}$$

Since the CMB is E-mode dominated, to leading order all of the rotation information is contained in the $2\alpha E_{\ell m}^{\text{CMB}}$ term in (3.7). In order to recover an angle from a single observation, then, we can construct a power spectrum using one B-mode map correlated with the full, coadded E-mode maps. The spectra for observation j, rotated by angle α_j, is

$$
\begin{aligned}
C_{\ell,j}^{EB,\text{obs}} &= \frac{1}{N}\frac{1}{(2\ell+1)}\sum_i^N \sum_m E_{\ell m,i}^{\text{obs}}(B_{\ell m,j}^{\text{obs}})^* \\
&= 2\alpha_j C_\ell^{EE,\text{CMB}}.
\end{aligned}
\tag{3.8}
$$

The E-mode maps have been coadded over all observations $i = 1,\dots,N$. The intrinsic $C_\ell^{EB,\text{CMB}}$ has been set to zero, and we have neglected $C_\ell^{BB,\text{CMB}}$ because it is $\ll C_\ell^{EE,\text{CMB}}$.

3.4.3 Mapmaking

The mapmaking procedure is nearly identical to the one used in "Pipeline A" of PB17, and will be briefly reviewed here. To make maps of the polarized sky, the raw time-ordered data (TOD) undergo a series of quality cuts, are converted to CMB temperature units, and

then differenced to form polarization timestreams. The timestreams are filtered to remove high and low frequency noise as well as scan-synchronous signals then combined with the detector pointing data to make maps. The maps are apodized with noise-weighted masks, which cover point sources as well. This procedure yields a single Q and U map for each observation. Finally, Q and U maps are transformed to E and B maps using the pure B-mode transform [178]. Due to the filtering, they are biased estimates of the true sky signal.

The chief difference between the maps used in this analysis and those in PB17 is the apodization. PB17 uses a separate mask for each observation, whereas this analysis uses one apodization mask common to every observation within each patch. This is done in order to simplify the calculation of the mode-mixing matrix, discussed in Section 3.4.4. However, this masking procedure does sub-optimally weight each pixel within a given observation, leading to an increase in noise. In some observations the increase in noise from edge pixels is excessive, and they are removed from the analysis if the map noise increase exceeds a certain threshold. The same cut is applied to observations that have excessive noise on one split in a null test as well, as described in Section 3.5.1. The overall impact of this apodization procedure is an effective noise increase of about 15%. Improving the apodization procedure to lessen this noise hit is an area of improvement for future analyses.

3.4.4   Maps to Spectra

The procedure to construct single-observation C_ℓ^{EB} spectra as outlined above is identical to PB17, with the modification that only one B-mode map is used per observation. The co-added E-mode maps and a single B-mode map are used to construct pseudospectra ($\tilde{C}_\ell$), which are biased estimates of the true spectra:

$$\tilde{C}_{\ell,j}^{EB} = \frac{1}{N_\ell} \sum_{k \in \mathrm{bin}_\ell} \tilde{m}_{jk}^{B*} \left(\frac{1}{\sum_{i \neq j} w_i} \sum_{i \neq j} w_i \tilde{m}_{ik}^{E} \right). \tag{3.9}$$

The $\tilde{m}_{jk}$ denotes a Fourier-transformed map with 2D wavevector k and observation j. The flat-sky approximation is used due to the size of the POLARBEAR patches, and the spectra are combined into ℓ bins of width $\Delta\ell = 40$. N_ℓ is the number of wavevectors in bin ℓ. The term in the parentheses represents the coadded E-mode map, with observation weights w_i. Observation j is removed from the coadd to eliminate noise bias, since noise is assumed to be uncorrelated between observations.

The estimated true spectra ($\hat{C}_b$) are calculated from the pseudospectra using

$$\hat{C}^{EB}_{b,j} \equiv \sum_{b'} K^{-1}_{bb',j} P_{b'\ell} \tilde{C}^{EB}_{\ell,j} \tag{3.10}$$

and

$$K_{bb',j} = \sum_{\ell\ell'} P_{b\ell} M_{\ell\ell',\text{patch}} F_{\ell',j} B^2_{\ell'} Q_{\ell'b'}. \tag{3.11}$$

All variables in this calculation have the same meaning as in PB17 but some are re-calculated for this analysis. The mode-mixing matrices $M_{\ell\ell',\text{patch}}$ correct for the effects of apodization and are calculated analytically for each patch using the patch apodization mask, discussed in Section 3.4.3. The filter transfer functions $F_{\ell',j}$ correct for the effects of time-domain filters for observation j, B_ℓ corrects for the beam, and $P_{b\ell}$ and $Q_{\ell'b'}$ are binning matrices. There are four bins b centered at $\ell = [700, 1100, 1500, 1900]$, each of width $\Delta\ell = 400$.

3.4.5 Spectra to Angles

Since the noise between different observations is uncorrelated, the noise between different C^{EB}_ℓ spectra is also uncorrelated. We will neglect the impact of foregrounds in the angle estimation: all three patches were chosen to have low foregrounds, and this systematic effect is discussed in Section 3.6.3. The estimated rotation angle $\hat{\alpha}_j$ for observation j is then obtained by minimizing
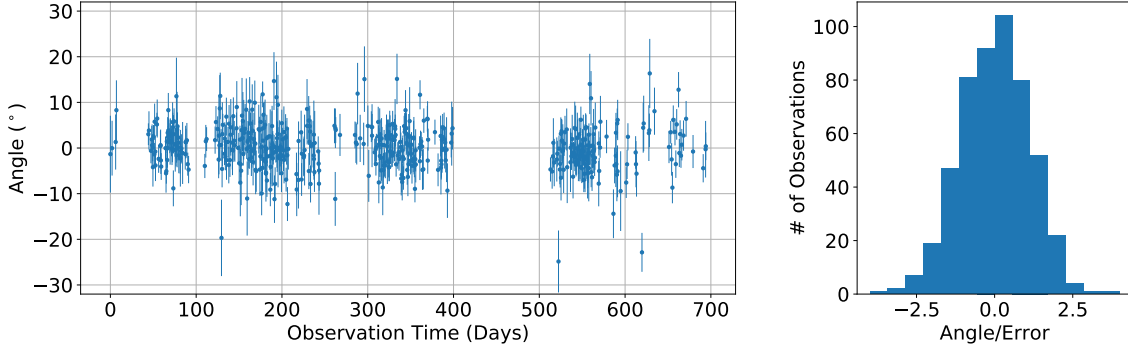
Figure 3.1. *Left*: The 515 estimated per-observation rotation angles $\hat{\alpha}_j$ used in this analysis. *Right*: A histogram of the angles normalized by their error, $\hat{\alpha}_j/\sigma_j$. The angles are Gaussian distributed.

$$\chi^2(\hat{\alpha}_j) = \sum_{bb'} (\hat{C}_{b,j}^{EB} - 2\hat{\alpha}_j C_b^{EE,\text{th}})(V_{bb'}^{EB})^{-1}(\hat{C}_{b'j}^{EB} - 2\hat{\alpha}_j C_{b'}^{EE,\text{th}}). \tag{3.12}$$

The theoretical power spectrum $C_{b'}^{EE,\text{th}}$ is calculated from the WMAP 9-year data. We use WMAP rather than Planck data because there are negligible differences for the purpose of our analysis and the WMAP results are already integrated in our pipeline. The covariance matrix $V_{bb'}^{EB}$ is calculated from 500 simulated maps that contain ΛCDM signal and instrumental noise. These simulated maps are generated by constructing maps containing only ΛCDM signal and scanning them into TOD. White noise from the PB17 noise model is added before running the maps through the full analysis pipeline. These simulations are also used to generate an error term σ_j for each observation, which is the standard deviation of all simulated angles for that observation. This construction includes the effect of sample variance, which is not relevant for our analysis because we make many observations of the same fixed CMB realization. The effect is negligible, however, because the angle error from sample variance alone is at least $16\times$ smaller than the total statistical error for each observation. The set of angles used in this analysis is shown in Figure 3.1.

As in PB17, the absolute polarization angle of the instrument is calibrated using the *EB*-derived angle coadded across both seasons. This means that the weighted mean angle in this

40

analysis is fixed to zero. While other non-*EB* calibration sources exist, this procedure, described in [120], is the most accurate way to calibrate the instrument. We show in Section 3.4.6 that this absolute polarization angle calibration has a negligible effect on our analysis.

The TOD filtering causes *E*-mode power to leak into *B*-mode maps, which can be estimated via simulation. 100 simulations of maps containing only CMB C_ℓ^{TT} and C_ℓ^{EE} power are run through the pipeline and used to construct $\hat{C}_{b,j}^{EB}$. A small amount of leakage is detected. It is less than 6% of the statistical error for any angle, resulting in a negligible $<0.01°$ bias at any axion frequency probed in this analysis, and so we ignore its impact.

3.4.6   Likelihood

The noise between observations is assumed to be uncorrelated, and the errors on each angle Gaussian. The likelihood for the sinusoid parameters is then

$$\mathscr{L}(A, f, \boldsymbol{\theta}) \propto e^{-\frac{1}{2}\chi^2(A, f, \boldsymbol{\theta})} \tag{3.13}$$

where

$$\chi^2(A, f, \boldsymbol{\theta}) = \sum_j^N \frac{(\langle s_j \rangle - \hat{\alpha}_j)^2}{\sigma_j^2}. \tag{3.14}$$

The index j represents a single observation, and the signal $\langle s_j \rangle$ is defined below. The likelihood normalization factor $\prod_j^N \sigma_j \sqrt{2\pi}$ is dropped because we are only interested in relative likelihoods. Observations which have σ_j at least two times larger than the mean value are discarded, since they contribute negligibly to the likelihood and are more likely to have systematic errors. This removed 23 observations, which constituted $<0.5\%$ of the statistical weight of the dataset. This leaves $N = 515$ angles available for the analysis.

The signal $\langle s_j \rangle$ must be averaged over the duration of each observation:

$$\langle s_j \rangle = \frac{1}{t_j^{\text{end}} - t_j^{\text{start}}} \int_{t_j^{\text{start}}}^{t_j^{\text{end}}} dt \, A \sin\left(2\pi f t + \theta\right)$$

$$= A \, \text{sinc}(\pi f \Delta t_j) \sin(2\pi f \bar{t}_j + \theta). \tag{3.15}$$

$\Delta t_j \equiv t_j^{\text{end}} - t_j^{\text{start}}$ is the observation duration and $\bar{t}_j \equiv (t_j^{\text{end}} + t_j^{\text{start}})/2$ is the middle of the observation time. The effect of averaging is to wash out signals with oscillation periods that are shorter than the 4–8 hour observation periods.

Frequency Domain

The frequency domain for our search is

$$0.02 \, \text{days}^{-1} \leq f \leq 0.45 \, \text{days}^{-1}. \tag{3.16}$$

The dataset spans 694 days, so we are able to probe sinusoidal periods out to approximately that length. However, as explained in Section 3.6, uncertainty in the relative HWP angle between the two seasons may show up as a low-frequency signal, leading us to set a minimum frequency of $0.02 \, \text{days}^{-1}$. The maximum frequency is set to $0.45 \, \text{days}^{-1}$ because the typical time-spacing between observations of a single patch is one day. This causes a significant loss in sensitivity around a frequency of $0.5 \, \text{days}^{-1}$, as well as integer multiples of this frequency. Furthermore, at frequencies higher than $0.5 \, \text{days}^{-1}$ the averaging effect in (3.15) reduces the amplitude of the signal beyond the level of a few percent. For these reasons, we choose to only analyze frequencies up to $0.45 \, \text{days}^{-1}$.

We assess the likelihood at a set of 1,492 evenly-spaced frequencies. In the absence of noise, this allows the likelihood estimator to recover an injected signal at any frequency to within 5% of the correct amplitude. This results in a frequency resolution about 5 times smaller than $1/694 \, \text{days}^{-1}$, which is the spacing that a Discrete Fourier Transform of the same length

42

of data would have. As a result, likelihood results from neighboring frequencies are highly correlated. This does not pose an issue for our analysis because we compare the results to simulated distributions which do not assume independence between different frequencies.

Effect of Absolute Polarization Angle Calibration

As described in Section 3.4.5, the absolute polarization angle of the instrument is calibrated by setting the weighted mean angle to zero. This means that our analysis is not sensitive to a static birefringence angle. To first order this is not an issue because we are searching for an oscillatory signal. However in the presence of such a signal, there will generally be some small shift in the mean angle caused by a partial oscillation. This shift is removed by the mean angle subtraction. This effect only becomes significant when there is $\lesssim 1$ oscillation period in the entire dataset. Our maximum period is 50 days, which corresponds to about 14 oscillation periods over the 694-day duration of our dataset. Therefore the subtraction in mean angle has negligible impact on the recovery of the signal amplitude.

3.5 Null Tests

We run a series of null tests to check for systematic errors in our analysis before unblinding the data. The data are split along 15 possible sources of potential contamination, differenced to cancel any true signal, and tested for the presence of systematics. Twelve of the splits are the same as in PB17: "moon distance", "sun distance", "rising vs. setting", "high vs. low PWV (Precipitable Water Vapor)", "high vs. low elevation", "high vs. low gain", "sun above or below horizon", "1st vs. 2nd season", "1st vs. 2nd half of dataset", "left- vs. right-going scans", "left vs. right side of the focal plane", and "pixel polarization type". We also add three new patch null tests, which pair two patches together in all three possible ways. Each split in these tests contains only the angles that were made from the *B*-mode maps from that patch, allowing us to probe for differences between patches.

3.5.1 Methodology

Two sets of angles are constructed for each test, one per split. The angles are constructed following the procedure in Section 3.4, with the following modifications:

- The *B*-mode maps contain only data from the split. This means that each map may contain less data or be eliminated altogether.

- For each split, a new map apodization mask is constructed per patch. These masks reflect differences in map coverage for each split. There are a few observations that have excessive noise in the unmasked region of some splits, and therefore cannot be null-validated. These observations' *B*-mode and *E*-mode maps are excluded from the analysis in this paper, as described in Section 3.4.3.

For each split, *all* of the *E*-mode map data is used to construct C_ℓ^{EB}, not just data from the split. This is because we wish to test for time-dependent systematic issues with the *B*-mode maps, and consider the coadded *E*-mode map validated in previous analyses (PB17).

A set of null statistics are computed for each test. For each of the two sets of angles '1' and '2', at each frequency f, we find the maximum likelihood estimation (mle) of the amplitude A^{mle} and phase θ^{mle} that maximizes $\mathscr{L}(A, f, \theta)$. The null statistic at a given frequency is

$$T_{\text{null}}(f) \equiv \frac{|A_{\text{null}}(f)|^2}{\sigma\left(\Re(A_{\text{null}}(f))\right)^2} \tag{3.17}$$

where

$$A_{\text{null}}(f) \equiv (A_1^{\text{mle}} e^{i\theta_1^{\text{mle}}} - A_2^{\text{mle}} e^{i\theta_2^{\text{mle}}})(f). \tag{3.18}$$

The T_{null} can be thought of as a generalization of the difference of two discrete Fourier transforms: the correspondence would be exact if we had instantaneous observations evenly spaced in time and equally weighted. The normalization factor $\sigma\left(\Re(A_{\text{null}})\right)$ is calculated using 500 simulations and ensures that $T_{\text{null}}(f)$ is distributed approximately as chi-squared with 2 degrees of freedom.

This is because $\Re(A_{\text{null}})$ and $\Im(A_{\text{null}})$ are both distributed approximately as Gaussians with the same variance and zero mean. We do not rely on these analytic distributions since we compare the results to simulations, but we do rely on the normalization to allow for fair comparison across different tests and frequencies.

We calculate T_{null} at $f = 0$ for the 10 tests out of 15 that have associated periods within the frequency range of this search. This statistic is simply the difference in the weighted mean angles between the two splits. We include it because differences in mean angle between two splits could cause a spurious signal with a period associated with the split: for example, a difference in angle caused by the moon distance could generate a signal aligned with the ~ 28 days synodic cycle. Five tests are omitted from the $f = 0$ analysis. "1st vs. 2nd season" and "1st vs. 2nd half of dataset" are excluded because the associated period is much longer than our maximum period of 50 days. The "left- vs. right-going scans", "left vs. right side of the focal plane", and "pixel polarization type" are excluded because both splits contain all observations, so a difference in mean angle would not generate a time-dependent signal. In total, there are 22390 T_{null} values: 1492 frequencies from Section 3.4.6 for each of the 15 tests, and $f = 0$ for 10 tests.

3.5.2   Pass Criteria

There are two pass criteria that need to be satisfied in order to pass the null tests. The first, "pass criteria #1," assesses failure in individual parts of the null test suite. The second, "pass criteria #2," uses Kolmogorov-Smirnov (KS) tests to assess uniformity of all null suite probabilities.

Using T_{null}, five probability-to-exceed (PTE) values are computed. The lowest PTE among the five, $P_{\text{low}}^{\#1}$, is compared to a distribution generated from 500 simulations to calculate a global significance value, $\text{PTE}(P_{\text{low}}^{\#1})$. Pass criteria #1 requires more than 5% of simulations to have a lower 'lowest of five PTEs' value than $P_{\text{low}}^{\#1}$: i.e. $1 - \text{PTE}(P_{\text{low}}^{\#1}) > 0.05$.

The five PTE values are shown in Table 3.1, and are:

1. $\max_{t,f} T_{\text{null}}$: The maximum T_{null} value across all tests and non-zero frequencies. This tests

Table 3.1. The five null test PTE values used in the pass criteria #1.

PTE statistic	Description	PTE
$\max_{t,f} T_{\text{null}}$	Spurious axion signal	0.032
$\sum_{t,f} T_{\text{null}}$	Total chi-square	0.062
$\max_t \sum_f T_{\text{null}}$	Bad test	0.060
$\max_f \sum_t T_{\text{null}}$	Bad frequency	0.246
$\max_t T_{\text{null}}(f = 0)$	Mean angle offset	0.192

for the presence of a systematic sinusoidal signal.

2. $\sum_{t,f} T_{\text{null}}$: The total chi-square value over all tests and non-zero frequencies, which assesses noise mis-estimation.

3. $\max_t \sum_f T_{\text{null}}$: The maximum per-test total chi-square value, which assesses issues with an individual test.

4. $\max_f \sum_t T_{\text{null}}$: The maximum per-frequency total chi-square value, which assesses issues with an individual frequency.

5. $\max_t T_{\text{null}}(f = 0)$. The maximum difference in mean angle offset over the ten $f = 0$ null tests.

The first four PTEs are calculated using only non-zero frequencies.

Three PTE values are computed using KS tests, and pass criteria #2 is satisfied if more than 5% of simulations have a lower value than $P_{\text{low}}^{\#2}$: i.e. $1 - \text{PTE}(P_{\text{low}}^{\#2}) > 0.05$. Here $P_{\text{low}}^{\#2}$ is the lowest of the three PTEs. These tests assess whether the probabilities of getting various T_{null} values follow a uniform distribution. The KS test inputs and PTE results are shown in Table 3.2. The probability value returned by the KS test cannot be used to assess significance, since correlations between null tests result in a slightly non-uniform distribution of individual probabilities. Instead, the value of the KS statistic itself is compared to simulations.

Table 3.2. The three null test PTE values used in the pass criteria #2.

Axion KS Test inputs	Description	Number of inputs	PTE
$\mathrm{PTE}_{f,t}(T_{\mathrm{null}})$	Overall	22380	0.128
$\mathrm{PTE}_f(\sum_t T_{\mathrm{null}})$	Per frequency	1492	0.122
$\mathrm{PTE}_t(\sum_f T_{\mathrm{null}})$	Per test	15	0.190

3.5.3 Null test results

For pass criteria #1, $1 - \mathrm{PTE}(P^{\#1}_{\mathrm{low}}) = 0.124$. For pass criteria #2, $1 - \mathrm{PTE}(P^{\#2}_{\mathrm{low}}) = 0.148$. Both are greater than 0.05, and so the null tests pass.

While the null tests pass our stated criteria, all of the PTE values are relatively low. This is potentially indicative of a systematic issue, which we investigated. The low PTEs do not appear to be caused by particular null splits or frequency ranges. Two of the PTEs in Table 3.1 ('bad test' and 'bad frequency') explicitly look for the worst test and frequency, and were not discrepant enough to fail pass criteria #1. Pass criteria #2 is sensitive to non-uniformities in the T_{null} distribution and also passed. In addition to these summary statistics, visual inspection of the full set of T_{null} values plotted for each test and frequency do not reveal large asymmetries between different null splits and frequency ranges. A set of correlated, low PTEs is not surprising given a high total chi-square value. The real data has a total chi-square value 20% larger than the simulation average. This is larger than all but 6% of simulations as shown in Table 3.1. Simulations with such a large total chi-square value have the overwhelming majority of their PTE values less than 0.2.

A high total chi-square value could indicate a problem with the noise model. The noise model is based on Monte-Carlo simulations of white noise timestreams, as described in PB17. It was validated on the full coadded spectra, so we do not expect it to be a source of error. However, to check for noise mis-estimation, we computed a set of angles using a different 100 realizations of signflip noise B-mode maps, which are created by randomly reversing the sign of the maps made for each 15 minute CES. This cancels out the true signal but maintains the noise properties

of the real data. We compared $\sigma\left(\Re(A_\text{null})\right)$ from signflip simulations to those computed using Monte-Carlo noise simulations, and found they agreed to within 5%, and in the wrong direction to alleviate the total chi-square tension. Having found no obvious discrepancy under a different noise model, and with the null tests having passed our pre-determined criteria, we decided that a somewhat elevated total chi-square value would not prevent us from unblinding the data.

3.6   Systematic Errors

In this section we examine the impact of several sources of systematic error, including uncertainty in the position of the HWP, any differences in average angle between the three observing patches, and foregrounds. Although we rely on some of the systematic pipeline used in PB17, our analysis is fundamentally different because we are looking for *time-dependent* sources of error. Systematics that provide a constant C_ℓ^{EB} offset are irrelevant. Therefore many of the PB17 systematics are of no concern, while two others, the HWP and differences between patches, require careful consideration.The typical maximum likelihood sinusoid amplitude generated by statistical noise alone is $0.26°$. Therefore any oscillatory systematic that generates an amplitude much less than $0.26°$ should have negligible impact on the limits in this work.

3.6.1   HWP Position Uncertainty

As discussed in Section 3.3, angle errors that are introduced by the stepped rotation of the HWP during the first observing season are a significant source of time-dependent uncertainty. The HWP angle was changed about 60 times during the first half of the first season, 4 times during the second half of the first season, and was then fixed for the second season. During each rotation the HWP was commanded to rotate in increments of $11.25°$. However, when examining the polarization angles derived from an alternative calibration source, the Crab Nebula (Tau A), it became clear that the angles during the first season exhibited larger variance than during the second season. Furthermore, there was an offset in angle between the two seasons. Both phenomena could be explained if the HWP did not step exactly to the commanded position

each time. While the exact HWP-induced offset at each step is unknown due to statistical error on the Tau A measurements, PB17 found that the discrepancy could be explained by adding a systematic error of $0.56°$ for each step, corresponding to a typical HWP offset of $0.28°$, in quadrature with the statistical error.

This systematic is highly important for this analysis because it corresponds to an unknown time-dependent shift in the instrument polarization angle, which could mimic an axion-generated birefringence signal. The HWP-induced offset between the first and second seasons, for example, is degenerate with a signal with a period of one year. To assess the impact at higher frequencies, we ran 500 simulations where a random angle offset, drawn from a Gaussian distribution with $\sigma = 0.56°$, was assigned to each HWP angle. Then we generated timestreams where each observation's CMB angle corresponded to the offset given by the HWP angle. The maximum likelihood sinusoid amplitude was then estimated at each axion frequency.

The result is shown in Figure 3.2. At high frequencies the HWP rotation cadence doesn't correspond to any specific frequency. Since observations have a statistical error of at least $2°$ and the typical HWP offset is $0.56°$, the impact at high frequencies is minimal. On average these offsets cause only a $1-2\%$ increase in the maximum likelihood amplitude estimate at a given frequency relative to statistical noise alone, and so we ignore the impact of this HWP offset noise in our likelihood. At low frequencies, however, the last few HWP steps in the first season and the offset between the first and second seasons begin to translate into larger sinusoidal signals. We emphasize that because the exact HWP-induced offset at each step is unknown, the numbers shown in Figure 3.2 are only indicative of the average effect we expect, not the true effect present in our data. Because the HWP step cadence begins to generate larger systematic issues at periods >50 days, there is a higher potential to generate a signal that would cause false detection. Based on these results, we chose to set 50 days as the longest period we analyze.

It is possible that the HWP offsets follow a more pathological model than what we assume and mimic a sinusoidal signal at some frequency in our domain. The "1st half vs 2nd half" null test described in Section 3.5 tests for this, because the time periods align with when the
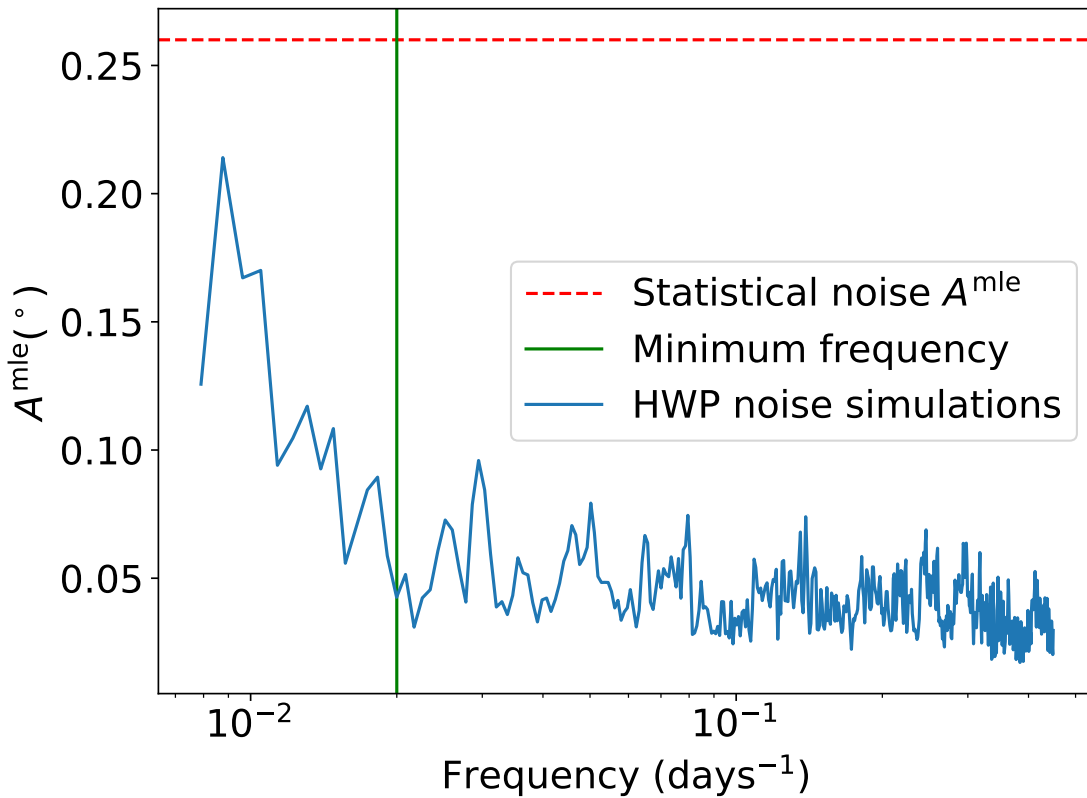
Figure 3.2. The estimated typical maximum likelihood amplitude signal of the HWP angle offsets. 500 simulations containing only random offset angles were generated and run through the likelihood. The median recovered amplitude is shown here. The HWP step cadence begins to generate larger systematic issues at periods >50 days. Based on these results, the maximum period used in this analysis is 50 days.

HWP was stepped vs. fixed. As stated in that section, there is no signal observed in this null test.

3.6.2 Differences in Patch Mean Angle

Since a typical day involves observing all three patches sequentially, any differences in the mean angle of each of the three patches could generate an oscillatory signal with a period of one day. However, as explained in Section 3.4.6, our upper frequency bound is $0.45\,\mathrm{days}^{-1}$ and so we are not sensitive to this signal. However, variations in the observing sequence can generate signals at other frequencies, and simulations of patch mean angle offsets reveal a transfer of $\leq 12\%$ of any offset into any frequency in domain we do observe. Fortunately, our null tests directly calculate the difference in mean angle between patches. Since they are consistent with simulations, which do not contain foreground power, we do not see evidence for any foreground or systematic patch mean angle differences.

One known effect that will cause offsets between the patch mean angles is sample variance, because each patch has an independent sample-variance-induced C_ℓ^{EB} signal. This effect is included in the ΛCDM simulations, but if it were large we would need to correct for its effects. It can be calculated both analytically and through simulations, and in each patch, the error from sample variance is $\sigma \approx 0.12°$. This is $3\times$ smaller than the statistical error alone on each patch mean angle. Furthermore, since the patch mean angle offsets transfer $\leq 12\%$ into any given frequency, the typical A^{mle} generated by cosmic variance is a negligible $\lesssim 0.01°$.

3.6.3 Foregrounds and Other Instrumental Systematics

Any C_ℓ^{EB} contribution from dust and synchrotron radiation should be time-independent and simply contribute to the patch mean angle differences. These differences were addressed in Section 3.6.2. Point sources may be variable in time, but the strongest are masked as discussed in PB17.

PB17 also makes many other estimates related to the calibration, analysis effects, and known instrumental systematics. We expect the multiplicative effects to have a similar impact

on the C_ℓ^{EB} spectrum as they do on the C_ℓ^{BB} spectrum, which PB17 determined was 6%. Since the angle estimates are linear in C_ℓ^{EB}, we would then roughly expect a overall 6% uncertainty on amplitude estimation. Since this is relatively small and does not bias our results, this is negligible uncertainty in our reported results.

The other instrumental systematics deal with effects that could potentially cause spurious additive C_ℓ^{EB}, including differential gain, gain drift, differential beam size, differential ellipticity, differential pointing, boresight pointing, and electrical crosstalk. These can impact our analysis if they generate a time-dependent C_ℓ^{EB}. An analysis of C_ℓ^{EB} bias was done in PB14, which noted that all sources provided $\lesssim 0.02°$ bias in the coadded spectra. Using a combination of analytic estimates [174] and simulations, we modified the analysis to account for per-observation C_ℓ^{EB} and determined that all such sources were either time-independent or provided a negligibly small time-dependent contribution as compared to the statistical noise.

3.7 Results

We search for the presence of a sinusoidal signal, and finding no statistically significant indication, place appropriate bounds over the frequency range of the search. By accounting for the axion field amplitude at the telescope, these translate to bounds on the axion-photon coupling over a range of axion masses.

3.7.1 Search for a Signal

In order to detect a signal, we form a test statistic $\Delta\chi^2$ which is large in the presence of a sinusoidal signal above the background. For each frequency in the discrete frequency domain, the MLE phase and amplitude are found, and the difference relative to the χ^2 with no signal is calculated:

$$\Delta\chi^2(f) \equiv \chi^2(A=0) - \chi^2(A^{\mathrm{mle}}(f), f, \theta^{\mathrm{mle}}(f)). \tag{3.19}$$
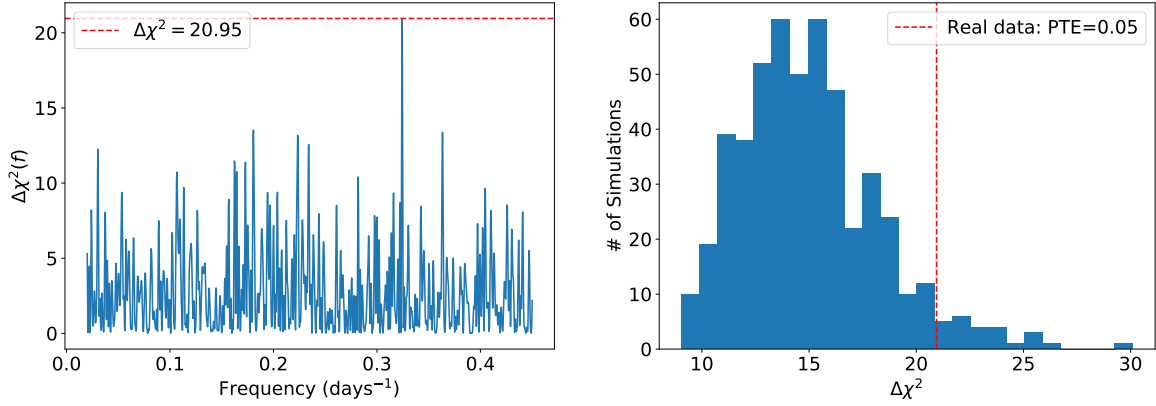
Figure 3.3. The significance test for the presence of an axion signal. *Top*: The calculation of $\Delta\chi^2$. For each frequency in the discrete frequency domain, the MLE phase and amplitude are found, and $\Delta\chi^2(f)$ is calculated. $\Delta\chi^2$ is the largest among these. *Bottom*: The significance of $\Delta\chi^2$ as compared to a set of 500 simulations.

The test statistic is the largest $\Delta\chi^2(f)$ among all frequencies:

$$\Delta\chi^2 \equiv \max_f(\Delta\chi^2(f)). \tag{3.20}$$

This statistic is optimal in the Neyman-Pearson sense in that it maximizes the probability of rejecting the no-signal hypothesis if the alternative hypothesis of a sinusoidal signal is true [196]. The distribution of the statistic is approximately chi-squared, but we do not rely on this, instead comparing to a distribution of test statistics computed from 500 ΛCDM + noise simulations. The p-value is the fraction of background simulation test statistic values that exceed that of the real data.

The selection of $\Delta\chi^2$ and its location relative to the distribution is shown in Figure 3.3. The real data has a p-value of 0.048, corresponding to 1.7σ significance. While this p-value is relatively small, it is not significant enough to claim detection of a signal above the noise background. Future analysis of the remaining three seasons of POLARBEAR will aid in determining if this result is simply a statistical fluctuation.

When assessing the significance of a result with many trials, in this case discrete fre-

quencies, it is often useful to report the experimental sensitivity. This is defined as the signal amplitude which would produce a detection at some significance level. We can approximate the $\Delta\chi^2$ required for any significance level by applying a fit to the distribution shown in the bottom of Figure 3.3. A 3σ detection (PTE = 0.0013) would require $\Delta\chi^2 = 28.5$, yielding an experimental sensitivity of $A(3\sigma) = 1.15°$. The 5σ (PTE $= 2.8 \times 10^{-7}$) experimental sensitivity is $A(5\sigma) = 1.43°$.

3.7.2 Upper Limit

As we do not detect a globally significant axion-like oscillation, at each frequency we compute a frequentist upper limit on the signal amplitude at 95% confidence level. The likelihood for the amplitude as a function of frequency is

$$\mathscr{L}_A(A,f) = \int_0^{2\pi} d\theta \mathscr{L}(A,f,\theta) P(\theta), \tag{3.21}$$

with a uniform probability distribution for the phase

$$P(\theta) = \frac{1}{2\pi}, \ 0 \le \theta < 2\pi. \tag{3.22}$$

We construct confidence intervals following the Neyman procedure [196] with the following ordering: intervals $[0, A^{95}(f)]$ are defined with an upper limit $A^{95}(f)$ at each frequency f such that

$$P(A^{\mathrm{mle}} \le A^{\mathrm{mle}}_{\mathrm{obs}} | A^{95})(f) = 0.05. \tag{3.23}$$

Here $A^{\mathrm{mle}}_{\mathrm{obs}}$ is the observed maximum likelihood amplitude calculated from the data using $\mathscr{L}_A$. $P(A^{\mathrm{mle}}|A)(f)$ is the probability of calculating A^{mle} given a true signal amplitude A plus background noise. Therefore $P(A_{\mathrm{mle}} \le A^{\mathrm{mle}}_{\mathrm{obs}} | A)(f)$ represents the probability that, given a true signal of amplitude A, A^{mle} would be less than or equal to the value observed. This probability is a monotonically decreasing function of A, and so it is less than 0.05 for all A-values above the

upper limit. In other words, signal amplitudes that would generate an A^{mle} as low or lower less than 5% of the time are excluded from the confidence interval. The limits calculated by this procedure are shown in Figure 3.4. The median upper bound is $0.65°$. The bound varies over frequencies as expected, in analogy to the typical behavior of a Fourier transform.

The probability distribution $P(A^{\mathrm{mle}}|A)(f)$ is generated by calculating A^{mle} from 500 simulated angle timestreams of background noise with an injected signal of amplitude A, frequency f, and random phase between 0 and 2π. This is done for all frequencies and discretized array of A-values, which are smoothed to create a continuous probability distribution. The results are checked for convergence of the median upper limit to the $<1\%$ level. $P(A^{\mathrm{mle}}|A)(f)$ is almost the same for each frequency. The primary difference comes from the finite duration of each observation, which reduces the strength of the bounds at higher frequencies according to the sinc function in (3.15). We can approximate the impact of this by calculating $\mathrm{sinc}(\pi f \overline{\Delta t})$, where $\overline{\Delta t} = 6.4$ hours is the weighted mean observation duration. The maximum amplitude reduction occurs at the largest frequency and is $<2.5\%$. While this effect is included in the constraint we place, it is small enough that we still report the median bound over the full frequency range.

3.7.3 Constraints

The median angle bound A^{95} represents a search for a sinusoidal signal in the CMB data independent of any axion model. Translating this into a constraint on the axion-photon coupling constant $g_{\phi\gamma}$ requires specifying model parameters. In F19, BK22, and SPT22, this was done by simply requiring that the local axion energy density equal the average Milky Way dark matter energy density, which we will call the 'deterministic' case, following reference [53]. This means the axion field has amplitude ϕ_{DM}, where $\phi_{\mathrm{DM}}^2 m_\phi^2/2 = \rho_0$ and ρ_0 is the local density of dark
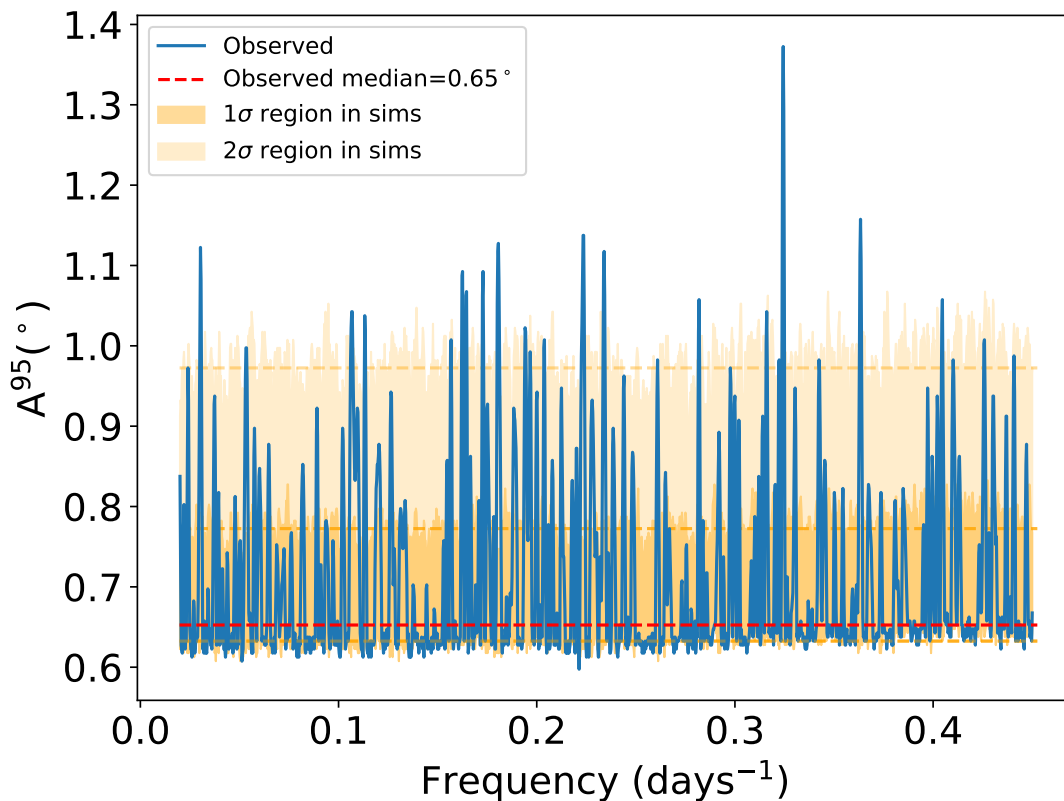
Figure 3.4. A 95% upper confidence limit on the presence of a sinusoidal signal at each frequency. The 1σ and 2σ regions contain approximately 68% and 95% of the upper bounds calculated from 500 simulations at each frequency. The median values for these regions are indicated with dashed lines. Many individual frequencies exceed the 2σ threshold, which is to be expected based on the large number of test frequencies, and does not necessarily indicate a detection.

matter. This gives the relation

$$g_{\phi\gamma} = (1.6 \times 10^{-11}\,\text{GeV}^{-1})$$

$$\times \left(\frac{A}{1°}\right) \times \left(\frac{m_\phi}{10^{-21}\,\text{eV}}\right) \times \left(\frac{\kappa \times \rho_0}{0.3\,\text{GeV/cm}^3}\right)^{-1/2}. \tag{3.24}$$

Here A is the rotation amplitude, m_ϕ is the axion mass, and κ is the fraction of the dark matter that the axion constitutes. Using $\kappa = 1$, $\rho_0 = 0.3\,\text{GeV/cm}^3$, and $A^{95} = 0.65°$, this constraint is

$$g_{\phi\gamma} < (1.1 \times 10^{-11}\,\text{GeV}^{-1}) \times \left(\frac{m_\phi}{10^{-21}\text{eV}}\right). \tag{3.25}$$

Reference [53], however, has recently pointed out that this constraint is inappropriate when the timescale of the experiment is much less than the axion field coherence time, as it is in our case. When considering the local axion field as the sum of many individual wave modes, each with random phase, the amplitude ϕ_0 at any given time is a Rayleigh-distributed stochastic variable centered on ϕ_{DM} that varies with time on the coherence timescale $\tau_{\text{coherence}} \sim (f v_{\text{MW}}^2/c^2)^{-1}$, where the virial velocity is $v_{\text{MW}} \approx 10^{-3}c$. We will call this the 'stochastic' case. This random phase model has been shown to roughly agree with simulations of fuzzy dark matter [114]. The largest frequency we consider in our analysis is $f_{\text{max}} = 0.45\,\text{days}^{-1}$, yielding a minimum coherence time of about 6000 years: therefore, for the purposes of our experiment we can approximate ϕ_0 as a fixed random variable. The phase is treated in the same manner with a uniform probability distribution. To form the likelihood for $g_{\phi\gamma}$ we integrate over these two parameters:

$$\mathscr{L}_{g_{\phi\gamma}}(g_{\phi\gamma}, f) = \int_0^\infty d\phi_0 \int_0^{2\pi} d\theta\, \mathscr{L}(g_{\phi\gamma}\phi_0/2, f, \theta) P(\phi_0) P(\theta). \tag{3.26}$$

Here $P(\phi_0)$ is a Rayleigh distribution centered on ϕ_{DM}:

$$P(\phi_0) = \frac{2\phi_0}{\phi_{DM}^2} e^{-\frac{\phi_0^2}{\phi_{DM}^2}}. \tag{3.27}$$

The resulting median 95% upper limit in this stochastic case is calculated in the same manner as Section 3.7.2, and is

$$g_{\phi\gamma} < (2.4 \times 10^{-11}\,\mathrm{GeV}^{-1}) \times \left(\frac{m_\phi}{10^{-21}\,\mathrm{eV}}\right). \tag{3.28}$$

This is $2.2\times$ larger than the deterministic case.[1] The increase is due to the possibility that we happen to be observing at an unlucky time when $\phi_0 < \phi_{DM}$, which generates a smaller signal amplitude at a given $g_{\phi\gamma}$.

We briefly comment on the choice between frequentist and Bayesian statistics in this analysis. In the frequentist approach adopted here, we generate confidence intervals according to (3.23). In a Bayesian approach, we would instead generate a posterior probability distribution for $g_{\phi\gamma}$, which requires choosing a prior $P(g_{\phi\gamma})$.

In the deterministic case, or equivalently when placing limits on the sinusoid amplitude A, the results roughly agree for several choices of prior. With a uniform prior on A, the median Bayesian upper limit is $0.60°$. If we had instead chosen to parameterize the signal ((3.3)) as

$$\beta_{CMB}(t) = B\sin(2\pi ft) + C\cos(2\pi ft), \tag{3.29}$$

applying uniform priors on B and C give a median upper limit of $0.71°$. Both of these results are close to the median frequentist $0.65°$ upper limit we report in Section 3.7.2.

In the stochastic case there is a large dependence on the choice of prior and parameteri-

---

[1]Reference [22] reports an increase of $2.7\times$ when using the frequentist approach. The difference possibly stems from the use of a different likelihood (they assume that the data is uniformly spaced in time) and/or differences between individual realizations of the noise. When comparing the Bayesian deterministic approach and the Bayesian stochastic approach with a uniform amplitude prior we see a $10\times$ increase, in agreement with [22].

zation. We must integrate over $P(\phi_0)$, and the non-zero probability of small $\phi_0 < \phi_{DM}$ values means that the posterior for $g_{\phi\gamma}$ has a long tail at large $g_{\phi\gamma}$. A uniform prior on $g_{\phi\gamma}$ results in a Bayesian upper limit $10\times$ greater than the deterministic case, much larger than the frequentist result. Futhermore, applying uniform priors in the sine-cosine parameterization ((3.29)) causes the upper bound to diverge. To resolve these issues, reference [53] advocates choosing a Berger-Bernardo prior for $g_{\phi\gamma}$, which like the Jeffreys's prior is parameterization-invariant, and in their analysis agrees with the frequentist result to within 3%. Unfortunately, for our likelihood we found no simple analytic form for this prior and it is difficult to accurately compute numerically. Due to issues with defining a Bayesian prior in the stochastic case, we choose to report a frequentist limit.

This limit is shown in Figure 3.5, along with a selection of other constraints. Our primary result is the constraint on $g_{\phi\gamma}$ assuming that the axion field amplitude is a Rayleigh-distributed stochastic variable. It is shown in full detail along with the median limit from (3.28). The median deterministic constraint, (3.25), is also shown. The published results from BK22 and SPT22 are deterministic Bayesian upper bounds with a uniform prior on $P(g_{\phi\gamma})$. None of the other bounds shown in Figure 3.5 come from assuming a value for the axion field in a dark matter halo. We emphasize that this is the first CMB analysis of this effect that we are aware of to include the local stochastic nature of ϕ_0.

In both the stochastic and deterministic cases, the bounds apply over the frequency range presented in (3.16), which corresponds to the axion mass range

$$9.6 \times 10^{-22}\,\mathrm{eV} \leq m_\phi \leq 2.2 \times 10^{-20}\,\mathrm{eV}. \tag{3.30}$$

3.8 Conclusion

We have used POLARBEAR data to search for a coherent, all-sky, sinusoidal oscillation of the CMB polarization angle in time. We do not detect such a signal, and place a median 95%
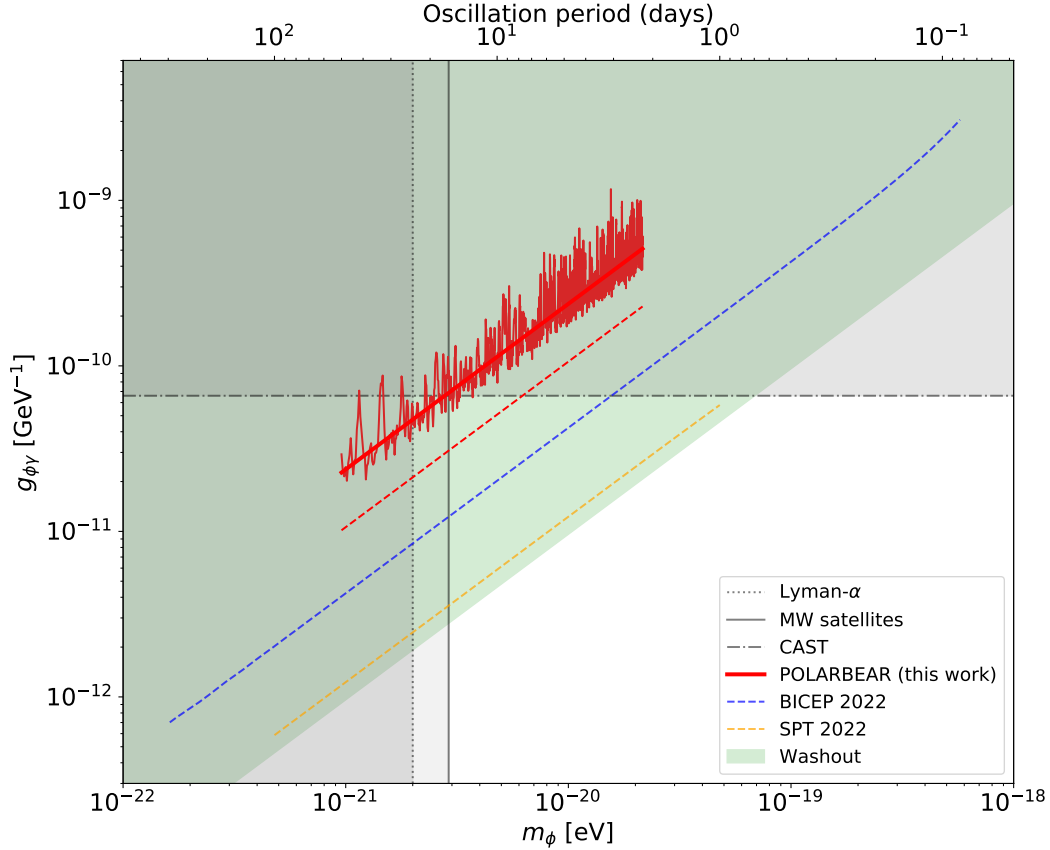
Figure 3.5. Bounds on the axion-photon coupling as a function of axion mass. Shown in solid red is the 95% upper limit obtained in this work using a stochastic local axion field amplitude and assuming the axion constitutes all the dark matter (see Section 3.7). The lighter oscillating result is the exact bound, and the median result, $g_{\phi\gamma} < (2.4 \times 10^{-11}\,\mathrm{GeV}^{-1}) \times (m_{\phi}/10^{-21}\,\mathrm{eV})$, is shown in darker red. The median deterministic bounds for POLARBEAR, BICEP, and SPT are the dashed lines: these are the published results in [13] and [75]. The green 'washout' bound was calculated in F19 from the lack of CMB polarization suppression. Lower bounds on the axion mass come from Milky Way satellites [140] and the Lyman-α forest [116]. Upper bounds on the axion-photon coupling from CAST [51] are also shown.

60

upper limit of $0.65°$ on the sinusoid amplitude over oscillation frequencies between $0.02\,\mathrm{days}^{-1}$ and $0.45\,\mathrm{days}^{-1}$. We use these results to constrain the coupling between electromagnetism and an axion, here defined as an ultralight pseudoscalar field, under the assumption that the axion constitutes all of the dark matter. The signal depends on the value of the axion field at the telescope, and under the assumption that the field amplitude is a Rayleigh-distributed stochastic variable, we set the limit $g_{\phi\gamma} < (2.4 \times 10^{-11}\,\mathrm{GeV}^{-1}) \times (m_\phi/10^{-21}\,\mathrm{eV})$ over the mass range $9.6 \times 10^{-22}\,\mathrm{eV} \le m_\phi \le 2.2 \times 10^{-20}\,\mathrm{eV}$.

Three additional seasons of POLARBEAR data have been collected in addition to the two seasons analyzed here, and we anticipate that analyzing them will improve our data volume by a factor of $\approx$2–3, with a corresponding $\approx$60% improvement in the constraints. This data will also possibly allow us to probe lower frequencies (smaller axion masses), because these seasons are not affected by the HWP position uncertainty that restricted the frequency range in this analysis. A promising avenue for placing constraints several times better than this with POLARBEAR data lies with measurements of Tau A, which was used as a polarization calibration source, and was precisely measured during the five observing seasons between 2012 and 2016. These measurements present a different challenge than the CMB because the axion field at the source needs to be carefully considered, whereas in our analysis the $\mathcal{O}(10^5)$ year duration of recombination allowed for ignoring the source term. Nonetheless, this additional data provides another avenue to search for the presence of axions using POLARBEAR data.

Several future CMB experiments, including the Simons Array [183], Simons Observatory [16], and CMB-S4 [5], should be able to perform a similar analysis with improved constraints. This analysis imposes no additional requirements on the design or operation of these experiments, it simply requires making many measurements of the CMB over an extended period of time. The sensitivity is not fundamentally limited by anything other than the precision of the polarization measurements, unlike the CMB washout effect, which is limited by cosmic variance [74]. The unknown amplitude of the axion field at the telescope is the chief source of model-dependence, but it is well described by a probability distribution that can be treated statistically when placing

bounds. Unlike many other astrophysical measurements, this analysis does not suffer from significant modelling uncertainty at the polarization source due to the well-understood nature of the CMB. In the rapidly growing field of axion searches, this should allow future CMB experiments to provide increasingly competitive measurements of the axion-photon coupling constant.

3.9 Acknowledgments

Chapter 3, in full, is a reprint of the material as it appears in Shunsuke Adachi, Tylor Adkins, Kam Arnold, Carlo Baccigalupi, Darcy Barron, Kolen Cheung, Yuji Chinone, Kevin T. Crowley, Josquin Errard, Giulio Fabbian, Chang Feng, Raphael Flauger, Takuro Fujino, Daniel Green, Masaya Hasegawa, Masashi Hazumi, Daisuke Kaneko, Nobuhiko Katayama, Brian Keating, Akito Kusaka, Adrian T. Lee, Yuto Minami, Haruki Nishino, Christian L. Reichardt, Praween Siritanasak, Jacob Spisak, Osamu Tajima, Satoru Takakura, Sayuri Takatori, Grant Paul Teply, and Kyohei Yamada. Constraints on axionlike polarization oscillations in the cosmic microwave background with polarbear, August 2023. I was the primary investigator and author of this paper.

Chapter 4

The Simons Observatory Small Aperture Telescopes

4.1   The Simons Observatory Overview

The Simons Observatory (SO) is an international collaboration of about 300 scientists building ground-based telescopes to measure the CMB. The nominal configuration consists of one 6m Large Aperture Telescope (LAT) and four 0.5m Small Aperture Telescopes (SATs), while planned expansions SO:Japan and SO:UK will add one and two additional SATs, respectively, by 2026. The observatory is located at the Atacama Desert in Chile's Parque Astronomico at an elevation of 5200m, next to other CMB experiments: Atacama Cosmology Telescope, Cosmology Large Angular Scale Surveyor, and Simons Array (see Figure 4.1). This site offers optimal observing conditions due to the low concentration of precipitable water vapor, which emits and absorbs in the microwave, and access to a large portion of the sky that overlaps with complementary experiments. The LAT will conduct an survey across approximately 40% of the sky, and the SATs will cover a survey area of approximately 10% [186].

The SO telescopes field a combined total of more than 60,000 detectors across six frequency bands centered at 27, 39, 93, 145, 225 and 280 GHz [84]. The LAT and SATs both use superconducting Transition-Edge-Sensor (TES) detectors operating on a focal plane cooled to 100mK to measure the faint CMB anisotropies. The deployment of such a large number of detectors is facilitated by a microwave multiplexing system that allows for 1000 detectors to

be read out on a single pair of coaxial cables. The detectors are embedded in dichroic pixels which each provide measurements of both orthogonal linear polarizations for two frequency bands simultaneously. The wide frequency coverage is designed to allow for the characterization and removal of two polarized foreground contaminants: galactic synchrotron emission, which is dominant at lower frequencies, and galactic dust, dominant at higher frequencies.

SO will provide the leading ground-based measurements of the primordial CMB perturbations as well as secondary anisotropies. The LAT will provide a set of high resolution maps of the temperature and polarization anisotropies, which will enable it to measure the gravitational lensing of the CMB, detect the thermal and kinetic Sunyaev– Zel'dovich effects, and constrain cosmological parameters. Key science goals include measuring the sum of neutrino masses, the effective number of relativistic species in the early universe, and dark energy, as well as improving our understanding of galaxy evolution and providing a catalog of galactic and extragalactic sources [186].

The SATs, which will be the focus of this chapter of the thesis, have a single primary science goal: measuring the polarization signature generated by primordial gravitational waves from inflation. The search for this signal is parameterized in terms of the tensor-to-scalar ratio r, and the current best upper bound is $r_{0.05} < 0.036$ at 95% confidence level [15]. The SATs have a target precision of $\sigma(r) = 0.003$. Both the SATs and the LAT will also enable a host of secondary science goals, including improved searches for signatures of cosmic birefringence.

The Simons Observatory has recently achieved first light, and currently all three SATs and the LAT have been deployed to Chile. The first SAT, which contains MF optics and is called SAT-MF1, was built at UCSD. SAT-MF1 served as the pathfinder SAT cryostat and underwent several years of technological integration, cryogenic validation, and optical validation. The remainder of this chapter will primarily dedicated to my contributions to the commissioning of SAT-MF1, which extended up to cryogenic validation of the instrument. Section 4.2 provides an overview of SAT MF-1 in its entirety, and the following subsections describe the integration and testing of selected components of the telescope. The final section, Section 4.8, describes

Figure 4.1. An overhead view of the SO site captured by drone [144, 58]. In the foreground are the LAT and the three SATs inside their ground shields. Directly behind is the ground shield for the Atacama Cosmology Telescope, and to the right are the Cosmology Large Angular Scale Surveyor (near) and Simons Array (far). Image provided by Gabriele Coppi, Rolando Dunner, Federico Nati, and Matias Rojas.

the design and construction of the SAT ground shields, which mitigate the effects of thermal emission from the ground.

4.2 SAT Overview

The search for primordial B-modes necessitates an experiment with high sensitivity and unprecedented control of instrument systematics. The SAT is optimized to cover the large angular scales ($30 \leq l \leq 200$) containing the predicted peak of the primordial B-mode signal with high sensitivity by using a 42 cm diameter aperture stop coupled to a nearly 40 cm diameter focal plane. The planned survey area for the SATs covers a sky fraction of 10% designed to maximize the instruments' mapping efficiency and consists of two sky patches that avoid emission from the Galactic plane. The field of view (FOV) of each telescope is $35°$.

Each SAT in the array is composed of two primary components. The SAT platform (SATP) provides the mounting and pointing structure for the receiver as well as optical baffling components. The SAT receivers couple light to dichroic detectors with the receivers denoted by one of three frequency band pairings. The frequency pairings are 27/39 GHz, 93/145 GHz, and 225/280 GHz for the SAT-LF ('low-frequency'), SAT-MF ('mid-frequency'), and SAT-UHF ('ultra-high frequency'), respectively. The sensitivity requirements of the experiment necessitate more observing weight on the primary CMB bands so two 'mid-frequency' receivers will be deployed as the first light instruments, denoted SAT-MF1 and SAT-MF2. The SAT-UHF telescope is designed primarily to remove the Galactic dust emission. The SAT-LF telescope is designed to remove Galactic synchrotron emission and is the final element in the SO nominal array, with a completion date after the initial array of three is on-sky as less observing weight is needed from the LF channels.

State-of-the-art millimeter TES detector arrays are photon noise-limited. Thus, increasing detector counts is one of the most straightforward ways to increase experimental sensitivity within a finite observing period [104]. The SATs use dichroic pixels sensitive to both linear
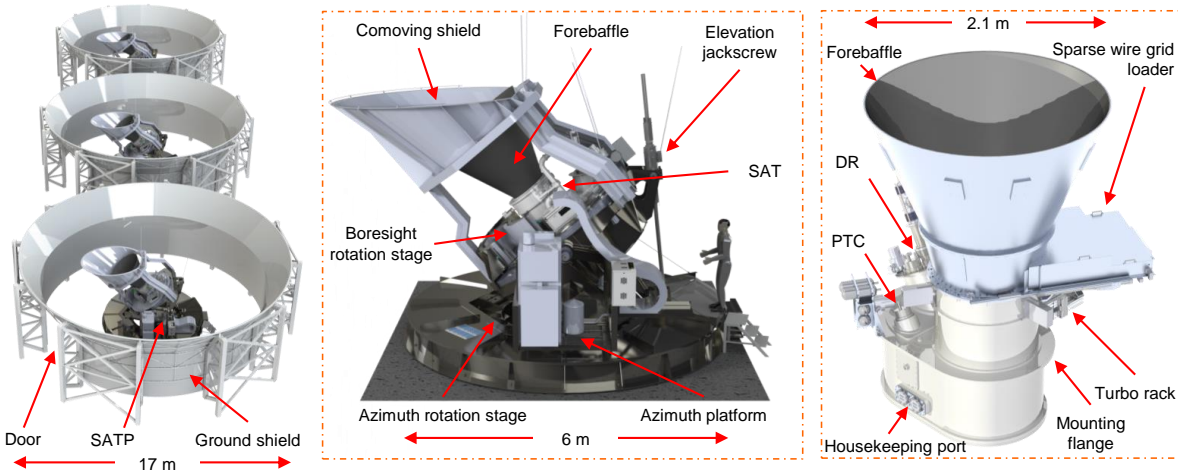
Figure 4.2. *Left*: A schematic of the array of three SATs as they would appear in Chile. Each SAT receiver is mounted to a SATP and surrounded by a ground shield. *Center*: Detailed view of the SATP with the receiver mounted as reference. *Right*: Detailed view of the SAT receiver with the forebaffle and sparse wire grid loading mechanism.

polarization directions, each containing four TES detectors [181]. The detectors are packaged into seven hexagonal units per SAT focal plane, referred to as universal focal-plane modules (UFMs). Each UFM for SAT-MF1 contains 1,728 detectors [134, 133], giving a total of 12,096 detectors in SAT-MF1.

A microwave multiplexing system (μMUX) using SLAC microresonator radio frequency (SMuRF) electronics reads out the detector signals [67, 99, 199]. SMuRF is capable of reading out over 1000 detectors via a single coax cable pair, resulting in only two coax pairs per UFM. This greatly simplifies the cryogenic cable management for reading out large format detector arrays. The coax lines are complimented by a woven cable for each UFM that provides the TES bias voltages, the flux ramps for the multiplexing circuit, and the power for the cryogenic low-noise amplifiers (LNAs). The SMuRF electronics systems are contained in several liquid-cooled NEMA 4X standard enclosures that are co-mounted with the receiver on the boresight stage. Optical fibers are used to transfer data to the site computing system.

Three 45 cm diameter silicon lenses with metamaterial anti-reflective coating (ARC) [93, 59, 63] couple the arrays to the sky with diffraction-limited resolution across the focal

plane. The aperture stop, all three lenses, and two of the low-pass-edge (LPE) filter elements are combined into a single unit referred to as the optics tube (OT). To maximize the SAT mapping speed, the entire OT is cooled to $< 1\,\mathrm{K}$— the first ground-based CMB telescope to do so. The OT assembly comprises $0.26\,\mathrm{m}^3$ in volume and over $200\,\mathrm{kg}$ in mass. The development of key technologies and capabilities with the SO SATs will be a valuable reference for future experiments planning to operate with large optical volumes at or below $1\,\mathrm{K}$, such as CMB-S4 [9, 6].

The SATPs were assembled by Vertex Antennentechnik GmbH[1] in Germany. Each SATP has an azimuthal rotation stage capable of covering up to $540°$ of rotational freedom and includes an integrated platform for mounting cryogenic equipment and electronics. The elevation stage provides pointing over a range from $20°$ to $90°$ above the horizon and is driven by a jackscrew mounted at its rear. The elevation can point to $0°$, after the removal of part of the optical baffling, for servicing and mounting components. Additionally, each SATP has a boresight pointing stage which allows $\pm 90°$ rotation around the receiver optical axis for additional polarization systematic controls (Figure 4.2).

Stray light and ground illumination are significant systematics concerns for the SAT. The SAT is designed such that radiation from the ground will be diffracted twice before entering the optics at our nominal pointing elevations. This design incorporates a forebaffle mounted to the front of each receiver, a comoving shield attached to the elevation structure of the SATP, and a groundshield that encircles the entire SATP. The forebaffle is conical with a weatherproofed microwave black coating on the interior surface, an aperture diameter of 2.1 m, and a height of 1.7 m from the window surface with the criterion that geometric rays with $> 40°$ incidence angle relative to the boresight cannot directly illuminate the receiver window. Additionally, the base of the forebaffle integrates an automated sparse wire grid mechanism that can be inserted in front of the window and rotated to allow for polarization angle calibration during routine observing operations [139]. The comoving shield is a conical section with a reflective aluminum surface

---

[1]Vertex Antennentechnik GmbH, 47198 Duisburg, Germany
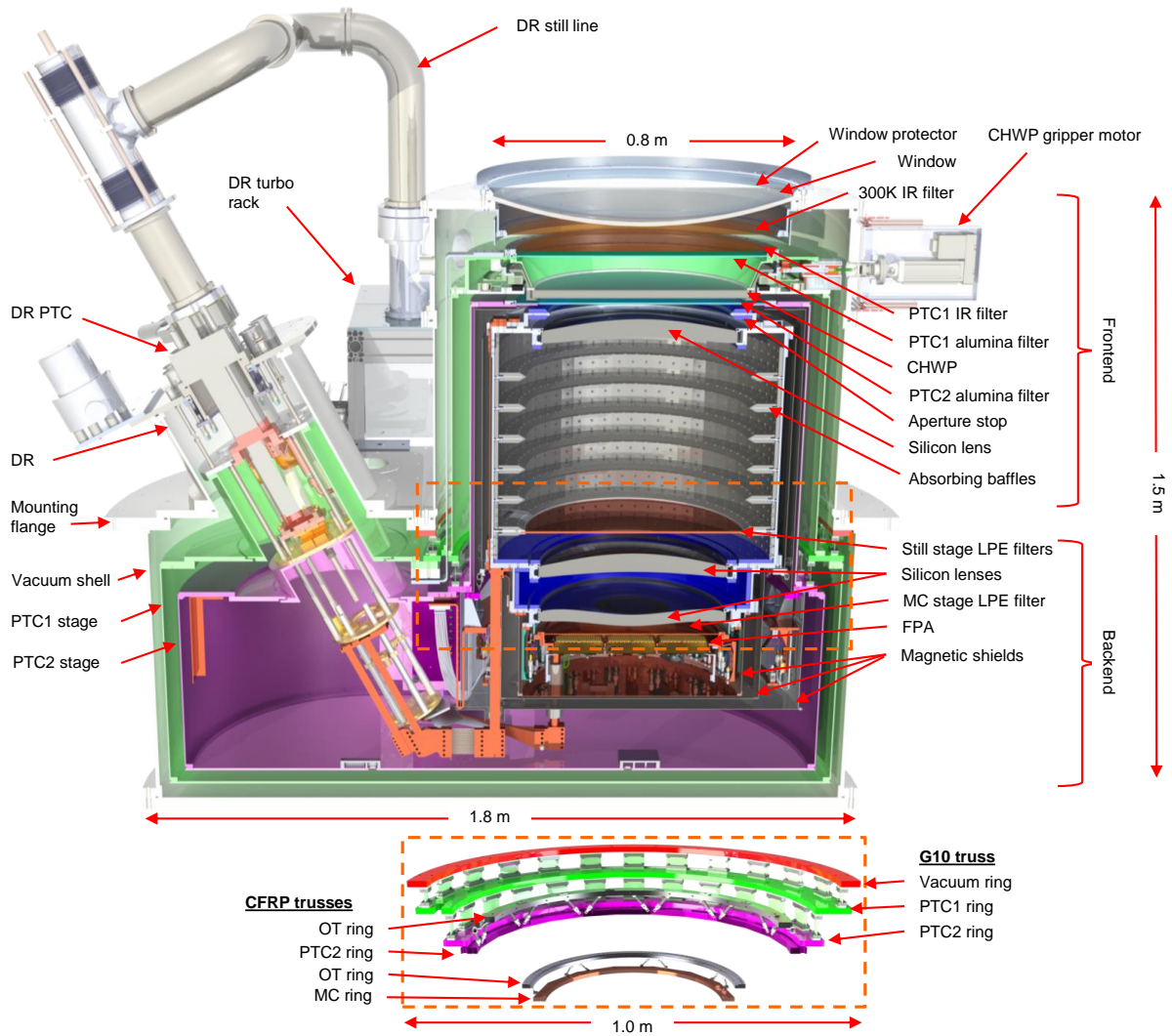
Figure 4.3. A cross-section view of SAT-MF1 showing the principal components. *Inset*: A detailed view of the three primary mechanical trusses as they are situated in the overall assembly with all surrounding components hidden.

that is 2.3 m tall with the tip extending 3.7 m from the window surface. The groundshield is built on a separate foundation surrounding the SATP with the upper edge at a radius of 8.4 m and height of 5.66 m and is formed from cylindrical and conical fiberglass panels. The interior of the cylindrical wall section is covered in steel panels to create a uniform surface facing the SATP. The upper 2 m of the ground shield forms an aluminum cone angled at 30° from vertical to reflect radiation skyward. At the top of the shield is a 5 cm radius aluminum pipe composed of eighteen sections and smoothly curved to provide minimal variation in ground pickup while the telescope is scanning. The combination of the three shields provides an optimal solution to balance the SAT sensitivity and systematics requirements with project costs and the features of the Chilean site (Figure 4.2).

Polarization modulation has become a prominent technique to enable polarization measurements over large angular scales by effectively decoupling the polarization signal from non-modulated signals such as atmospheric effects [97, 176, 103, 161]. The SATs use a cryogenic rotating half-wave plate (CHWP) operating at 50 K with a superconducting magnetic bearing. The nominal spin speed of the CHWP is 2 Hz, which modulates the CMB polarized signal at 8 Hz. The SAT-MF1 CHWP is composed of a three layer sapphire stack sandwiched between two alumina plates each with a two layer mullite/duroid ARC. More details of the design and performance of the CHWP used in SAT-MF1 can be found in [198].

4.3   Cryogenic Structure and Trusses

The scientific goals of the SAT require cooling the detectors, optics, and CHWP system to cryogenic temperatures, which provides tight constraints on the overall design of the SAT-MF1 receiver. The structure of SAT-MF1 incorporates an outer vacuum shell with two nested thermal shells cooled by two Cryomech[2] PT-420 pulse tube coolers (PTCs), one of which is integrated into the dilution refrigerator assembly (DR). We will refer to the first thermal shell as the PTC1 stage and the second thermal shell as the PTC2 stage. A modified SD-400 DR manufactured

by Bluefors[3] provides the cooling power for the 1 K still stage, which is coupled to the OT, and the 100 mK mixing chamber (MC) stage, which is coupled to the focal plane assembly (FPA). The FPA houses the seven UFMs and their associated cold readout components. The principal elements of SAT-MF1 are shown in Figure 4.3 and an image of the fully assembled receiver in lab is shown in Figure 4.4.

4.3.1 Truss Design

The SAT receiver's internal support structure consists of three distinct trusses that provide mechanical support while thermally isolating temperature stages. Each truss mounts near the center of mass of the components it supports in order to simplify the assembly and minimize any deflection at non-vertical pointings. The design strategy allows for a single mating surface at each stage to meet our mechanical requirements. By creating the mounting interface near the center of mass of the components, the receiver is naturally split into two primary volumes. The front-end volume is cylindrical and encompasses the majority of the optical components. The back-end volume is oval in shape with flat sides to accommodate access ports and electronics feed-throughs and encompasses the cryogenic components, focal plane, and cold electronics components. Details of the design can be seen in Figure 4.3.

The vacuum shell was designed to hold sea-level atmospheric pressure with a minimum FoS of four. The overall mass was not a strong driver of the design. The back-end is closed off with one large lid which allows ample access space to the back-end cryogenics, focal plane, and electronics. This greatly simplifies the integration of components and allows for quick turn-arounds between cool-downs. A prominent flange at the top edge of the back-end vacuum shell provides the mating surface to the SATP.

The first support truss (the G10 vacuum/PTC1/PTC2 truss) attaches to the same plate that mates to the SATP. The truss is composed of three rings corresponding to the vacuum shell, PTC1 stage, and PTC2 stage with the thermal offset between stages provided by G10 tabs that

---

[3]Bluefors Oy, 00370 Helsinki, Finland

Figure 4.4. The fully assembled SAT-MF1 in the UCSD laboratory space. The rack mounted to the side houses the turbo-molecular pumps for the DR circuit and is attached to the receiver with a mounting jig for testing in the lab.

bolt to the rings.

The second truss is composed of carbon-fiber-reinforced polymer (CFRP) struts running between two aluminum rings at $\sim 45°$ and provides the mechanical support for the still stage, with one end bolted to the PTC2 ring of the G10 vacuum/PTC1/PTC2 truss and the other end bolted to a flange near the center-of-mass of the OT (referred to as the CFRP PTC2/OT truss). The struts providing the mechanical support and thermal isolation between the rings are comprised of CFRP tubes with aluminum caps epoxied on each end of the tubes which are then bolted to the aluminum rings. The CFRP tubes are manufactured by Clearwater Composites[4]. The CFRP PTC2/OT truss is re-entrant with respect to the G10 vacuum/PTC1/PTC2 truss to keep the mounting points as close to the center-of-mass of the system as possible.

A third, smaller CFRP truss (the CFRP OT/FPA truss) of similar design connects the focal plane on the MC stage to the bottom surface of the OT. The CFRP tubes for this truss are manufactured by vDijk Pultrusion Products[5] (DPP). More details of the design, manufacture, and testing of the CFRP struts is described in [60].

A sheet of $6.25 \mu m$ thick mylar with a > 150 angstrom aluminum layer on both sides, procured from MEI[6], bridges each thermal gap on all the support trusses to create an enclosed Faraday cage encompassing the back-end. The back-end vacuum shell provides the primary element of the RF shield with specialized RF gaskets installed on the outside of each vacuum O-ring to ensure the shielding is maintained at vacuum joints. Pi filters are attached at the hermetic sockets for the housekeeping and non-coax readout inputs. The alumnized mylar then carries the shield down to the focal plane where the FPA itself completes the shield in order to isolate electronic components in the back-end volume from RF-interference.

The design also incorporates two additional CFRP trusses for the cold readout electronics from the PTC2 to OT stages and from the OT to FPA stages. The mass suspended by these trusses is relatively small and their primary purpose is to provide a modular mechanical structure

---

[4]Clearwater Composites, LLC., 4429 Venture Avenue, Duluth, MN 55811, USA
[5]vDijk Pultrusion Products, Aphroditestraat 24, NL-5047 TW TILBURG, The Netherlands
[6]MEI - Metallized Engineering, Suffield, CT 06078
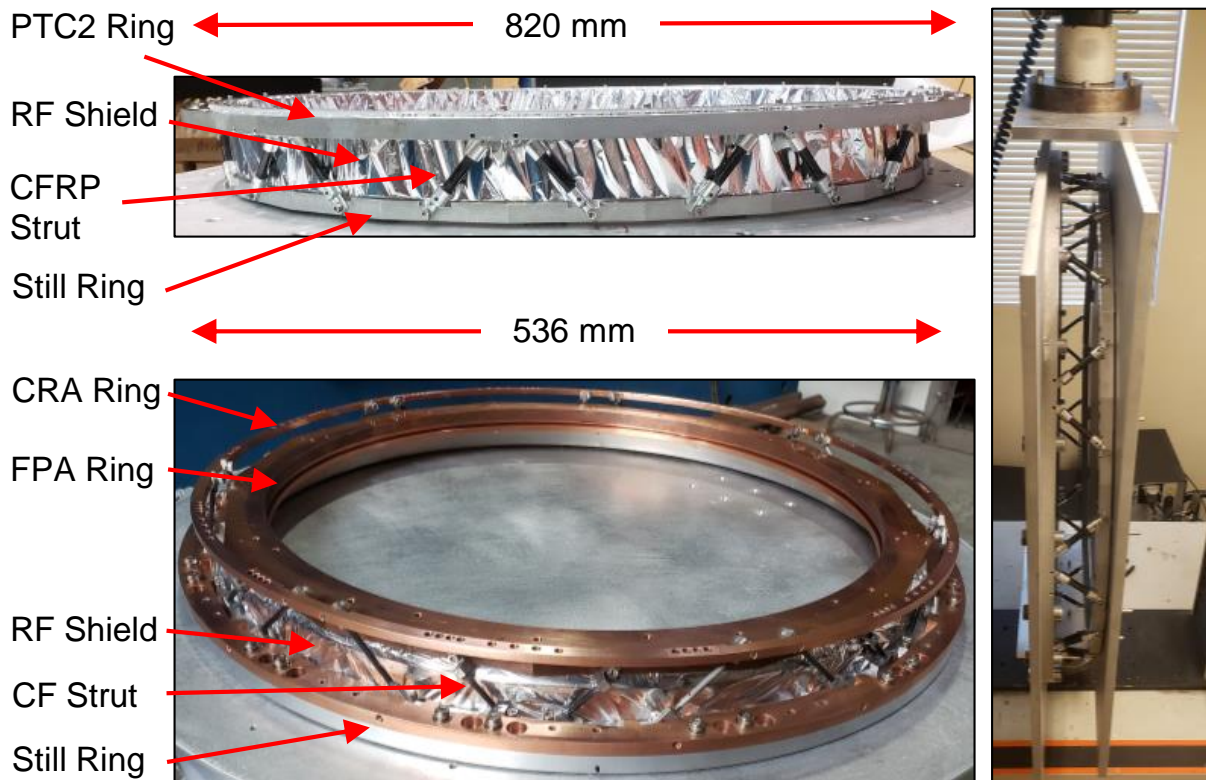
Figure 4.5. *Top Left*: The CFRP PTC2/OT truss with the RF shield installed. *Bottom Left*: The CFRP OT/FPA truss with the RF shield installed. The carbon fiber supports and copper ring for the CRA components at the MC stage is also integrated into the pictured assembly. *Right*: Example validation test showing the CFRP PTC2/OT truss mounted in the Instron universal testing machine for the shear force test.

for the readout components that is stiff, with primary resonance modes above ~ 40 Hz, and low thermal conductance.

4.3.2 CFRP Truss Strength Tests

The SAT-MF1 trusses had to meet two primary mechanical goals: 1) support the system with enough margin of safety to ensure reliable operation over all observing, transport, and installation procedures, and 2) maintain the alignment of the optical system to within the tolerances specified by the optical design. Validation tests were performed at several stages of the manufacture and installation procedure to verify the mechanical elements of the receiver conformed to our requirements. This section will describe the validation of the CFRP trusses.

The loading requirements for the two CFRP trusses come from the most stringent use cases and the weight of the mass each truss supports. These requirements are shown in Table 4.1. The multiple of 3 on the requirements for the PTC2/OT truss in compression and the OT/FPA truss in tension comes from the site transport condition of the fully loaded SAT-MF1 receiver. The other requirements with a multiple of 1 are set by supporting the mass during normal operation.

Table 4.1. Truss loading requirements. The mass supported by each truss in the fully assembled SAT-MF1 is indicated. 'Tension', 'Compression', and 'Shear' indicate the maximum loading condition from transport or operation along each axis, in multiples of the supported mass.

Truss	Mass	Tension	Compression	Shear
G10 Vac/PTC1	460 kg	3	1	1
G10 PTC1/PTC2	300 kg	3	1	1
CFRP PTC2/OT	210 kg	1	3	1
CFRP OT/FPA	30 kg	3	1	1

We performed simulations under these loading requirements to determine the maximum stress on an individual strut. The results of these simulations across all three loading conditions produced three numbers for each strut: the maximum stress in tension, compression, and shear. The shear force experienced by any single strut is very small due to the design of the trusses, and individual struts were found to exceed these requirements easily. The primary requirement is on the tension and compression resilience of the struts. The epoxy joint between the CFRP and the aluminum end caps experiences similar stresses in tension and compression as the dominant adhesion area is between the walls of the nested cylinders, and so we report only the tension requirements here. The most stringent CFRP requirements for both trusses come from the axial loading in the site transport case, from the assembly highbay to the observing platform, with the multiple of three included in the numbers shown in Table 4.2. The resulting strut design, analysis, and testing is described in detail in [60], and the results described therein led to the struts and trusses presented in this paper. We tested five of each strut type to destruction in an Instron, all of which exceeded our requirements in their elastic regime. Notably, the failure point

was most typically at the aluminum tab where the bolt is mated rather than at the epoxy joint.

Table 4.2. Tab and strut testing results. The elastic strength tension requirement for an individual element was calculated using simulations of the full truss loads shown in Table 4.1. The measured value refers to the minimum top of the elastic regime for all witness sample tabs and struts which were tested to destruction.

Strut Type	Tension Requirement	Measured Yield
Monolithic G10 tab	0.575 kN	> 10.5 kN
3mm OD CFRP	0.3 kN	> 0.8 kN
8mm OD CFRP	1.5 kN	> 2.5 kN

After individual struts were validated and full CFRP trusses assembled, we performed non-destructive tests on each CFRP truss. First, the trusses were thermally cycled in liquid nitrogen five times to simulate stresses that occur during cooldowns. Next, we applied loads to the trusses that were safely in the elastic regime of the struts, based off the strut test data, but beyond the minimum requirements specified in Table 4.2 to ensure the fully assembled trusses were not susceptible to an unanticipated failure mode that would not be found in individual strut tests. This required six tests in total. Four of the six were conducted in an Instron; the CFRP PTC2/OT tension and compression tests were conducted by hanging and stacking weights on the truss, since this truss would not fit in the Instron in those orientations. The tests in the Instron yielded force vs displacement curves, shown in Figure 4.6. The CFRP PTC2/OT truss remained in the elastic regime beyond 3.6 kN in the shear test on the Instron and successfully supported 4.2 kN in tension and 10.0 kN in compression. The CFRP OT/FPA truss remained in the elastic regime beyond 1600 N, 600 N, and 400 N in the tension, compression, and shear directions, respectively. The trusses were inspected for damage after each test and with no notable issues, they were approved for installation in SAT-MF1.

Finally, it is worth noting that there are two additional CFRP trusses that support the detector readout system. These trusses support far less mass and are made with the same 3 mm and 8 mm OD CFRP struts as the other two trusses, with only small differences in dimension, and so were not separately validated.
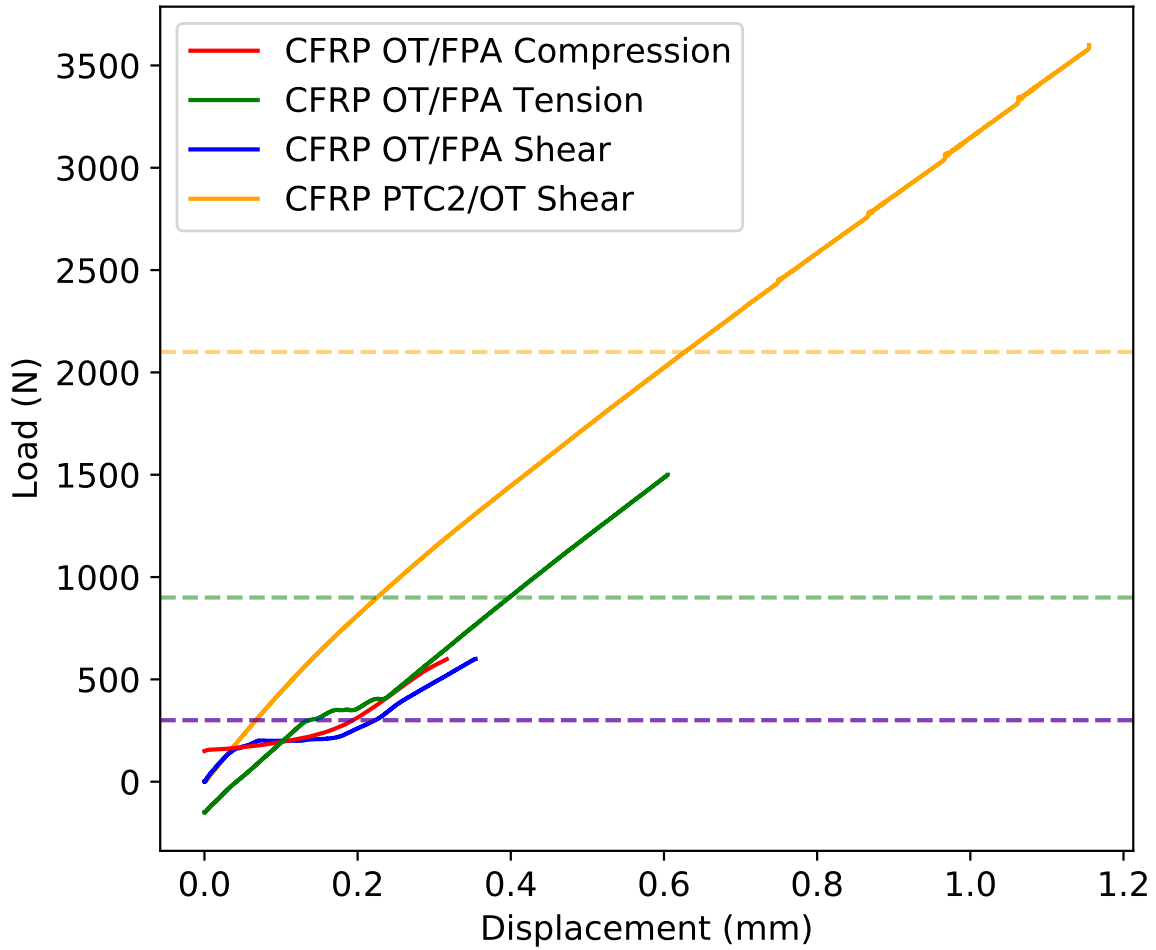
Figure 4.6. Stress tests of the CFRP PTC2/OT truss in shear and the CFRP OT/FPA truss in all three configurations. After some initial settling, all tests show the trusses remain in the elastic regime as predicted, exceeding the loading requirements set in Table 4.1 (horizontal lines). The FPA compression and tension tests start from an offset of +150N and -150N respectively due to the weight of the testing jig.

4.4   Housekeeping Electronics

The SAT receiver requires a suite of diagnostic sensors and heaters to monitor and control the instrument. The most important of these are the cryogenic thermometers, which provide the data necessary for much of the thermal analysis in the following sections. There are sixteen silicon diodes that measure temperatures across the PTC1 and PTC2 stages, and twelve ruthenium oxide (ROX) thermistors that measure temperatures across the still and MC stages. The diodes and still ROXs are read out with four-wire measurements using Lake Shore[7] 240 Series Input Modules (LS240s). The five MC ROXs are read out with four-wire measurements using a dedicated Lake Shore Model 372 AC Resistance Bridge (LS372) with associated model 3716 preamp/scanner. In addition, the DR comes equipped with a temperature sensor on each stage, which are read out with a separate LS372 and preamp/scanner.

The ability to apply heat to different temperature stages is important during both testing and normal telescope operation. The DR comes equipped with heaters at the still and MC stages, which are used to set the stage temperatures and to run load curves. A custom heater is located on the focal plane to control and stabilize the temperature of the detectors (see section 4.5). These heaters are controlled through the two LS372s. Additionally, several other heaters across all temperature stages were used for in-lab testing to understand the thermal conductivity of the system and were controlled via several programmable PSUs.

The thermometry and heater cables enter SAT-MF1 through two Accu-Glass[8] 50D2-L100 hermetic feedthroughs. There are four 50 pin twisted pair looms[9] between the vacuum shell and the PTC2 stage designated for: ROX thermometry, diode thermometry, heaters, and a spare. High-frequency signals are filtered out by 0.8 MHz cutoff frequency Pi filters at the output of the cryostat. The ROX thermometry output is connected to a break-out PCB which routes the MC ROXs to an LS372 scanner and the still ROXs to an LS240. Manganin cables manufactured by

---

[7]Lake Shore Cryotronics, Westerville, OH 43082
[8]Accu-Glass Products Inc., Valencia, CA 91355
[9]Universal Cryogenics, Tucson, AZ 85705

Universal Cryogenics[10] with D-sub 50 connectors on one end and MDM-51 connectors on the other route from the vacuum side of the hermetic connector to the PTC2 stage via thermalizing clamps at both the PTC stages. The cables connect to a set of PCBs heatsunk to the PTC2 stage which break-out each MDM-51 connector into 12 4-pin Glenair[11] connectors. Individual sensors and heaters are then routed from the PCB to their installed location on each stage.

The housekeeping system also monitors and controls a number of other telescope components, including the pulse tube compressors, DR turbo pumps, and gas handling system. The external temperature of the telescope and temperature-sensitive electronics are monitored using approximately twenty thermometers read through a Labjack T7[12]. Essential housekeeping systems are provided power through an uninterruptible power supply to ensure they can be put into a safe standby mode in the event of power interruption at the site.

The housekeeping system and other devices, such as the CHWP, are managed through the Observatory Control System (OCS), a custom open-source platform designed by SO to manage distributed systems[13]. OCS runs across multiple nodes, managing the data acquisition and control for many of the SAT-MF1 subsystems, as well as linking them to live-monitoring tools. A detailed overview of OCS and the SAT-MF1 DAQ network is described in [125].

The majority of the housekeeping electronics system is located on the boresight stage of the SATP, which holds the SAT receiver. Since the boresight plate is not environmentally sealed, the electronics are protected by NEMA 4X standard enclosures. Power and network connections are provided by electronics at the base of the telescope, which connect to site computing and power outside the ground shields. A schematic diagram of the housekeeping components is shown in Figure 4.7.

---

[10]Universal Cryogenics Laboratories, Tucson, AZ 85705
[11]Glenair Inc., Glendale, CA 91201
[12]LabJack Corporation, Lakewood, CO 80235
[13]GitHub: http://github.com/simonsobs/ocs
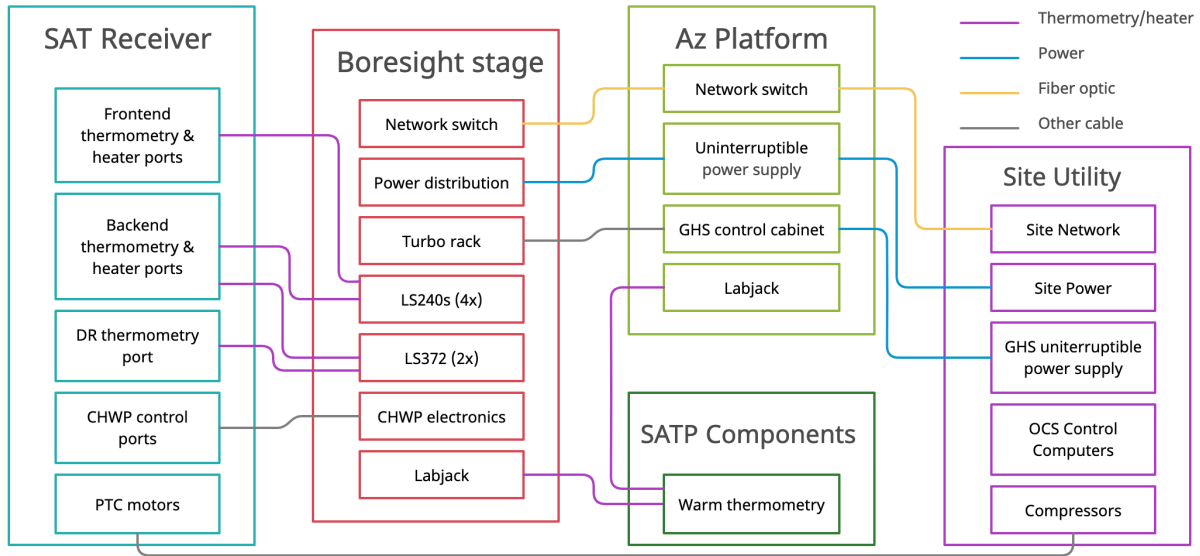
Figure 4.7. Diagram of the SAT housekeeping system and related components. Principal locations of components are identified with different color schemes. Lines denote cable connections between locations. Internal connections, chiefly ethernet and power, are omitted. Also omitted are vendor supplied systems for SATP monitoring such as motors and encoders. More details on the computing structure of the housekeeping system can be found in [125].

4.5 FPA Temperature Stability

Providing a stable thermal environment for the focal plane is important as TES detectors are sensitive to variations in the bath temperature. SAT-MF1 uses a control thermometer combined with a $50\,\Omega$ heater epoxied into a copper mounting block to provide thermal control of the FPA. Superconducting NbTi wires connect the heater to the housekeeping breakout board on the PTC2 stage. We use a Lakeshore 372 temperature bridge and a custom proportional-integral-derivative (PID) loop implemented within an OCS agent to servo the heater and stabilize the FPA temperature. The temperature measured by the control thermometer is a good approximation for the temperature of the entire FPA, as typical gradients across the FPA are ≤ 1 mK.

Through PID control, the SAT is able to control the FPA to a set temperature for an arbitrary length of time with RMS fluctuations of $< 7\,\mu\text{K}$. As shown in Fig. 4.8, PID control provides improved stability on timescales greater than 30 seconds, eliminating long-timescale effects such as diurnal variations. This level of control has proved sufficient for the in-lab testing

described in this paper. Future work will assess whether this setup mitigates thermal fluctuations at a level sufficient for detector noise during observations, in particular their impact on the $1/f$ noise of the demodulated detector timestreams.

4.6 CHWP

4.6.1 CHWP design

The CHWP is part of the optical stack and is located at the PTC1 stage front-end (see Figure 4.3). The CHWP sapphire stack is mounted to a magnetic ring, which at cryogenic temperatures is levitated by 53 yttrium barium copper oxide (YBCO) high-temperature superconducting pucks positioned under the ring. Rotation is provided by a combination of small fixed magnets on the rotating component and solenoid motor coils fixed to the PTC1 stage.

The CHWP system has a number of crucial interfaces which contribute to thermal loading. There are three linear actuated motors that grip the CHWP when the CHWP is mechanically connected to the cryostat, most crucially when the receiver is cooling and warming. The actuators are mounted symmetrically around the CHWP on the vacuum shell and grip the CHWP via three small diameter G10 cylinders, which provide the requisite compression strength while maintaining thermal isolation. The CHWP also has wiring for thermometry, the drive motor solenoids, and the rotation encoder elements. This wiring is routed out of the receiver via two Accu-Glass 15D2-L63 hermetic feedthroughs on the front end of the vacuum shell. The rotation encoder primarily consists of five LEDs and associated photodiodes that provide accurate information about the spin frequency of the CHWP. The CHWP itself imparts some friction on the system through non-idealities in the magnetic field that induce eddy currents, which can also cause heating. The gripping, wiring, and eddy current thermal loading, as well as mechanical constraints imposed by the system, were incorporated into the design for the SAT receivers. A detailed description of the CHWP system can be found in [198].
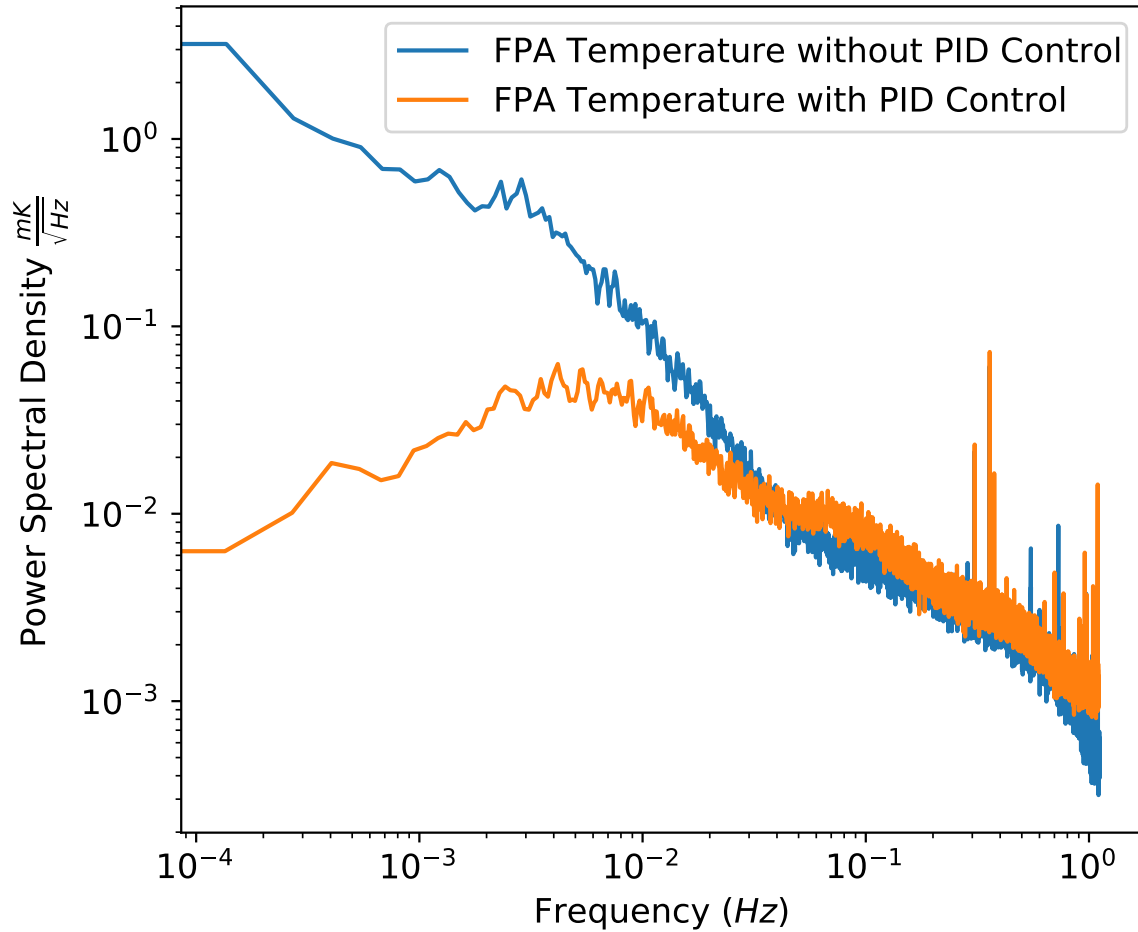
Figure 4.8. Focal plane temperature stability with and without PID control. The 'PID control' data was taken at a temperature of 100mK, and the 'without PID control' data was taken while constant heating power was applied to the focal plane to produce a similar temperature. A single thermometer sampled at 2Hz was used to record the FPA temperature and provide PID feedback. PID control was optimized for lower frequencies and begins to provide improved stability at periods longer than about 30s.

4.6.2 Vibrational heating from the CHWP

During the course of SAT-MF1 testing, we observed a coupling between the temperature of the FPA and certain CHWP spin frequencies. This was caused by the spinning CHWP exciting vibrational modes in the FPA structure, resulting in up to a 5 mK increase in the FPA base temperature. The spin frequencies that excited resonances were identified using an accelerometer attached to the SAT receiver, which showed spikes at 96 times the CHWP spin frequency. This multiplicative factor is associated with two symmetry numbers in the CHWP system: the 16 magnetic segments on the spinning part of the CHWP, and the 48 superconducting YBCO pucks on the static part of the CHWP. The heating is most noticeable when spinning the CHWP from 1 to 2 Hz, which corresponds to focal plane vibrational resonances at 100 to 200 Hz. However, since the CHWP can maintain a fixed spin rate to < 0.01 Hz accuracy, and the focal plane resonances appear narrow, there are wide regions of spin frequency space to operate in without causing noticeable heating. This allows the CHWP to spin at its desired frequency of ~ 2 Hz without issue. We have also changed the number of superconducting YBCO pucks in the system to 53 such that the number of pucks and number of magnet segments are relative primes of each other to eliminate the observed resonances [198].

4.7 Magnetic field testing

4.7.1 Magnetic Shielding

The TES detector and readout architecture used in the SATs is susceptible to interference from fluctuating magnetic fields [189, 112]. During operation these can come from the scanning of the telescope through Earth's magnetic field, the drive motors of SATP, and the CHWP bearing and motor. The SAT receivers incorporate multiple levels and types of shielding to maximize attenuation of external fields at the location of the FPA (see Figure 4.3).

The first shielding layer is composed of Amuneal[14] Amumetal 4 K (A4K) material and

---

[14]Amuneal Mfg. Corp., Philadelphia, PA 19124

comprises a cylinder that attaches to the PTC2 stage and wraps around the OT and FPA volumes with a hole for the optical beam and a lid at the other end to allow FPA access. The second shielding layer is also an A4K cylinder nested inside the first layer and attached to the OT which is thermally coupled to the still stage. A third shield, mounted on the back of the OT, is composed of a cylindrical copper shield around the FPA volume with a 90/10 tin/lead plating on the outer surface to provide a type 2 superconducting shield with a lid at one end of the cylinder to provide access. The lead is included to prevent tin pesting. The impact of penetrations in the A4K magnetic shielding by the 1" diameter copper rods of the heat straps is minimized with small cylindrical protrusions from each of the magnetic shield lids. More details on the SAT receiver's magnetic shielding can be found in [21]. Shielding is also integrated directly into the UFM package, principally in the form of an aluminum shell that composes the outer layer of the UFM package [189, 112].

4.7.2   Solenoid Driven Magnetic Fields

We performed two tests of the magnetic field sensitivity with a field-deployable UFM: once in a test cryostat with no additional magnetic shielding added over the UFM's intrinsic shielding and once in the SAT-MF1 cryostat with all three of the deployment magnetic shields. We compare the UFM magnetic field response measured in both tests to measure the total attenuation of the SAT-MF1 magnetic shielding. We also use these tests to estimate the magnetic field seen by the UFM's from the Earth's magnetic field during observations.

The sensitivity of the UFMs to external magnetic fields was tested using a coil of audio cabling wrapped 100 times around a $1\,\mathrm{m} \times 1\,\mathrm{m}$ box that was positioned below and to the side of SAT-MF1. This setup does not provide a uniform magnetic field as a Helmholtz coil would, but the field was measured with a Honeywell HMR2300 smart digital magnetometer[15] to be uniform to $< 10\%$ within the region spanned by the detectors. A sine wave current with a period of 100 s was sent through the cabling, which was slow enough to act as an approximately DC

---

[15]Honeywell Aerospace, Phoenix, AZ 85034

field while providing an unambiguous magnetic response in the detectors. The magnetic field at the location of the detector arrays relative to the solenoid was measured using the magnetometer, and a maximum field of 0.8 Gauss was applied.

The response of the UFM to the injected magnetic field was determined by measuring the amplitude of the sine-wave in the detectors' time-ordered data. We first subtracted a linear fit and then applied a Buttersworth filter centered on the injected magnetic field frequency. Finally, we fit a sine wave to the resulting data using a least squares regression to extract the amplitude. The resulting data product is the response of the UFM to external magnetic fields with units of pA/G of external magnetic field. We were able to complete the analysis with the test cryostat data, however, no response was seen when the full shielding was present in the SAT-MF1 test so the detector noise level forms an upper bound on the magnetic pickup.

Figure 4.9 shows the results of each of the two magnetic field tests. We calculate the lower bound for the total magnetic shielding factor for the entire SAT-MF1 deployment shielding by dividing the medians of the no shielding test response by the full shielding test result. We measure a lower bound of total magnetic shielding attenuation of 200.

We can divide the nominal magnitude of Earth's magnetic field at the Chile site by this total attenuation to get the expected magnitude of the detector response from the Earth's magnetic field. The maximum variation in the earth's magnetic field during SAT operation can be estimated using our nominal scan strategy, which involves scanning approximately $45°$ in azimuth at a constant elevation of roughly $50°$. The component of the earth's magnetic field at the Chilean site that lies in the azimuthal plane is ≈ 0.2 Gauss. Thus, we can put an upper bound of the injected magnetic field from the Earth to be less than 0.1 mGauss. The upper bound detector signal induced by this injected field (after attenuation due to shielding) is expected to be subdominant to other sources of 1/f at the same frequency.
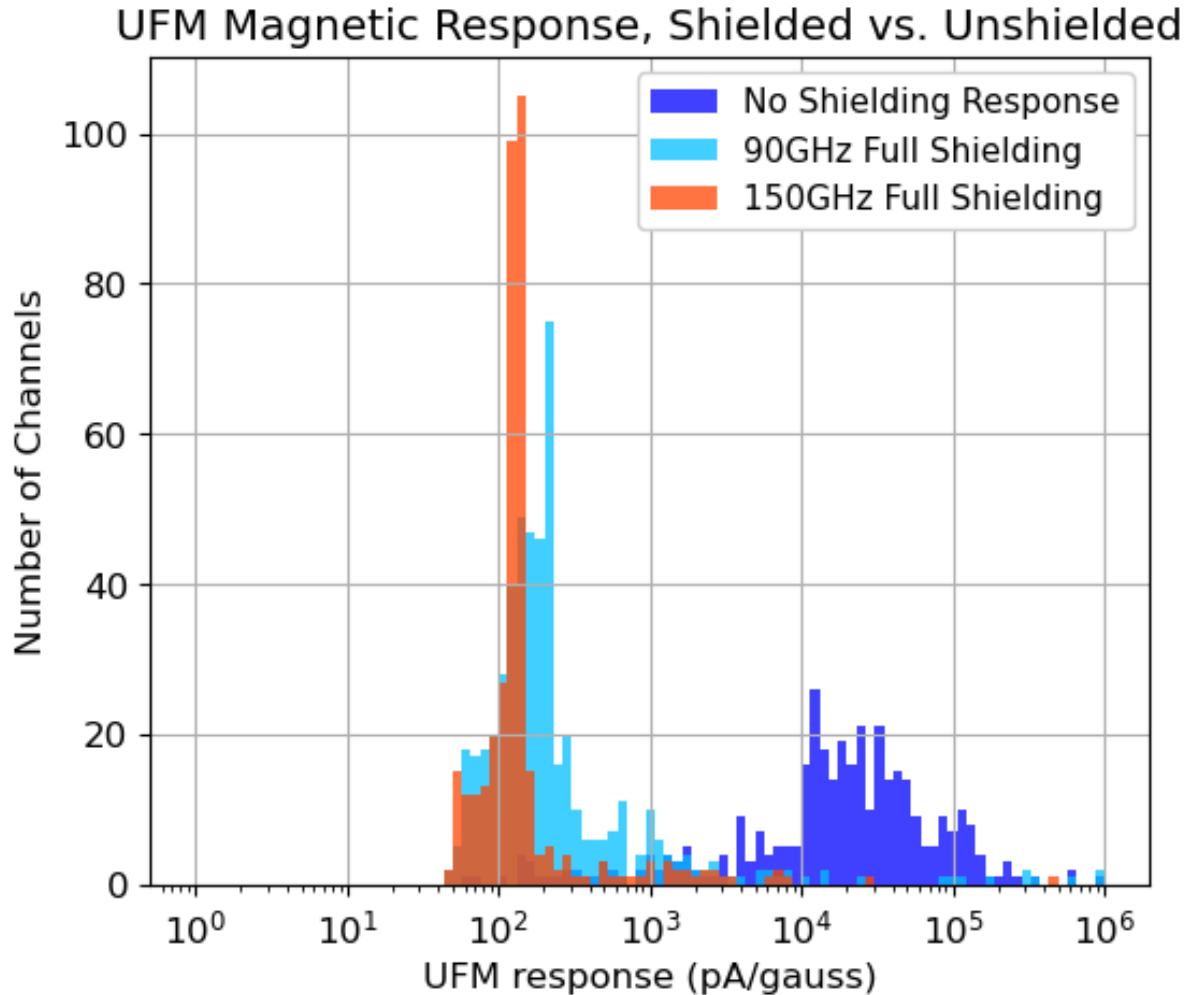
Figure 4.9. Comparison between the injected magnetic field tests done with a deployment caliber UFM in a test cryostat with no shielding and in the SAT-MF1 cryostat with full magnetic shielding. The detector population shown was coupled to feedhorns but with a reflective mask at the feedhorn aperture. The unshielded test (dark blue) exhibited unambiguous responses to the magnetic field in both 90 and 150 GHz channels. The shielded test produced no identifiable response above the noise floor of the detector which is used to provide an upper bound on the response level. The noise level varies by frequency band providing a 90 GHz distribution (light blue) and 150 GHz distribution (orange). The magnetic field strength is measured by a magnetometer external to the cryostat but at the same distance relative to the solenoid.

4.7.3 CHWP-generated magnetic fields

The CHWP magnetic pickup in dark detector and readout timestreams from the detector test unit is measured by examining the PSDs for peaks at multiples of the CHWP spin frequency. The measurements shown here were done before the still stage superconducting magnetic shield was installed. Clear evidence of HWP-induced pickup at the spin frequency was observed across detectors and resonators at multiple different HWP spin frequencies between $1 - 2\,Hz$. Pickup at both 1x and 2x the spin frequency was visible when spinning the HWP at $2\,Hz$, see Fig. 4.10. The strength of the CHWP pickup across detectors and resonators is consistent with the levels observed in Section 4.7.2. This strongly suggests that most of this pickup is due to a variable magnetic field generated by imperfections in the CHWP magnetic bearing. The lines have a narrow bandwidth set by the stability of HWP rotation, which is $\leq$ 10 mHz when PID control is used.

We also placed the external magnetometer above SAT-MF1 at an equivalent distance to the CHWP as the FPA and observed a clear magnetic field generated at the spin frequency. These results were observed at three distinct spin frequencies of $1\,Hz$, $1.5\,Hz$, and $2\,Hz$, providing unambiguous evidence that the pickup is associated with the spinning CHWP. The magnetometer recorded magnetic field pickup when the CHWP motor was turned off but the CHWP was still spinning, which indicates that the CHWP drive motor coils and corresponding fixed magnets do not generate a significant magnetic field fluctuation at the distance of the FPA, in line with predictions.

We expect the primary non-ideality of the rotor magnet to be a dipole, which is confirmed by the fact that the pickup in Fig. 4.10 is strongest at 1x the spin frequency (2 Hz), but higher order modes can also be present. Any pickup at higher multiples of the CHWP frequency is more significant for the SAT performance since the incoming polarization signal is modulated at four times the spin frequency. Therefore non-optical signals around this frequency, nominally 8 Hz, can be transferred to the demodulated data, resulting in potential systematics that would need to

be addressed in the analysis pipeline. While the 2x (4 Hz) line is clearly seen, we are unable to distinguish the 3x or higher order modes from the noise in the eight-hour timestream we used in this analysis. In particular, the 4x HWP signal is not visible above the integrated white noise level, which is an encouraging sign. The level of the higher order pickup in our detectors, and especially that of the 4x signal, will continue to be assessed in future testing as we integrate the deployment arrays in SAT-MF1 to ensure any systematic contribution from CHWP-associated magnetic fields is sub-dominant to other systematic sources or the white noise level.

4.8   Ground Shield

4.8.1   Why Have a Ground Shield?

The ground shield is shown in Figure 4.2 and Figure 4.11, along with the forebaffle and co-moving shield. Together, these three components comprise the warm baffling system of the SAT. The basic motivation for this baffling is simple: the ground is a thermal emitter with a temperature of ~ 300K, and the polarization anisotropies we are trying to measure are $< 1\mu$K. The microwave signal from the ground, then, provides a potentially huge source of contamination. This is significantly mitigated by the fact that only a small part of the telescope beam sees the ground (part of the so-called 'spillover' power), but the ground still provides a significant source of contamination that must be addressed.

A major help in mitigating ground contamination is that the SAT is attempting to measure the CMB anisotropies rather than the monopole. This means that isotropic sources of ground contamination are significantly less concerning than anistropic sources. In data processing this will be exploited by subtracting a background signal from the data, which removes much of the ground signal. The primary concerns when it comes to reducing ground contamination, therefore, are twofold: 1) Minimize the overall spillover onto the ground; and 2) *really* minimize spillover onto the ground that changes as the telescope scans.

1) is primarily accomplished by designing the optics inside the receiver so that the
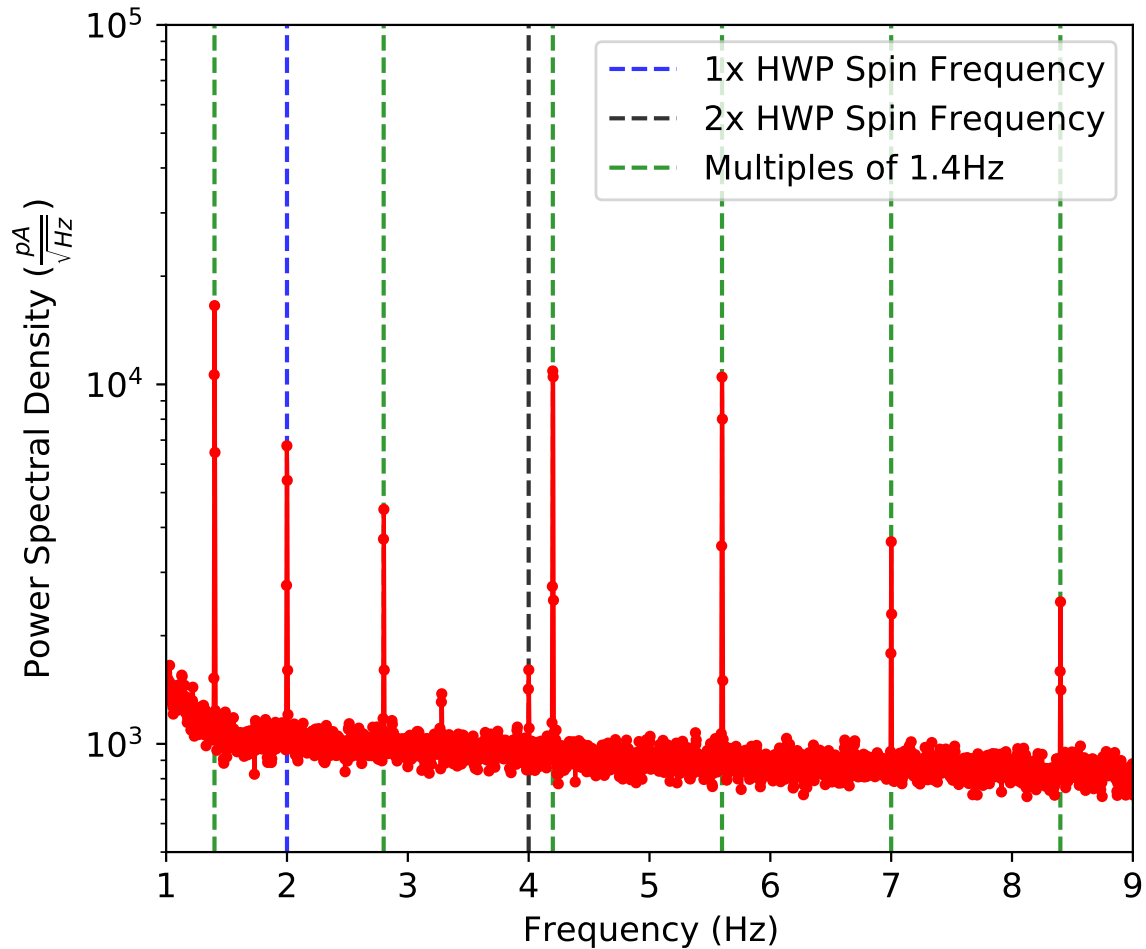
Figure 4.10. Narrow-bandwidth noise sources seen in a TES-coupled detector from the detector test module. Testing was performed without the superconducting magnetic shield installed. The pickup at 1x (2 Hz) and 2x (4 Hz) the HWP spin frequency is clearly visible. We do not detect pickup at 4x (8 Hz) the spin frequency which is the modulation frequency of the desired CMB polarization signal. The lines at multiples of 1.4 Hz are associated with the PTC motor drive frequency and are not seen in resonator-coupled channels. The unlabelled lines appear in both resonator-coupled and TES-coupled channels at equal strength, and are likely associated with the warm readout system.

Figure 4.11. An overview of the ground shield and other warm baffling. *Top Left:* A solidworks model of the ground shield. *Top Right:* The interior of the ground shield, with the co-moving shield mounted on the SATP. *Bottom Left:* All three ground shields fully constructed on site. *Bottom Right*: The interior of the ground shield with the SAT receiver forebaffle, but no co-moving shield. Pictures taken by Michael Randall, model by Grant Teply.
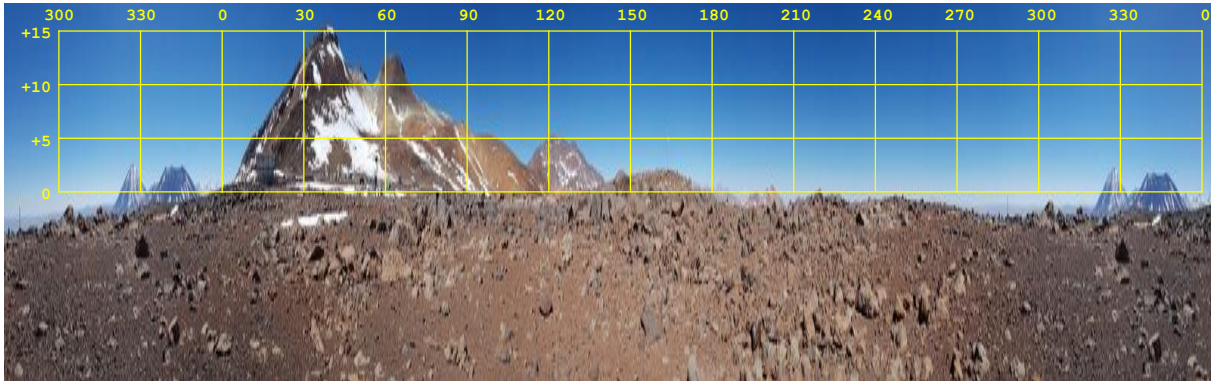
Figure 4.12. A view of the landscape from the site in azimuth and elevation. The image has been vertically stretched. The nearby mountain Cerro Toco has the highest elevation, at 15°. All other features are $\leq 5°$. Image credit: Paolo Calisse

telescope does not see much light directed too far away from the main beam. The reflecting portions of the warm baffling (the co-moving shield and ground shield) do play some role by ensuring that the spillover is directed towards the sky, which is much cooler than the ground in the microwave. It is impossible to completely eliminate spillover, though, and so 2) is where the warm baffling really comes in to play. The combination of all three baffling components ensures that the vast majority of the spillover does not see a change as the telescope scans, and therefore contributes only an isotropic signal. The landscape outside of the ground shield is decidedly anisotropic, and except for the top of the nearby mountain Cerro Toco (see Figure 4.12), light from all objects outside the ground shield must diffract at least twice in order to be been by any detector.

4.8.2 Optical Baffling Requirements

The optical requirements for the ground shield are a part of the overall requirements on the warm baffling system. I did not lead the design of these optical requirements but will briefly summarize them here, as they are important for understanding the ground shield mechanical design. The requirements were:

- The warm baffling must not interfere with the telescope's field of view.

- Rays greater than 40° away from the telescope pointing angle must not enter the telescope window.

- The spillover onto the warm baffling and ground, numerically estimated by simulations, must meet certain thresholds that depend on the observing frequency.

- All objects below 5° in elevation must diffract at least twice before entering the telescope window.

- The bottom of the forebaffle cone (near the telescope window) must not directly see Cerro Toco over the ground shield.

The first requirement is self-explanatory, and the second requirement stems from the need to avoid the sun and moon while observing. The final three requirements are based on the considerations outlined in Section 4.8.1. The spillover requirement numbers were predetermined from a sensitivity calculation that was done to meet the overall instrument science goals. The diffraction and Cerro Toco criteria require some additional explanation.

At the beginning of the design process, the requirement was simply that all objects outside the ground shield diffract twice before entering the telescope to minimize the anisotropic signal. However, this required the top of the forebaffle to not see Cerro Toco, which in turn required very large baffling components. It was then determined that the diffraction from the top of the forebaffle was very small, and the diffraction from the bottom of the forebaffle was more immportant, and the requirement was relaxed so that the bottom of the forebaffle cone must not directly see Cerro Toco over the ground shield. At the same time, to minimize scattering off of the forebaffle hitting the ground, it was determined that the top of the forebaffle should not see any object lower than 5° in elevation.

The result of this optimization yielded an microwave-absorbative conical forebaffle 1.70 m in length, a microwave-reflecting co-moving shield 2.3 m in length, and a ground shield with a radius of 8.42 m and a height of 5.66m. The forebaffle and shield move with the telescope as it

scans to provide an azimuth-independent signature for spillover. The purpose of the forebaffle is to block rays greater than $40°$ away from the telescope and absorb the largest chunk of the spillover on an microwave-black surface. The forebaffle is absorbative, rather than reflective, because it allows for greater control over reflections and unexpected sidelobes, although at the cost of higher spillover. The purpose of the co-moving shield is to help realize the double-diffraction criterion and reflect the vast majority of the remaining spillover to the sky. The purpose of the ground shield is to provide the final diffraction layer and reflect to sky the remaining spillover.

4.8.3 Mechanical Design Requirements

The ground shield requirements are shown in Figure 4.13, Table 4.3, and Table 4.4. The guiding principle was to create an azimuthally-symmetric structure that minimizes both its own emission and the ground emission seen by the telescope, subject to the dimensions noted in Section 4.8.2 and the relatively harsh environmental conditions of the Atacama Desert. This section will explain how this principle guided a number of design choices that led to the ground shield requirements.

The most important part of the ground shield is the upper portion, because the spillover onto the ground shield rapidly diminishes away from the top. Simulations show that 80% of the spillover is concentrated into the upper 2m, which is therefore where the design requirements are the most stringent. This portion of the ground shield will be referred to as the 'optical section'.

A key requirement for the optical section was azimuthal uniformity: we required that the structure deviate from the specified height (8.42m) and radius (5.66m) by no more than 5cm. This requirement effectively required a cylindrical ground shield, rather than a polygon. Although the latter would almost certainly have been easier to build, it induces azimuth-dependent ground pickup as the telescope scans. This has effect has been seen in other experiments that have constructed polygonal ground shields, and so we wanted to avoid that issue if possible.

The most important part of the optical section is the top edge, where light undergoes
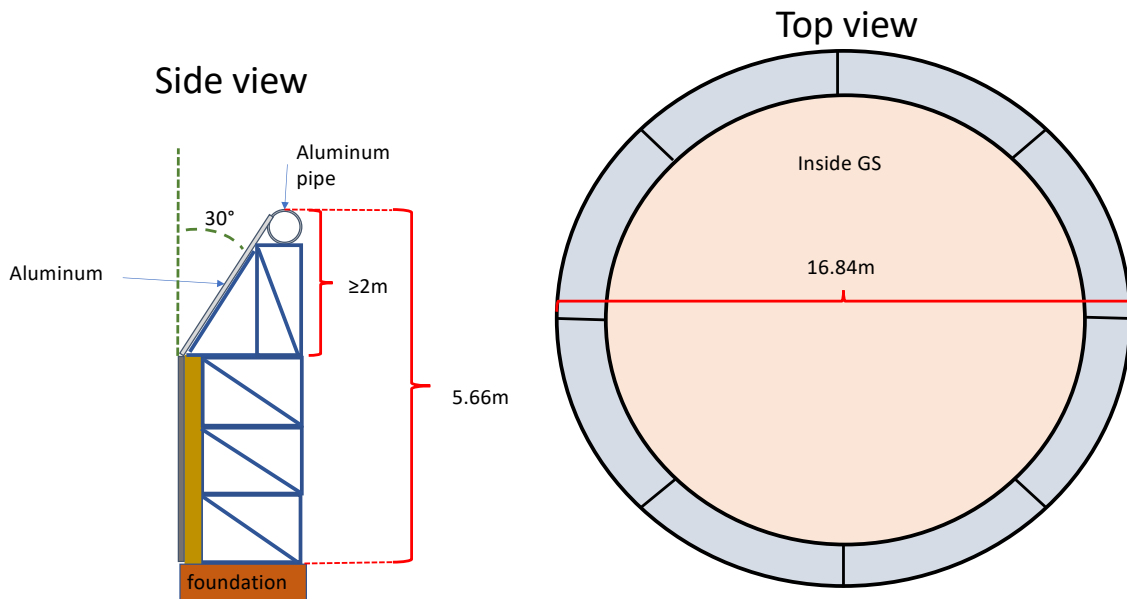
Figure 4.13. Diagram showing ground shield requirements as given to vendors during the Request For Proposal. The remainder of this caption is a direct copy of the text given to the prospective vendors. *A cross section and top-down view of the ground shield are shown. The interior, top portion will require an optical section made of aluminum. The optical section will help prevent thermal radiation from the ground from diffracting into the telescope field of view. The optical section should be as close to the inner wall as possible. It is not a precision mirror and does not need to satisfy especially tight tolerances. The interior of the structure should be as cylindrical as possible within structural constraints – more extensive support may be used on the exterior. The interior of the cylindrical section must be covered with metal to within 0.5m of the ground. The optical section will be tilted by 30°. The circular shape of the ground shield must be maintained, making the optical section conical.*

Table 4.3. The ground shield mechanical requirements, as given to prospective vendors during the Request for Proposal.

Parameter	Value
Optical section material	aluminum
Optical section sheet thickness	$\geq$ 2 mm
Localized deformation of optical section	< 3 mm
Radius at highest point	842 cm
Height at highest point	566 cm
Radius uniformity tolerance	< 5 cm
Height uniformity tolerance	< 5 cm
Length of optical section	$\geq$ 200 cm
Radius of curvature at the top of the optical section	$\geq$ 5 cm
Arc angle at the top of the optical section	$\geq$ 150 degrees
Structural components of the optical section not visible to the telescope	TRUE
No gaps between optical section panels	TRUE
Thermal strain relief	TRUE
Door width	3.5 m
Door height	3.5 m
Total allowable outer radius including support structures	9 m
Minimum allowable inner radius	6.5 m
All exposed components UV resistant	TRUE
All exposed components rust resistant	TRUE
Paint on outside fiberglass	Valspar "desert sand" WXD0055L OR "Beige" RAL 1001
Grounding to telescope cabling	TRUE
Human door	TRUE
Tilt of optical section	30 degrees
Metal below optical section	TRUE
Length at bottom of GS not covered by metal	$\leq$ 0.5 m

Table 4.4. The ground shield environment requirements, as given to prospective vendors during the Request for Proposal.

Parameter	Value
Location	Cerro Toco, Chile
Altitude	5190 m
Air temperature	-21 to +15 °C
Air temperature, maximum diurnal variation	30 °C, peak to peak
Air pressure	58 to 61 kPa
Relative humidity	0 to 90 %
Wind speed during observation	< 30 m/s
Wind speed, survival	60 m/s
Sand and dust, diameter	74 to 1000 μm
Sand and dust, concentration	1 g/m^3
Rain	22 mm/hr
Ice	1 cm
Snow	75 cm
Hail, survival	2 cm diameter at 25 m/s
Seismic acceleration at ground, survival	0.28g peak
Solar radiation, short wavelength	1290 W/m^2
Solar radiation, long wavelength	100 W/m^2

diffraction over the top of the ground shield. It was estimated[16] how much less optical power a rounded edge diffracts as compared to a straight edge. This effect increases with radius of curvature, and at 150 GHz there is an 80% reduction in optical power over a cylindrical surface with a radius of 5cm . The effect also decreases with wavelength, and so the minimum effect we expect is a 33% decrease at 30 GHz. For practical reasons, we limited the radius of curvature required to 5cm.

Another design decision involved whether the optical section should be absorbative or reflective in the microwave. The basic trade-off is the same for the forebaffle and co-moving shield: absorbing material provides better control of reflections and unexpected sidelobes, while reflecting material provides lower total optical loading. For the ground shield, however, the primary concern was practical. Trying to make the entire upper 2m of the ground shield absorbative would have been costly and a huge logistical challenge. It also posed a risk, because if the blackening material was damaged or peeled off, it would provide a highly non-uniform signature. Therefore it was determined that a reflective optical section, of unpainted aluminum, was an easier and more robust solution. We considered painting, which would have protected the aluminum and reduced thermal gradients. However, a special microwave-transparent paint would have been needed, as most commercially available paints are 'grey bodies' in the microwave, and this would have been too difficult and costly to apply.

Several requirements revolved around the deformations and gaps allowed in the the optical section. It is desirable to minimize these to preserve uniformity, but as a practical matter they are impossible to eliminate. Furthermore, it is difficult to set quantitative requirements on them that flow directly from the science goals, and the 3mm specification on local deformations was set to allow for inclusion of things like protruding rivet heads. Gaps are a natural part of the structure due to thermal expansion - a 3m section of aluminum panel, for example, will change size by 2.5mm under the $\Delta T = 35°K$ temperature swings normally experienced at site. However, a slit between two conducting surfaces produces a polarized signature [191], and so we required

---

[16]Lyman Page, private communication of unpublished work

that these be covered.

The tilt of the optical section, which was ultimately set at 30°, necessitated a revision of the requirements after a vendor was selected. While a tilt intuitively makes sense as a way to direct spillover onto the ground shield towards the sky, initially no tilt was specified, and the ground shield was essentially a big cylinder. This was because there is no direct or reflective path from the telescope window to the ground shield, and therefore the spillover onto the ground shield was seen as not important enough to warrant tilting, given the considerable perceived difficulties in constructing an aluminum cone nearly 17m in diameter.

Later it realized that this would in fact violate the 5° elevation diffraction criteria. The problem is reflections off of the ground shield, which would allow the telescope to see objects behind the telescope at $< 5°$ elevation through scattering (rather than specular reflections) off of the forebaffle. It was this scattering path that was ignored in the initial analysis. Although the microwave-absorbing surface of the forebaffle only allows for a small fraction of light to be scattered, simulations with a 1% scattering rate showed these backwards reflections could cause a significant problem, see Figure 4.14. This problem can be avoided by tilting the ground shield just a few degrees, but this back side lobe also poses a second issue for sun and moon avoidance. This can only be mitigated by tilting far enough that the back side lobe is entirely hidden within the existing sidelobe given by forebaffle scattering. A tilt angle of 30° accomplishes this, as shown in Figure 4.14. Fortunately, the ground shield vendor was able to accommodate the change in design relatively easily.

The rest of the structure below the optical section is less important, and was required to simply be a cylinder opaque to microwaves. The environmental considerations were standard for the rest of the site buildings. The most notable specification is the wind requirement. It is extremely windy at the site, with gusts up to 60 m/s, and this was the driving requirement on the size of the foundations, which were a significant portion of the cost of construction. Another practical reason for the existence of the ground shield is as wind protection for people working on the telescope. Although not optically necessary, it was for this reason that the ground shield
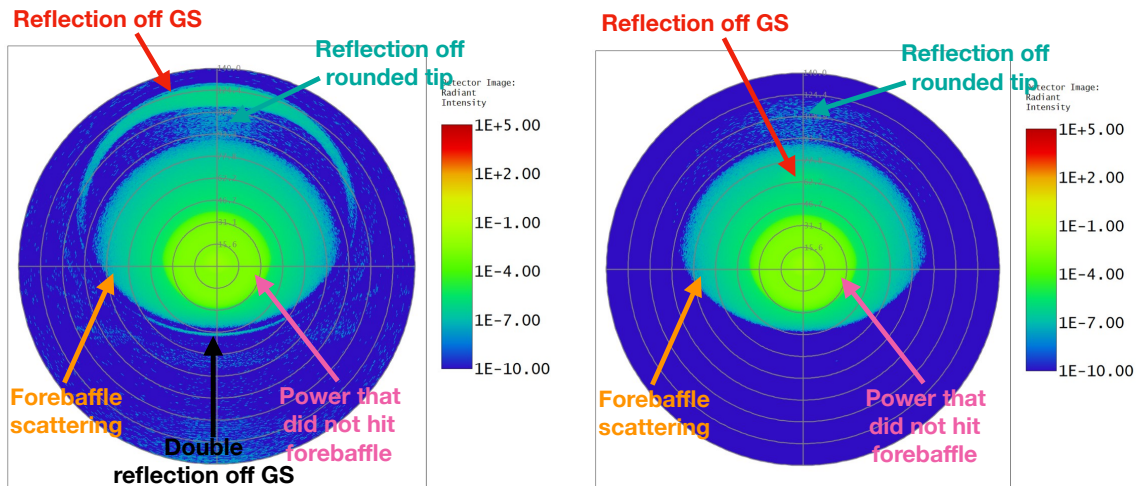
Figure 4.14. The distribution of optical power from forebaffle scattering given no tilt (left) or $30°$ tilt (right) of the upper 2m of the ground shield. The output is from a geometric optics simulation of a single detector beam in the telescope focal plane. The map coordinates are angular and centered in the direction of boresite pointing at the nominal observing elevation of $50°$, and the color shows the radiant intensity seen by the detector. The simulation assumes that the window scatters 1% of the main beam into 2π solid angle, and the forebaffle is 99% absorbative and the remaining 1% fully scatters. The left panel clearly shows a sidelobe that develops behind the telescope at an elevation of $\approx 0 - 20°$ due to reflection off of the ground shield (red arrow), violating the $5°$ diffraction criterion. The right panel shows how this sidelobe is absorbed into the main forebaffle scattering sidelobe with a tilt of $30°$, satisfying the criterion and avoiding additional issues with sun and moon avoidance. Figure credit: Fred Matsuda.

walls were required to be mostly flush with the ground, so as not to allow wind and wind-blown debris to get in.

4.8.4   Construction of the Ground Shield

The construction contract was won through a competitive bidding process by VyS, a Chilean construction company who was also responsible for constructing the SO foundations at the site[17]. They specialize in providing fiberglass structures for telecommunications equipment, and were able to provide a cylindrical and conical structure of molded fiberglass. The overall structure and dimensions are shown in Figure 4.11 and Figure 4.15.

Various components of the optical section are shown in Figure 4.16. The conical structure

---

[17]https://www.vys.cl/
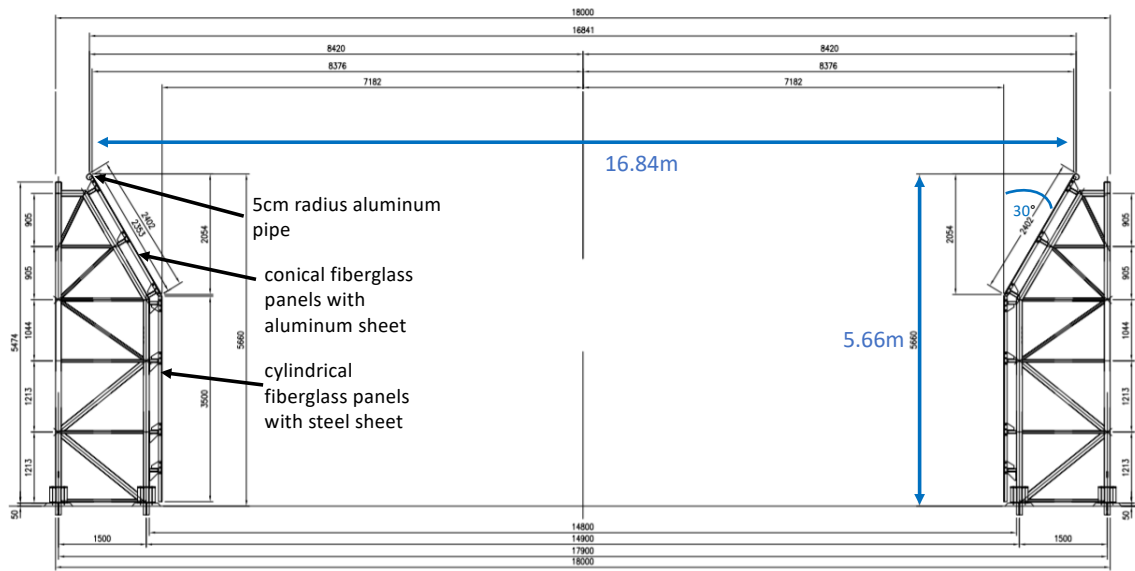
Figure 4.15. A cross section of the ground shield, showing dimensions and major components. Annotated from drawings provided by VyS.

of the optical section is provided by 18 custom-built fiberglass panels. Covering the panels are 54 pieces of aluminum sheet metal, arranged with 18 sheets azimuthally and three radially. There were two options to arrange the 54 panels: the second option was to put the long side of each aluminum sheet in the radial direction. The first option was chosen because it yields 18 rather than 54 radial seams, which generate an azimuth-dependent signal as the telescope scans. The seams that allow for thermal expansion were covered by small strips of aluminum.

The panels were initially slated to be epoxied in place, with no externally visible fasteners. This arrangement was tested with a mock-up of a small portion of the optical section, which revealed that the expoxy along was not sufficiently strong. This necessitated the addition of rivets along the panels, which are small enough to satisfy the requirement on deformations of the optical surface. Additionally, after the ground shields were installed, it was discovered that the optical section focused sunlight in such a way that portions of the SAT platform caught on fire. The aluminum panels were roughened to solve this issue.

The aluminum pipe at the top of the ground shield was also composed of 18 segments, each 3m long. The pipes were machine-bent into circular sections and joined together by the

insertion of a smaller section of pipe. As with the aluminum panels, a 5mm gap was left for thermal expansion, which was covered by the same aluminum strip.

The cylindrical structure of the ground shield is provided by fiberglass panels in a similar manner to the conical section, see Figure 4.17. The steel structure is hot-dipped galvanized and situated on a foundation of twelve concrete blocks, each 1.2m × 2m × 2m. The concrete structure was initially much larger, as the site wind spec of 60 m/s had not been converted to a sea level spec, where it is the equivalent of just 49 m/s. This conversion led to significant cost savings. A portion of the interior of the ground shield is paved to allow for vehicles to drive in and for people to walk around. This paved area includes two mounting points for a removable structure designed to allow for the telescope to be hoisted into place.

As of the time of writing this thesis, all three of the ground shields have been fully installed. The telescopes for each have been delivered and just begun operations, although the optical performance of the ground shields and warm baffling has not yet been determined.

4.9 Acknowledgements

I would like to give a big thanks to all of my SAT co-authors for years of work put into the telescope. On the ground shield: thanks to Fred Matsuda for doing the optical design, Michael Randall for taking pictures of the ground shield at the site, and Grant Teply for helping throughout the entire process.

Chapter 4, in part, is currently being prepared for submission for publication and appears in preprint as: Nicholas Galitzki, Tran Tsan, Jake Spisak, Michael Randall, Max Silva-Feaver, Joseph Seibert, Jacob Lashner, Shunsuke Adachi, Sean M. Adkins, Thomas Alford, Kam Arnold, Peter C. Ashton, Jason E. Austermann, Carlo Baccigalupi, Andrew Bazarko, James A. Beall, Sanah Bhimani, Bryce Bixler, Gabriele Coppi, Lance Corbett, Kevin D. Crowley, Kevin T. Crowley, Samuel Day-Weiss, Simon Dicker, Peter N. Dow, Cody J. Duell, Shannon M. Duff, Remington G. Gerras, John C. Groh, Jon E. Gudmundsson, Kathleen Harrington, Masaya
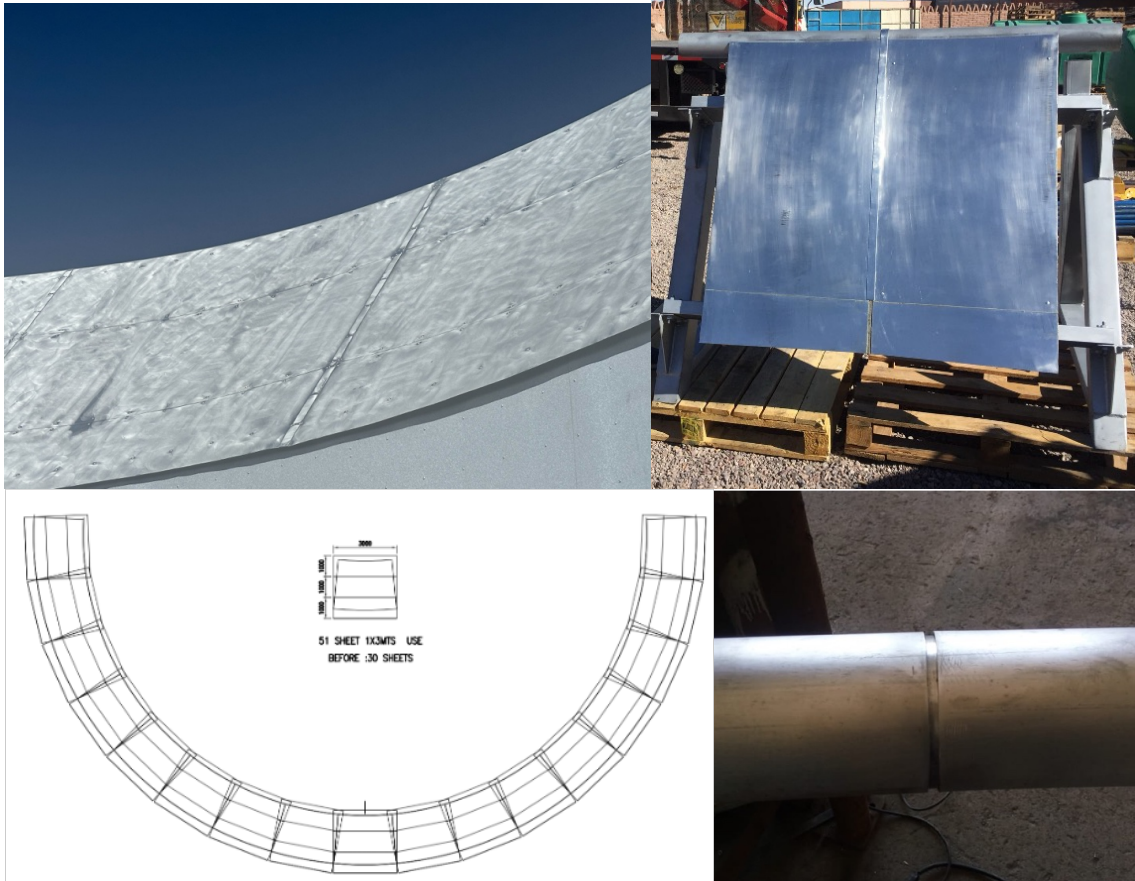
Figure 4.16. The optical section of the ground shield. *Top Left:* The optical section as built, showing the additional rivets added after the mock-up, and the surface roughening added after focused light caused a fire on the platform. *Top Right:* A mock-up built to test the design. The epoxy alone was not strong enough, so rivets were added to the final design. *Bottom Left:* The layout of the aluminum panels. *Bottom Right:* A pipe joint, achieved by inserting a small diameter pipe. Upper left image provided by Michael Randall, all other images and drawings provided by VyS.
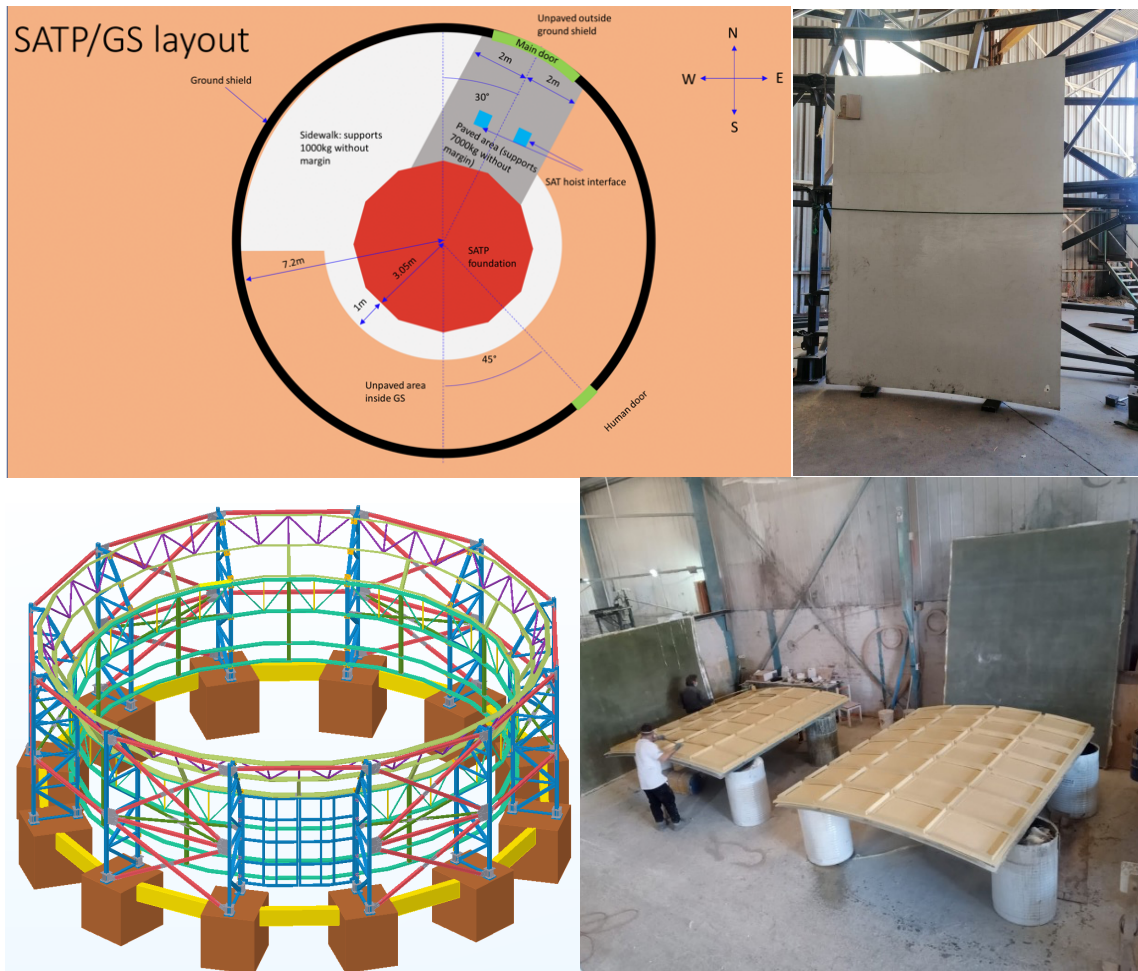
Figure 4.17. *Top Left:* The paved area inside of the ground shield. *Top Right:* A test fit of the cylindrical panels on the ground shield structure. *Bottom Left:* The steel structure and foundations of the ground shield. *Bottom Right:* The cylindrical panels being prepared in the workshop. All images besides top left provided by VyS.

Hasegawa, Erin Healy, Shawn W. Henderson, Johannes Hubmayr, Jeffrey Iuliano, Bradley R. Johnson, Brian Keating, Ben Keller, Kenji Kiuchi, Anna M. Kofman, Brian J. Koopman, Akito Kusaka, Adrian T. Lee, Richard A. Lew, Lawrence T. Lin, Michael J Link, Tammy J. Lucas, Marius Lungu, Aashrita Mangu, Jeffrey J McMahon, Amber D. Miller, Jenna E. Moore, Magdy Morshed, Hironobu Nakata, Federico Nati, Laura B. Newburgh, David V. Nguyen, Michael D. Niemack, Lyman A. Page, Kana Sakaguri, Yuki Sakurai, Mayuri Sathyanarayana Rao, Lauren J. Saunders, Jordan E. Shroyer, Junna Sugiyama, Osamu Tajima, Atsuto Takeuchi, Refilwe Tanah Bua, Grant Teply, Tomoki Terasaki, Joel N. Ullom, Jeffrey L. Van Lanen, Eve M. Vavagiakis, Michael R Vissers, Liam Walters, and Yuhan Wang. The simons observatory: Design, integration, and testing of the small aperture telescopes, 2024.
I was a first-tier author of this paper.

Bibliography

[1] Kevork Abazajian. Detection of Dark Matter Decay in the X-ray. In *astro2010: The Astronomy and Astrophysics Decadal Survey*, volume 2010, page 1, January 2009.

[2] Kevork Abazajian, George M. Fuller, and Mitesh Patel. Sterile neutrino hot, warm, and cold dark matter. *Physical Review D*, 64(2), may 2001.

[3] Kevork Abazajian, George M. Fuller, and Mitesh Patel. The Cosmological Bulk Neutrino Catastrophe. *Phys. Rev. Lett.*, 90:061301, 2003.

[4] Kevork Abazajian, George M. Fuller, and Wallace H. Tucker. Direct Detection of Warm Dark Matter in the X-Ray. *The Astrophysical Journal*, 562(2):593–604, December 2001.

[5] Kevork N. Abazajian, Peter Adshead, Zeeshan Ahmed, Steven W. Allen, David Alonso, Kam S. Arnold, Carlo Baccigalupi, James G. Bartlett, Nicholas Battaglia, Bradford A. Benson, Colin A. Bischoff, Julian Borrill, Victor Buza, Erminia Calabrese, Robert Caldwell, John E. Carlstrom, Clarence L. Chang, Thomas M. Crawford, Francis-Yan Cyr-Racine, Francesco De Bernardis, Tijmen de Haan, Sperello di Serego Alighieri, Joanna Dunkley, Cora Dvorkin, Josquin Errard, Giulio Fabbian, Stephen Feeney, Simone Ferraro, Jeffrey P. Filippini, Raphael Flauger, George M. Fuller, Vera Gluscevic, Daniel Green, Daniel Grin, Evan Grohs, Jason W. Henning, J. Colin Hill, Renee Hlozek, Gilbert Holder, William Holzapfel, Wayne Hu, Kevin M. Huffenberger, Reijo Keskitalo, Lloyd Knox, Arthur Kosowsky, John Kovac, Ely D. Kovetz, Chao-Lin Kuo, Akito Kusaka, Maude Le Jeune, Adrian T. Lee, Marc Lilley, Marilena Loverde, Mathew S. Madhavacheril, Adam Mantz, David J. E. Marsh, Jeffrey McMahon, Pieter Daniel Meerburg, Joel Meyers, Amber D. Miller, Julian B. Munoz, Ho Nam Nguyen, Michael D. Niemack, Marco Peloso, Julien Peloton, Levon Pogosian, Clement Pryke, Marco Raveri, Christian L. Reichardt, Graca Rocha, Aditya Rotti, Emmanuel Schaan, Marcel M. Schmittfull, Douglas Scott, Neelima Sehgal, Sarah Shandera, Blake D. Sherwin, Tristan L. Smith, Lorenzo Sorbo, Glenn D. Starkman, Kyle T. Story, Alexander van Engelen, Joaquin D. Vieira, Scott Watson, Nathan Whitehorn, and W. L. Kimmy Wu. Cmb-s4 science book, first edition, 2016.

[6] Kevork N. Abazajian, Peter Adshead, Zeeshan Ahmed, Steven W. Allen, David Alonso, Kam S. Arnold, Carlo Baccigalupi, James G. Bartlett, Nicholas Battaglia, Bradford A. Benson, Colin A. Bischoff, Julian Borrill, Victor Buza, Erminia Calabrese, Robert Caldwell,

John E. Carlstrom, Clarence L. Chang, Thomas M. Crawford, Francis-Yan Cyr-Racine, Francesco De Bernardis, Tijmen de Haan, Sperello di Serego Alighieri, Joanna Dunkley, Cora Dvorkin, Josquin Errard, Giulio Fabbian, Stephen Feeney, Simone Ferraro, Jeffrey P. Filippini, Raphael Flauger, George M. Fuller, Vera Gluscevic, Daniel Green, Daniel Grin, Evan Grohs, Jason W. Henning, J. Colin Hill, Renee Hlozek, Gilbert Holder, William Holzapfel, Wayne Hu, Kevin M. Huffenberger, Reijo Keskitalo, Lloyd Knox, Arthur Kosowsky, John Kovac, Ely D. Kovetz, Chao-Lin Kuo, Akito Kusaka, Maude Le Jeune, Adrian T. Lee, Marc Lilley, Marilena Loverde, Mathew S. Madhavacheril, Adam Mantz, David J. E. Marsh, Jeffrey McMahon, Pieter Daniel Meerburg, Joel Meyers, Amber D. Miller, Julian B. Munoz, Ho Nam Nguyen, Michael D. Niemack, Marco Peloso, Julien Peloton, Levon Pogosian, Clement Pryke, Marco Raveri, Christian L. Reichardt, Graca Rocha, Aditya Rotti, Emmanuel Schaan, Marcel M. Schmittfull, Douglas Scott, Neelima Sehgal, Sarah Shandera, Blake D. Sherwin, Tristan L. Smith, Lorenzo Sorbo, Glenn D. Starkman, Kyle T. Story, Alexander van Engelen, Joaquin D. Vieira, Scott Watson, Nathan Whitehorn, and W. L. Kimmy Wu. CMB-S4 Science Book, First Edition. *arXiv*, page arXiv:1610.02743, October 2016.

[7] Kevork N. Abazajian and Helena García Escudero. Visible in the laboratory and invisible in cosmology: Decaying sterile neutrinos. *Phys. Rev. D*, 108(12):123036, 2023.

[8] Kevork N. Abazajian and Alexander Kusenko. Hidden treasures: Sterile neutrinos as dark matter with miraculous abundance, structure formation for different production mechanisms, and a solution to the σ_8 problem. *Phys. Rev. D*, 100(10):103513, 2019.

[9] Maximilian H. Abitbol, Zeeshan Ahmed, Darcy Barron, Ritoban Basu Thakur, Amy N. Bender, Bradford A. Benson, Colin A. Bischoff, Sean A. Bryan, John E. Carlstrom, Clarence L. Chang, David T. Chuss, Kevin T. Crowley, Ari Cukierman, Tijmen de Haan, Matt Dobbs, Tom Essinger-Hileman, Jeffrey P. Filippini, Ken Ganga, Jon E. Gudmundsson, Nils W. Halverson, Shaul Hanany, Shawn W. Henderson, Charles A. Hill, Shuay-Pwu P. Ho, Johannes Hubmayr, Kent Irwin, Oliver Jeong, Bradley R. Johnson, Sarah A. Kernasovskiy, John M. Kovac, Akito Kusaka, Adrian T. Lee, Salatino Maria, Philip Mauskopf, Jeff J. McMahon, Lorenzo Moncelsi, Andrew W. Nadolski, Johanna M. Nagy, Michael D. Niemack, Roger C. O'Brient, Stephen Padin, Stephen C. Parshley, Clement Pryke, Natalie A. Roe, Karwan Rostem, John Ruhl, Sara M. Simon, Suzanne T. Staggs, Aritoki Suzuki, Eric R. Switzer, Osamu Tajima, Keith L. Thompson, Peter Timbie, Gregory S. Tucker, Joaquin D. Vieira, Abigail G. Vieregg, Benjamin Westbrook, Edward J. Wollack, Ki Won Yoon, Karl S. Young, and Edward Y. Young. CMB-S4 Technology Book, First Edition. *arXiv e-prints*, page arXiv:1706.02464, June 2017.

[10] Maximilian H. Abitbol, David Alonso, Sara M. Simon, Jack Lashner, Kevin T. Crowley, Aamir M. Ali, Susanna Azzoni, Carlo Baccigalupi, Darcy Barron, Michael L. Brown, Erminia Calabrese, Julien Carron, Yuji Chinone, Jens Chluba, Gabriele Coppi, Kevin D. Crowley, Mark Devlin, Jo Dunkley, Josquin Errard, Valentina Fanfani, Nicholas Galitzki, Martina Gerbino, J. Colin Hill, Bradley R. Johnson, Baptiste Jost, Brian Keating, Nicoletta

Krachmalnicoff, Akito Kusaka, Adrian T. Lee, Thibaut Louis, Mathew S. Madhavacheril, Heather McCarrick, Jeffrey McMahon, P. Daniel Meerburg, Federico Nati, Haruki Nishino, Lyman A. Page, Davide Poletti, Giuseppe Puglisi, Michael J. Randall, Aditya Rotti, Jacob Spisak, Aritoki Suzuki, Grant P. Teply, Clara Vergès, Edward J. Wollack, Zhilei Xu, and Mario Zannoni. The Simons Observatory: gain, bandpass and polarization-angle calibration requirements for B-mode searches. *Journal of Cosmology and Astroparticle Physics*, 2021(5):032, May 2021.

[11] Shunsuke Adachi, Tylor Adkins, Kam Arnold, Carlo Baccigalupi, Darcy Barron, Kolen Cheung, Yuji Chinone, Kevin T. Crowley, Josquin Errard, Giulio Fabbian, Chang Feng, Raphael Flauger, Takuro Fujino, Daniel Green, Masaya Hasegawa, Masashi Hazumi, Daisuke Kaneko, Nobuhiko Katayama, Brian Keating, Akito Kusaka, Adrian T. Lee, Yuto Minami, Haruki Nishino, Christian L. Reichardt, Praween Siritanasak, Jacob Spisak, Osamu Tajima, Satoru Takakura, Sayuri Takatori, Grant Paul Teply, and Kyohei Yamada. Constraints on axionlike polarization oscillations in the cosmic microwave background with polarbear, August 2023.

[12] Shunsuke Adachi, Tylor Adkins, Carlo Baccigalupi, Yuji Chinone, Kevin T. Crowley, Josquin Errard, Giulio Fabbian, Chang Feng, Takuro Fujino, Masaya Hasegawa, Masashi Hazumi, Oliver Jeong, Daisuke Kaneko, Brian Keating, Akito Kusaka, Adrian T. Lee, Anto I. Lonappan, Yuto Minami, Masaaki Murata, Lucio Piccirillo, Christian L. Reichardt, Praween Siritanasak, Jake Spisak, Satoru Takakura, Grant P. Teply, and Kyohei Yamada. Exploration of the polarization angle variability of the crab nebula with polarbear and its application to the search for axion-like particles, 2024.

[13] P. A. R. Ade, Z. Ahmed, M. Amiri, D. Barkats, R. Basu Thakur, C. A. Bischoff, D. Beck, J. J. Bock, H. Boenish, E. Bullock, V. Buza, J. R. Cheshire, J. Connors, J. Cornelison, M. Crumrine, A. Cukierman, E. V. Denison, M. Dierickx, L. Duband, M. Eiben, S. Fatigoni, J. P. Filippini, S. Fliescher, N. Goeckner-Wald, D. C. Goldfinger, J. Grayson, P. Grimes, G. Hall, G. Halal, M. Halpern, E. Hand, S. Harrison, S. Henderson, S. R. Hildebrandt, G. C. Hilton, J. Hubmayr, H. Hui, K. D. Irwin, J. Kang, K. S. Karkare, E. Karpel, S. Kefeli, S. A. Kernasovskiy, J. M. Kovac, C. L. Kuo, K. Lau, E. M. Leitch, A. Lennox, K. G. Megerian, L. Minutolo, L. Moncelsi, Y. Nakato, T. Namikawa, H. T. Nguyen, R. O'Brient, R. W. Ogburn, S. Palladino, T. Prouve, C. Pryke, B. Racine, C. D. Reintsema, S. Richter, A. Schillaci, R. Schwarz, B. L. Schmitt, C. D. Sheehy, A. Soliman, T. St. Germaine, B. Steinbach, R. V. Sudiwala, G. P. Teply, K. L. Thompson, J. E. Tolan, C. Tucker, A. D. Turner, C. Umiltà, C. Vergès, A. G. Vieregg, A. Wandui, A. C. Weber, D. V. Wiebe, J. Willmert, C. L. Wong, W. L. K. Wu, H. Yang, K. W. Yoon, E. Young, C. Yu, L. Zeng, C. Zhang, and S. Zhang. Bicep/*keck* xiv: Improved constraints on axionlike polarization oscillations in the cosmic microwave background. *Phys. Rev. D*, 105:022006, Jan 2022.

[14] P. A. R. Ade et al. BICEP/Keck XII: Constraints on axionlike polarization oscillations in the cosmic microwave background. *Phys. Rev. D*, 103(4):042002, 2021.

[15] P. A. R. Ade et al. Improved Constraints on Primordial Gravitational Waves using Planck, WMAP, and BICEP/Keck Observations through the 2018 Observing Season. *Phys. Rev. Lett.*, 127(15):151301, 2021.

[16] Peter Ade, James Aguirre, Zeeshan Ahmed, Simone Aiola, Aamir Ali, David Alonso, Marcelo A. Alvarez, Kam Arnold, Peter Ashton, Jason Austermann, Humna Awan, Carlo Baccigalupi, Taylor Baildon, Darcy Barron, Nick Battaglia, Richard Battye, Eric Baxter, Andrew Bazarko, James A. Beall, Rachel Bean, Dominic Beck, Shawn Beckman, Benjamin Beringue, Federico Bianchini, Steven Boada, David Boettger, J. Richard Bond, Julian Borrill, Michael L. Brown, Sarah Marie Bruno, Sean Bryan, Erminia Calabrese, Victoria Calafut, Paolo Calisse, Julien Carron, Anthony Challinor, Grace Chesmore, Yuji Chinone, Jens Chluba, Hsiao-Mei Sherry Cho, Steve Choi, Gabriele Coppi, Nicholas F. Cothard, Kevin Coughlin, Devin Crichton, Kevin D. Crowley, Kevin T. Crowley, Ari Cukierman, John M. D'Ewart, Rolando Dünner, Tijmen de Haan, Mark Devlin, Simon Dicker, Joy Didier, Matt Dobbs, Bradley Dober, Cody J. Duell, Shannon Duff, Adri Duivenvoorden, Jo Dunkley, John Dusatko, Josquin Errard, Giulio Fabbian, Stephen Feeney, Simone Ferraro, Pedro Fluxà , Katherine Freese, Josef C. Frisch, Andrei Frolov, George Fuller, Brittany Fuzia, Nicholas Galitzki, Patricio A. Gallardo, Jose Tomas Galvez Ghersi, Jiansong Gao, Eric Gawiser, Martina Gerbino, Vera Gluscevic, Neil Goeckner-Wald, Joseph Golec, Sam Gordon, Megan Gralla, Daniel Green, Arpi Grigorian, John Groh, Chris Groppi, Yilun Guan, Jon E. Gudmundsson, Dongwon Han, Peter Hargrave, Masaya Hasegawa, Matthew Hasselfield, Makoto Hattori, Victor Haynes, Masashi Hazumi, Yizhou He, Erin Healy, Shawn W. Henderson, Carlos Hervias-Caimapo, Charles A. Hill, J. Colin Hill, Gene Hilton, Matt Hilton, Adam D. Hincks, Gary Hinshaw, Renée Hložek, Shirley Ho, Shuay-Pwu Patty Ho, Logan Howe, Zhiqi Huang, Johannes Hubmayr, Kevin Huffenberger, John P. Hughes, Anna Ijjas, Margaret Ikape, Kent Irwin, Andrew H. Jaffe, Bhuvnesh Jain, Oliver Jeong, Daisuke Kaneko, Ethan D. Karpel, Nobuhiko Katayama, Brian Keating, Sarah S. Kernasovskiy, Reijo Keskitalo, Theodore Kisner, Kenji Kiuchi, Jeff Klein, Kenda Knowles, Brian Koopman, Arthur Kosowsky, Nicoletta Krachmalnicoff, Stephen E. Kuenstner, Chao-Lin Kuo, Akito Kusaka, Jacob Lashner, Adrian Lee, Eunseong Lee, David Leon, Jason S.-Y. Leung, Antony Lewis, Yaqiong Li, Zack Li, Michele Limon, Eric Linder, Carlos Lopez-Caraballo, Thibaut Louis, Lindsay Lowry, Marius Lungu, Mathew Madhavacheril, Daisy Mak, Felipe Maldonado, Hamdi Mani, Ben Mates, Frederick Matsuda, Loïc Maurin, Phil Mauskopf, Andrew May, Nialh McCallum, Chris McKenney, Jeff McMahon, P. Daniel Meerburg, Joel Meyers, Amber Miller, Mark Mirmelstein, Kavilan Moodley, Moritz Munchmeyer, Charles Munson, Sigurd Naess, Federico Nati, Martin Navaroli, Laura Newburgh, Ho Nam Nguyen, Michael Niemack, Haruki Nishino, John Orlowski-Scherer, Lyman Page, Bruce Partridge, Julien Peloton, Francesca Perrotta, Lucio Piccirillo, Giampaolo Pisano, Davide Poletti, Roberto Puddu, Giuseppe Puglisi, Chris Raum, Christian L. Reichardt, Mathieu Remazeilles, Yoel Rephaeli, Dominik Riechers, Felipe Rojas, Anirban Roy, Sharon Sadeh, Yuki Sakurai, Maria Salatino, Mayuri Sathyanarayana Rao, Emmanuel Schaan, Marcel Schmittfull, Neelima Sehgal, Joseph Seibert, Uros Seljak, Blake Sherwin, Meir Shimon, Carlos Sierra, Jonathan Sievers, Precious Sikhosana, Maximiliano Silva-Feaver, Sara M. Simon, Adrian Sinclair, Praween

Siritanasak, Kendrick Smith, Stephen R. Smith, David Spergel, Suzanne T. Staggs, George Stein, Jason R. Stevens, Radek Stompor, Aritoki Suzuki, Osamu Tajima, Satoru Takakura, Grant Teply, Daniel B. Thomas, Ben Thorne, Robert Thornton, Hy Trac, Calvin Tsai, Carole Tucker, Joel Ullom, Sunny Vagnozzi, Alexander van Engelen, Jeff Van Lanen, Daniel D. Van Winkle, Eve M. Vavagiakis, Clara Vergès, Michael Vissers, Kasey Wagoner, Samantha Walker, Jon Ward, Ben Westbrook, Nathan Whitehorn, Jason Williams, Joel Williams, Edward J. Wollack, Zhilei Xu, Byeonghee Yu, Cyndia Yu, Fernando Zago, Hezi Zhang, and Ningfeng Zhu and. The simons observatory: science goals and forecasts. *Journal of Cosmology and Astroparticle Physics*, 2019(02):056–056, feb 2019.

[17] Peter A. R. Ade, Kam Arnold, Matt Atlas, Carlo Baccigalupi, Darcy Barron, David Boettger, Julian Borrill, Scott Chapman, Yuji Chinone, Ari Cukierman, Matt Dobbs, Anne Ducout, Rolando Dunner, Tucker Elleflot, Josquin Errard, Giulio Fabbian, Stephen Feeney, Chang Feng, Adam Gilbert, Neil Goeckner-Wald, John Groh, Grantland Hall, Nils W. Halverson, Masaya Hasegawa, Kaori Hattori, Masashi Hazumi, Charles Hill, William L. Holzapfel, Yasuto Hori, Logan Howe, Yuki Inoue, Gregory C. Jaehnig, Andrew H. Jaffe, Oliver Jeong, Nobuhiko Katayama, Jonathan P. Kaufman, Brian Keating, Zigmund Kermish, Reijo Keskitalo, Theodore Kisner, Akito Kusaka, Maude Le Jeune, Adrian T. Lee, Erik M. Leitch, David Leon, Yun Li, Eric Linder, Lindsay Lowry, Frederick Matsuda, Tomotake Matsumura, Nathan Miller, Josh Montgomery, Michael J. Myers, Martin Navaroli, Haruki Nishino, Takahiro Okamura, Hans Paar, Julien Peloton, Levon Pogosian, Davide Poletti, Giuseppe Puglisi, Christopher Raum, Gabriel Rebeiz, Christian L. Reichardt, Paul L. Richards, Colin Ross, Kaja M. Rotermund, David E. Schenck, Blake D. Sherwin, Meir Shimon, Ian Shirley, Praween Siritanasak, Graeme Smecher, Nathan Stebor, Bryan Steinbach, Aritoki Suzuki, Jun ichi Suzuki, Osamu Tajima, Satoru Takakura, Alexei Tikhomirov, Takayuki Tomaru, Nathan Whitehorn, Brandon Wilson, Amit Yadav, Alex Zahn, and Oliver Zahn and. POLARBEAR constraints on cosmic birefringence and primordial magnetic fields. *Physical Review D*, 92(12), dec 2015.

[18] R. Adhikari, M. Agostini, N. Anh Ky, T. Araki, M. Archidiacono, M. Bahr, J. Baur, J. Behrens, F. Bezrukov, P.S. Bhupal Dev, D. Borah, A. Boyarsky, A. de Gouvea, C.A. de S. Pires, H.J. de Vega, A.G. Dias, P. Di Bari, Z. Djurcic, K. Dolde, H. Dorrer, M. Durero, O. Dragoun, M. Drewes, G. Drexlin, Ch.E. Düllmann, K. Eberhardt, S. Eliseev, C. Enss, N.W. Evans, A. Faessler, P. Filianin, V. Fischer, A. Fleischmann, J.A. Formaggio, J. Franse, F.M. Fraenkle, C.S. Frenk, G. Fuller, L. Gastaldo, A. Garzilli, C. Giunti, F. Glück, M.C. Goodman, M.C. Gonzalez-Garcia, D. Gorbunov, J. Hamann, V. Hannen, S. Hannestad, S.H. Hansen, C. Hassel, J. Heeck, F. Hofmann, T. Houdy, A. Huber, D. Iakubovskyi, A. Ianni, A. Ibarra, R. Jacobsson, T. Jeltema, J. Jochum, S. Kempf, T. Kieck, M. Korzeczek, V. Kornoukhov, T. Lachenmaier, M. Laine, P. Langacker, T. Lasserre, J. Lesgourgues, D. Lhuillier, Y.F. Li, W. Liao, A.W. Long, M. Maltoni, G. Mangano, N.E. Mavromatos, N. Menci, A. Merle, S. Mertens, A. Mirizzi, B. Monreal, A. Nozik, A. Neronov, V. Niro, Y. Novikov, L. Oberauer, E. Otten, N. Palanque-Delabrouille, M. Pallavicini, V.S. Pantuev, E. Papastergis, S. Parke, S. Pascoli, S. Pastor, A. Patwardhan, A. Pilaftsis, D.C. Radford, P.C.-O. Ranitzsch, O. Rest, D.J. Robinson, P.S. Rodrigues da Silva, O. Ruchayskiy, N.G.

Sanchez, M. Sasaki, N. Saviano, A. Schneider, F. Schneider, T. Schwetz, S. Schönert, S. Scholl, F. Shankar, R. Shrock, N. Steinbrink, L. Strigari, F. Suekane, B. Suerfu, R. Takahashi, N. Thi Hong Van, I. Tkachev, M. Totzauer, Y. Tsai, C.G. Tully, K. Valerius, J.W.F. Valle, D. Venos, M. Viel, M. Vivier, M.Y. Wang, C. Weinheimer, K. Wendt, L. Winslow, J. Wolf, M. Wurm, Z. Xing, S. Zhou, and K. Zuber. A white paper on kev sterile neutrino dark matter. *Journal of Cosmology and Astroparticle Physics*, 2017(01):025–025, January 2017.

[19] Susmita Adhikari et al. Astrophysical Tests of Dark Matter Self-Interactions. *arXiv*, 7 2022.

[20] M. Aker et al. Search for keV-scale sterile neutrinos with the first KATRIN data. *Eur. Phys. J. C*, 83(8):763, 2023.

[21] Aamir M. Ali, Shunsuke Adachi, Kam Arnold, Peter Ashton, Andrew Bazarko, Yuji Chinone, Gabriele Coppi, Lance Corbett, Kevin D. Crowley, Kevin T. Crowley, Mark Devlin, Simon Dicker, Shannon Duff, Chris Ellis, Nicholas Galitzki, Neil Goeckner-Wald, Kathleen Harrington, Erin Healy, Charles A. Hill, Shuay-Pwu Patty Ho, Johannes Hubmayr, Brian Keating, Kenji Kiuchi, Akito Kusaka, Adrian T. Lee, Michael Ludlam, Aashrita Mangu, Frederick Matsuda, Heather McCarrick, Federico Nati, Michael D. Niemack, Haruki Nishino, John Orlowski-Scherer, Mayuri Sathyanarayana Rao, Christopher Raum, Yuki Sakurai, Maria Salatino, Trevor Sasse, Joseph Seibert, Carlos Sierra, Maximiliano Silva-Feaver, Jacob Spisak, Sara M. Simon, Suzanne Staggs, Osamu Tajima, Grant Teply, Tran Tsan, Edward Wollack, Bejamin Westbrook, Zhilei Xu, Mario Zannoni, and Ningfeng Zhu. Small Aperture Telescopes for the Simons Observatory. *Journal of Low Temperature Physics*, April 2020.

[22] Gonzalo Alonso-Álvarez and James M. Cline. Sterile neutrino production at small mixing in the early universe. *Physics Letters B*, 833:137278, oct 2022.

[23] and N. Aghanim, Y. Akrami, M. Ashdown, J. Aumont, C. Baccigalupi, M. Ballardini, A. J. Banday, R. B. Barreiro, N. Bartolo, S. Basak, R. Battye, K. Benabed, J.-P. Bernard, M. Bersanelli, P. Bielewicz, J. J. Bock, J. R. Bond, J. Borrill, F. R. Bouchet, F. Boulanger, M. Bucher, C. Burigana, R. C. Butler, E. Calabrese, J.-F. Cardoso, J. Carron, A. Challinor, H. C. Chiang, J. Chluba, L. P. L. Colombo, C. Combet, D. Contreras, B. P. Crill, F. Cuttaia, P. de Bernardis, G. de Zotti, J. Delabrouille, J.-M. Delouis, E. Di Valentino, J. M. Diego, O. Doré, M. Douspis, A. Ducout, X. Dupac, S. Dusini, G. Efstathiou, F. Elsner, T. A. Enßlin, H. K. Eriksen, Y. Fantaye, M. Farhang, J. Fergusson, R. Fernandez-Cobos, F. Finelli, F. Forastieri, M. Frailis, A. A. Fraisse, E. Franceschi, A. Frolov, S. Galeotta, S. Galli, K. Ganga, R. T. Génova-Santos, M. Gerbino, T. Ghosh, J. González-Nuevo, K. M. Górski, S. Gratton, A. Gruppuso, J. E. Gudmundsson, J. Hamann, W. Handley, F. K. Hansen, D. Herranz, S. R. Hildebrandt, E. Hivon, Z. Huang, A. H. Jaffe, W. C. Jones, A. Karakci, E. Keihänen, R. Keskitalo, K. Kiiveri, J. Kim, T. S. Kisner, L. Knox, N. Krachmalnicoff, M. Kunz, H. Kurki-Suonio, G. Lagache, J.-M. Lamarre, A. Lasenby,

M. Lattanzi, C. R. Lawrence, M. Le Jeune, P. Lemos, J. Lesgourgues, F. Levrier, A. Lewis, M. Liguori, P. B. Lilje, M. Lilley, V. Lindholm, M. López-Caniego, P. M. Lubin, Y.-Z. Ma, J. F. Macías-Pérez, G. Maggio, D. Maino, N. Mandolesi, A. Mangilli, A. Marcos-Caballero, M. Maris, P. G. Martin, M. Martinelli, E. Martínez-González, S. Matarrese, N. Mauri, J. D. McEwen, P. R. Meinhold, A. Melchiorri, A. Mennella, M. Migliaccio, M. Millea, S. Mitra, M.-A. Miville-Deschênes, D. Molinari, L. Montier, G. Morgante, A. Moss, P. Natoli, H. U. Nørgaard-Nielsen, L. Pagano, D. Paoletti, B. Partridge, G. Patanchon, H. V. Peiris, F. Perrotta, V. Pettorino, F. Piacentini, L. Polastri, G. Polenta, J.-L. Puget, J. P. Rachen, M. Reinecke, M. Remazeilles, A. Renzi, G. Rocha, C. Rosset, G. Roudier, J. A. Rubiño-Martín, B. Ruiz-Granados, L. Salvati, M. Sandri, M. Savelainen, D. Scott, E. P. S. Shellard, C. Sirignano, G. Sirri, L. D. Spencer, R. Sunyaev, A.-S. Suur-Uski, J. A. Tauber, D. Tavagnacco, M. Tenti, L. Toffolatti, M. Tomasi, T. Trombetti, L. Valenziano, J. Valiviita, B. Van Tent, L. Vibert, P. Vielva, F. Villa, N. Vittorio, B. D. Wandelt, I. K. Wehus, M. White, S. D. M. White, A. Zacchei, and A. Zonca. Planck 2018 results. *Astronomy and Astrophysics*, 641:A6, sep 2020.

[24] Carlos A. Argüelles, Vedran Brdar, and Joachim Kopp. Production of keV Sterile Neutrinos in Supernovae: New Constraints and Gamma Ray Observables. *Phys. Rev. D*, 99(4):043012, 2019.

[25] K. Arnold, P. A. R. Ade, A. E. Anthony, D. Barron, D. Boettger, J. Borrill, S. Chapman, Y. Chinone, M. A. Dobbs, J. Errard, G. Fabbian, D. Flanigan, G. Fuller, A. Ghribi, W. Grainger, N. Halverson, M. Hasegawa, K. Hattori, M. Hazumi, W. L. Holzapfel, J. Howard, P. Hyland, A. Jaffe, B. Keating, Z. Kermish, T. Kisner, M. Le Jeune, A. T. Lee, E. Linder, M. Lungu, F. Matsuda, T. Matsumura, N. J. Miller, X. Meng, H. Morii, S. Moyerman, M. J. Myers, H. Nishino, H. Paar, E. Quealy, C. Reichardt, P. L. Richards, C. Ross, A. Shimizu, C. Shimmin, M. Shimon, M. Sholl, P. Siritanasak, H. Speiler, N. Stebor, B. Steinbach, R. Stompor, A. Suzuki, T. Tomaru, C. Tucker, and O. Zahn. The bolometric focal plane array of the POLARBEAR CMB experiment. In Wayne S. Holland, editor, *SPIE Proceedings*. SPIE, sep 2012.

[26] Asimina Arvanitaki, Savas Dimopoulos, Sergei Dubovsky, Nemanja Kaloper, and John March-Russell. String axiverse. *Physical Review D*, 81(12), jun 2010.

[27] Takehiko Asaka, Steve Blanchet, and Mikhail Shaposhnikov. The nuMSM, dark matter and neutrino masses. *Phys. Lett. B*, 631:151–156, 2005.

[28] Takehiko Asaka, Mikko Laine, and Mikhail Shaposhnikov. Lightest sterile neutrino abundance within the nuMSM. *Journal of High Energy Physics*, 2007(01):091, 2007. [Erratum: JHEP 02, 028 (2015)].

[29] Takehiko Asaka and Mikhail Shaposhnikov. The νMSM, dark matter and baryon asymmetry of the universe. *Phys. Lett. B*, 620:17–26, 2005.

[30] Takehiko Asaka, Mikhail Shaposhnikov, and Alexander Kusenko. Opening a new window for warm dark matter. *Phys. Lett. B*, 638:401–406, 2006.

[31] Maria Dias Astros and Stefan Vogl. Boosting the production of sterile neutrino dark matter with self-interactions. *arXiv*, 7 2023.

[32] A. Baha Balantekin, George M. Fuller, Anupam Ray, and Anna M. Suliga. Probing self-interacting sterile neutrino dark matter with the diffuse supernova neutrino background. *Phys. Rev. D*, 108:123011, Dec 2023.

[33] V. Barger, R. J. N. Phillips, and S. Sarkar. Remarks on the KARMEN anomaly. *Physics Letters B*, 352:365–371, 1995.

[34] Aritra Basu, Jishnu Goswami, Dominik J. Schwarz, and Yuko Urakawa. Searching for Axionlike Particles under Strong Gravitational Lenses. *Phys. Rev. Lett.*, 126(19):191102, 2021.

[35] Asher Berlin and Dan Hooper. Axion-Assisted Production of Sterile Neutrino Dark Matter. *Phys. Rev. D*, 95(7):075017, 2017.

[36] F. Bezrukov, A. Chudaykin, and D. Gorbunov. Hiding an elephant: heavy sterile neutrino with large mixing angle does not contradict cosmology. *Journal of Cosmology and Astroparticle Physics*, 2017(06):051–051, June 2017.

[37] F. Bezrukov, A. Chudaykin, and D. Gorbunov. Induced resonance makes light sterile neutrino Dark Matter cool. *Phys. Rev. D*, 99(8):083507, 2019.

[38] F. Bezrukov, A. Chudaykin, and D. Gorbunov. Scalar induced resonant sterile neutrino production in the early Universe. *Phys. Rev. D*, 101(10):103516, 2020.

[39] Patrick D. Bolton, Frank F. Deppisch, and P. S. Bhupal Dev. Neutrinoless double beta decay versus other probes of heavy sterile neutrinos. *Journal of High Energy Physics*, 2020(03):170, 2020.

[40] E. Borriello, M. Paolillo, G. Miele, G. Longo, and R. Owen. Constraints on sterile neutrino dark matter from XMM-Newton observations of M33. *Monthly Notices of the Royal Astronomical Society*, 425(3):1628–1632, September 2012.

[41] A. Boyarsky, M. Drewes, T. Lasserre, S. Mertens, and O. Ruchayskiy. Sterile neutrino Dark Matter. *Prog. Part. Nucl. Phys.*, 104:1–45, 2019.

[42] Alexey Boyarsky, Denys Malyshev, Andrey Neronov, and Oleg Ruchayskiy. Constraining dark matter properties with spi. *Monthly Notices of the Royal Astronomical Society*, 387(4):1345–1360, July 2008.

[43] Alexey Boyarsky, Denys Malyshev, Andrey Neronov, and Oleg Ruchayskiy. Constraining DM properties with SPI. *Mon. Not. Roy. Astron. Soc.*, 387:1345, 2008.

[44] Alexey Boyarsky, A. Neronov, Oleg Ruchayskiy, and M. Shaposhnikov. Constraints on sterile neutrino as a dark matter candidate from the diffuse x-ray background. *Mon. Not. Roy. Astron. Soc.*, 370:213–218, 2006.

[45] Torsten Bringmann, Paul Frederik Depta, Marco Hufnagel, Jörn Kersten, Joshua T. Ruderman, and Kai Schmidt-Hoberg. Minimal sterile neutrino dark matter. *Phys. Rev. D*, 107(7):L071702, 2023.

[46] Manuel A. Buen-Abad, JiJi Fan, and Chen Sun. Constraints on axions from cosmic distance measurements. *JHEP*, 02(2):103, 2022.

[47] Yi Cai, Juan Herrero-García, Michael A. Schmidt, Avelino Vicente, and Raymond R. Volkas. From the trees to the forest: a review of radiative neutrino mass models. *Front. in Phys.*, 5:63, 2017.

[48] Allen Caldwell, Gia Dvali, Bé la Majorovits, Alexander Millar, Georg Raffelt, Javier Redondo, Olaf Reimann, Frank Simon, and Frank Steffen and. Dielectric haloscopes: A new way to detect axion dark matter. *Physical Review Letters*, 118(9), mar 2017.

[49] Andrea Caputo, Laura Sberna, Miguel Frías, Diego Blas, Paolo Pani, Lijing Shao, and Wenming Yan. Constraints on millicharged dark matter and axionlike particles from timing of radio waves. *Phys. Rev. D*, 100:063515, Sep 2019.

[50] Sean M. Carroll. Quintessence and the rest of the world: Suppressing long-range interactions. *Physical Review Letters*, 81(15):3067–3070, oct 1998.

[51] CAST Collaboration. New CAST limit on the axion–photon interaction. *Nature Physics*, 13(6):584–590, may 2017.

[52] Andrés Castillo, Jorge Martin-Camalich, Jorge Terol-Calvo, Diego Blas, Andrea Caputo, Ricardo Tanausú Génova Santos, Laura Sberna, Michael Peel, and Jose Alberto Rubiño Martín. Searching for dark-matter waves with PPTA and QUIJOTE pulsar polarimetry. *Journal of Cosmology and Astroparticle Physics*, 06(06):014, 2022.

[53] Gary P. Centers, John W. Blanchard, Jan Conrad, Nataniel L. Figueroa, Antoine Garcon, Alexander V. Gramolin, Derek F. Jackson Kimball, Matthew Lawson, Bart Pelssers, Joseph A. Smiga, Alexander O. Sushkov, Arne Wickenbrock, Dmitry Budker, and Andrei Derevianko. Stochastic fluctuations of bosonic dark matter. *Nature Communications*, 12(1), dec 2021.

[54] Garv Chauhan, Shunsaku Horiuchi, Patrick Huber, and Ian M. Shoemaker. Low-Energy

Supernovae Bounds on Sterile Neutrinos. *arXiv*, 9 2023.

[55] Muping Chen, Graciela B. Gelmini, Philip Lu, and Volodymyr Takhistov. Primordial Black Hole Sterile Neutrinogenesis: Sterile Neutrino Dark Matter Production Independent of Couplings. *arXiv*, 12 2023.

[56] Yifan Chen, Yuxin Liu, Ru-Sen Lu, Yosuke Mizuno, Jing Shu, Xiao Xue, Qiang Yuan, and Yue Zhao. Stringent axion constraints with Event Horizon Telescope polarimetric measurements of M87*. *Nature Astron.*, 6(5):592–598, 2022.

[57] Carlos Chichiri, Graciela B. Gelmini, Philip Lu, and Volodymyr Takhistov. Cosmological dependence of sterile neutrino dark matter with self-interacting neutrinos. *Journal of Cosmology and Astroparticle Physics*, 2022(09):036, 2022.

[58] Gabriele Coppi, Giulia Conenna, Sofia Savorgnano, Felipe Carrero, Rolando Dünner-Planella, Nicholas Galitzki, Federico Nati, and Mario Zannoni. Protocalc: an artificial calibrator source for cmb telescopes, 2022.

[59] K. P. Coughlin, J. J. McMahon, K. T. Crowley, B. J. Koopman, K. H. Miller, S. M. Simon, and E. J. Wollack. Pushing the limits of broadband and high-frequency metamaterial silicon antireflection coatings. *Journal of Low Temperature Physics*, 193(5-6):876–885, May 2018.

[60] Kevin D. Crowley, Peter Dow, Jordan E. Shroyer, John C. Groh, Bradley Dober, Jacob Spisak, Nicholas Galitzki, Tanay Bhandarkar, Mark J. Devlin, and Simon Dicker et al. The Simons Observatory: A large-diameter truss for a refracting telescope cooled to 1 k. *Review of Scientific Instruments*, 93(5), May 2022.

[61] Neal Dalal and Andrey Kravtsov. Not so fuzzy: excluding fdm with sizes and stellar kinematics of ultra-faint dwarf galaxies, 2022.

[62] Basudeb Dasgupta and Joachim Kopp. Sterile Neutrinos. *Phys. Rept.*, 928:1–63, 2021.

[63] R. Datta, C. D. Munson, M. D. Niemack, J. J. McMahon, J. Britton, E. J. Wollack, J. Beall, M. J. Devlin, J. Fowler, P. Gallardo, J. Hubmayr, K. Irwin, L. Newburgh, J. P. Nibarger, L. Page, M. A. Quijada, B. L. Schmitt, S. T. Staggs, R. Thornton, and L. Zhang. Large-aperture wide-bandwidth antireflection-coated silicon lenses for millimeter wavelengths. *Applied Optics*, 52:8747, December 2013.

[64] André de Gouvêa. Neutrino Mass Models. *Ann. Rev. Nucl. Part. Sci.*, 66:197–217, 2016.

[65] André De Gouvêa, Manibrata Sen, Walter Tangarife, and Yue Zhang. Dodelson-Widrow Mechanism in the Presence of Self-Interacting Neutrinos. *Phys. Rev. Lett.*, 124(8):081802, 2020.

[66] Frank F. Deppisch, Wei Liu, and Manimala Mitra. Long-lived heavy neutrinos from higgs decays. *JHEP*, 2018(8), aug 2018.

[67] B. Dober, D. T. Becker, D. A. Bennett, S. A. Bryan, S. M. Duff, J. D. Gard, J. P. Hays-Wehle, G. C. Hilton, J. Hubmayr, J. A. B. Mates, C. D. Reintsema, L. R. Vale, and J. N. Ullom. Microwave squid multiplexer demonstration for cosmic microwave background imagers. *Applied Physics Letters*, 111(24):243510, 2017.

[68] Scott Dodelson and Lawrence M. Widrow. Sterile neutrinos as dark matter. *Physical Review Letters*, 72(1):17–20, jan 1994.

[69] A. D. Dolgov and S. H. Hansen. Massive sterile neutrinos as warm dark matter. *Astropart. Phys.*, 16:339–344, 2002.

[70] A. D. Dolgov, S. H. Hansen, G. Raffelt, and D. V. Semikoz. Heavy sterile neutrinos: Bounds from big bang nucleosynthesis and SN1987A. *Nucl. Phys. B*, 590:562–574, 2000.

[71] Leanne D Duffy and Karl van Bibber. Axions as dark matter particles. *New Journal of Physics*, 11(10):105008, oct 2009.

[72] Maximilian H. Abitbol et al.). The Simons Observatory: Astro2020 Decadal Project Whitepaper. *Bull. Am. Astron. Soc.*, 51:147, 2019.

[73] Ningfeng Zhu et al. The Simons Observatory Large Aperture Telescope Receiver. *Astrophys. J. Supp.*, 256(1):23, 2021.

[74] Michael A. Fedderke, Peter W. Graham, and Surjeet Rajendran. Axion dark matter detection with cmb polarization. *Phys. Rev. D*, 100:015040, Jul 2019.

[75] K. R. Ferguson, A. J. Anderson, N. Whitehorn, P. A. R. Ade, M. Archipley, J. S. Avva, L. Balkenhol, K. Benabed, A. N. Bender, B. A. Benson, F. Bianchini, L. E. Bleem, F. R. Bouchet, L. Bryant, E. Camphuis, J. E. Carlstrom, T. W. Cecil, C. L. Chang, P. Chaubal, P. M. Chichura, T.-L. Chou, T. M. Crawford, A. Cukierman, C. Daley, T. de Haan, K. R. Dibert, M. A. Dobbs, A. Doussot, D. Dutcher, W. Everett, C. Feng, A. Foster, S. Galli, A. E. Gambrel, R. W. Gardner, N. Goeckner-Wald, R. Gualtieri, F. Guidi, S. Guns, N. W. Halverson, E. Hivon, G. P. Holder, W. L. Holzapfel, J. C. Hood, N. Huang, L. Knox, M. Korman, C.-L. Kuo, A. T. Lee, A. E. Lowitz, C. Lu, M. Millea, J. Montgomery, T. Natoli, G. I. Noble, V. Novosad, Y. Omori, S. Padin, Z. Pan, P. Paschos, K. Prabhu, W. Quan, A. Rahlin, C. L. Reichardt, M. Rouble, J. E. Ruhl, E. Schiappucci, G. Smecher, J. A. Sobrin, J. Stephen, A. Suzuki, C. Tandoi, K. L. Thompson, B. Thorne, C. Tucker, C. Umilta, J. D. Vieira, G. Wang, W. L. K. Wu, V. Yefremenko, and M. R. Young. Searching for axionlike time-dependent cosmic birefringence with data from spt-3g. *Phys. Rev. D*, 106:042011, Aug 2022.

[76] D. J. Fixsen, E. S. Cheng, J. M. Gales, J. C. Mather, R. A. Shafer, and E. L. Wright. The Cosmic Microwave Background Spectrum from the Full COBE FIRAS Data Set. *apj*, 473:576, December 1996.

[77] Joshua W. Foster, Marius Kongsore, Christopher Dessert, Yujin Park, Nicholas L. Rodd, Kyle Cranmer, and Benjamin R. Safdi. Deep search for decaying dark matter with xmm-newton blank-sky observations. *Physical Review Letters*, 127(5), July 2021.

[78] Joshua W. Foster, Marius Kongsore, Christopher Dessert, Yujin Park, Nicholas L. Rodd, Kyle Cranmer, and Benjamin R. Safdi. Deep Search for Decaying Dark Matter with XMM-Newton Blank-Sky Observations. *Phys. Rev. Lett.*, 127(5):051101, 2021.

[79] Joshua W. Foster, Nicholas L. Rodd, and Benjamin R. Safdi. Revealing the dark matter halo with axion direct detection. *Physical Review D*, 97(12), jun 2018.

[80] Tomohiro Fujita, Ryo Tazaki, and Kenji Toma. Hunting axion dark matter with protoplanetary disk polarimetry. *Physical Review Letters*, 122(19), may 2019.

[81] George M. Fuller, Lukáš Gráf, Amol V. Patwardhan, and Jacob Spisak. Dark population transfer mechanism for sterile neutrino dark matter, 2024.

[82] George M. Fuller, Chad T. Kishimoto, and Alexander Kusenko. Heavy sterile neutrinos, entropy and relativistic energy production, and the relic neutrino background, 2011.

[83] George M. Fuller, Alexander Kusenko, and Kalliopi Petraki. Heavy sterile neutrinos and supernova explosions. *Phys. Lett. B*, 670:281–284, 2009.

[84] Nicholas Galitzki, Aamir Ali, Kam S. Arnold, Peter C. Ashton, Jason E. Austermann, Carlo Baccigalupi, Taylor Baildon, Darcy Barron, James A. Beall, Shawn Beckman, Sarah Marie M. Bruno, Sean Bryan, Paolo G. Calisse, Grace E. Chesmore, Yuji Chinone, Steve K. Choi, Gabriele Coppi, Kevin D. Crowley, Kevin T. Crowley, Ari Cukierman, Mark J. Devlin, Simon Dicker, Bradley Dober, Shannon M. Duff, Jo Dunkley, Giulio Fabbian, Patricio A. Gallardo, Martina Gerbino, Neil Goeckner-Wald, Joseph E. Golec, Jon E. Gudmundsson, Erin E. Healy, Shawn Henderson, Charles A. Hill, Gene C. Hilton, Shuay-Pwu Patty Ho, Logan A. Howe, Johannes Hubmayr, Oliver Jeong, Brian Keating, Brian J. Koopman, Kenji Kiuchi, Akito Kusaka, Jacob Lashner, Adrian T. Lee, Yaqiong Li, Michele Limon, Marius Lungu, Frederick Matsuda, Philip D. Mauskopf, Andrew J. May, Nialh McCallum, Jeff McMahon, Federico Nati, Michael D. Niemack, John L. Orlowski-Scherer, Stephen C. Parshley, Lucio Piccirillo, Mayuri Sathyanarayana Rao, Christopher Raum, Maria Salatino, Joseph S. Seibert, Carlos Sierra, Max Silva-Feaver, Sara M. Simon, Suzanne T. Staggs, Jason R. Stevens, Aritoki Suzuki, Grant Teply, Robert Thornton, Calvin Tsai, Joel N. Ullom, Eve M. Vavagiakis, Michael R. Vissers, Benjamin Westbrook, Edward J. Wollack, Zhilei Xu, and Ningfeng Zhu. The Simons Observatory: instrument overview. In Jonas Zmuidzinas and Jian-Rong Gao, editors, *Millimeter, Submillimeter,*

and Far-Infrared Detectors and Instrumentation for Astronomy IX, volume 10708, pages 1 – 13. International Society for Optics and Photonics, SPIE, 2018.

[85] Nicholas Galitzki, Tran Tsan, Jake Spisak, Michael Randall, Max Silva-Feaver, Joseph Seibert, Jacob Lashner, Shunsuke Adachi, Sean M. Adkins, Thomas Alford, Kam Arnold, Peter C. Ashton, Jason E. Austermann, Carlo Baccigalupi, Andrew Bazarko, James A. Beall, Sanah Bhimani, Bryce Bixler, Gabriele Coppi, Lance Corbett, Kevin D. Crowley, Kevin T. Crowley, Samuel Day-Weiss, Simon Dicker, Peter N. Dow, Cody J. Duell, Shannon M. Duff, Remington G. Gerras, John C. Groh, Jon E. Gudmundsson, Kathleen Harrington, Masaya Hasegawa, Erin Healy, Shawn W. Henderson, Johannes Hubmayr, Jeffrey Iuliano, Bradley R. Johnson, Brian Keating, Ben Keller, Kenji Kiuchi, Anna M. Kofman, Brian J. Koopman, Akito Kusaka, Adrian T. Lee, Richard A. Lew, Lawrence T. Lin, Michael J Link, Tammy J. Lucas, Marius Lungu, Aashrita Mangu, Jeffrey J McMahon, Amber D. Miller, Jenna E. Moore, Magdy Morshed, Hironobu Nakata, Federico Nati, Laura B. Newburgh, David V. Nguyen, Michael D. Niemack, Lyman A. Page, Kana Sakaguri, Yuki Sakurai, Mayuri Sathyanarayana Rao, Lauren J. Saunders, Jordan E. Shroyer, Junna Sugiyama, Osamu Tajima, Atsuto Takeuchi, Refilwe Tanah Bua, Grant Teply, Tomoki Terasaki, Joel N. Ullom, Jeffrey L. Van Lanen, Eve M. Vavagiakis, Michael R Vissers, Liam Walters, and Yuhan Wang. The simons observatory: Design, integration, and testing of the small aperture telescopes, 2024.

[86] Camilo Garcia-Cely and Xiaoyong Chu. Self-interacting dark matter as a solution to the problems in small-scale structures. In *52nd Rencontres de Moriond on EW Interactions and Unified Theories*, pages 307–314, 2017.

[87] Graciela B. Gelmini, Masahiro Kawasaki, Alexander Kusenko, Kai Murai, and Volodymyr Takhistov. Big Bang Nucleosynthesis constraints on sterile neutrino and lepton asymmetry of the Universe. *Journal of Cosmology and Astroparticle Physics*, 2020(09):051, 2020.

[88] Graciela B. Gelmini, Philip Lu, and Volodymyr Takhistov. Cosmological Dependence of Non-resonantly Produced Sterile Neutrinos. *Journal of Cosmology and Astroparticle Physics*, 2019(12):047, 2019.

[89] Graciela B. Gelmini, Philip Lu, and Volodymyr Takhistov. Cosmological Dependence of Resonantly Produced Sterile Neutrinos. *Journal of Cosmology and Astroparticle Physics*, 2020(06):008, 2020.

[90] Graciela B. Gelmini, Philip Lu, and Volodymyr Takhistov. Visible Sterile Neutrinos as the Earliest Relic Probes of Cosmology. *Phys. Lett. B*, 800:135113, 2020.

[91] J. Ghiglieri and M. Laine. Improved determination of sterile neutrino dark matter spectrum. *Journal of High Energy Physics*, 2015(11):171, 2015.

[92] J. Ghiglieri and M. Laine. Neutrino dynamics below the electroweak crossover. *Journal*

of Cosmology and Astroparticle Physics, 2016(07):015–015, jul 2016.

[93] Joseph E. Golec, Jeffrey J. McMahon, Aamire Ali, Simon Dicker, Nicholas Galitzki, Kathleen Harrington, Benjamin Westbrook, Edward J. Wollack, Zhilei Xu, and Ningfeng Zhu. Design and fabrication of metamaterial anti-reflection coatings for the Simons Observatory. In Ramón Navarro and Roland Geyl, editors, *Advances in Optical and Mechanical Technologies for Telescopes and Instrumentation IV*, volume 11451, pages 1182 – 1189. International Society for Optics and Photonics, SPIE, 2020.

[94] Alan H. Guth. Inflationary universe: A possible solution to the horizon and flatness problems. *Phys. Rev. D*, 23:347–356, Jan 1981.

[95] Rasmus S. L. Hansen and Stefan Vogl. Thermalizing sterile neutrino dark matter. *Phys. Rev. Lett.*, 119(25):251305, 2017.

[96] Diego Harari and Pierre Sikivie. Effects of a nambu-goldstone boson on the polarization of radio galaxies and the cosmic microwave background. *Physics Letters B*, 289(1):67–72, 1992.

[97] Kathleen Harrington, Rahul Datta, Keisuke Osumi, Aamir Ali, John W. Appel, Charles L. Bennett, Michael K. Brewer, Ricardo Bustos, Manwei Chan, David T. Chuss, Joseph Cleary, Jullianna Denes Couto, Sumit Dahal, Rolando Dünner, Joseph R. Eimer, Thomas Essinger-Hileman, Johannes Hubmayr, Francisco Raul Espinoza Inostroza, Jeffrey Iuliano, John Karakla, Yunyang Li, Tobias A. Marriage, Nathan J. Miller, Carolina Núñez, Ivan L. Padilla, Lucas Parker, Matthew A. Petroff, Bastian Pradenas Márquez, Rodrigo Reeves, Pedro Fluxá Rojas, Karwan Rostem, Deniz Augusto Nunes Valle, Duncan J. Watts, Janet L. Weiland, Edward J. Wollack, and Zhilei Xu. Two Year Cosmology Large Angular Scale Surveyor (CLASS) Observations: Long Timescale Stability Achieved with a Front-End Variable-delay Polarization Modulator at 40 GHz. *arXiv e-prints*, page arXiv:2101.00034, December 2020.

[98] Fiona A. Harrison et al. The Nuclear Spectroscopic Telescope Array (NuSTAR) High-energy X-Ray Mission. *The Astrophysical Journal*, 770(2):103, June 2013.

[99] Shawn W. Henderson, Zeeshan Ahmed, Jason Austermann, Daniel Becker, Douglas A. Bennett, David Brown, Saptarshi Chaudhuri, Hsiao-Mei Sherry Cho, John M. D'Ewart, Bradley Dober, Shannon M. Duff, John E. Dusatko, Sofia Fatigoni, Josef C. Frisch, Jonathon D. Gard, Mark Halpern, Gene C. Hilton, Johannes Hubmayr, Kent D. Irwin, Ethan D. Karpel, Sarah S. Kernasovskiy, Stephen E. Kuenstner, Chao-Lin Kuo, Dale Li, John A. B. Mates, Carl D. Reintsema, Stephen R. Smith, Joel Ullom, Leila R. Vale, Daniel D. Van Winkle, Michael Vissers, and Cyndia Yu. Highly-multiplexed microwave SQUID readout using the SLAC Microresonator Radio Frequency (SMuRF) electronics for future CMB and sub-millimeter surveys. In Jonas Zmuidzinas and Jian-Rong Gao, editors, *Millimeter, Submillimeter, and Far-Infrared Detectors and Instrumentation for*

Astronomy IX, volume 10708 of *Society of Photo-Optical Instrumentation Engineers (SPIE) Conference Series*, page 1070819, July 2018.

[100] Johannes Herms, Alejandro Ibarra, and Takashi Toma. A new mechanism of sterile neutrino dark matter production. *Journal of Cosmology and Astroparticle Physics*, 2018(06):036, 2018.

[101] Jun Hidaka and George M. Fuller. Dark matter sterile neutrinos in stellar collapse: Alteration of energy/lepton number transport and a mechanism for supernova explosion enhancement. *Phys. Rev. D*, 74:125015, 2006.

[102] Jun Hidaka and George M. Fuller. Sterile Neutrino-Enhanced Supernova Explosions. *Phys. Rev. D*, 76:083516, 2007.

[103] C. A. Hill, A. Kusaka, P. Ashton, P. Barton, T. Adkins, K. Arnold, B. Bixler, S. Ganjam, A. T. Lee, F. Matsuda, T. Matsumura, Y. Sakurai, R. Tat, and Y. Zhou. A cryogenic continuously rotating half-wave plate mechanism for the POLARBEAR-2b cosmic microwave background receiver. *Review of Scientific Instruments*, 91(12):124503, December 2020.

[104] Charles A. Hill, Sarah Marie M. Bruno, Sara M. Simon, Aamir Ali, Kam S. Arnold, Peter C. Ashton, Darcy Barron, Sean Bryan, Yuji Chinone, Gabriele Coppi, Kevin T. Crowley, Ari Cukierman, Simon Dicker, Jo Dunkley, Giulio Fabbian, Nicholas Galitzki, Patricio A. Gallardo, Jon E. Gudmundsson, Johannes Hubmayr, Brian Keating, Akito Kusaka, Adrian T. Lee, Frederick Matsuda, Philip D. Mauskopf, Jeffrey McMahon, Michael D. Niemack, Giuseppe Puglisi, Mayuri Sathyanarayana Rao, Maria Salatino, Carlos Sierra, Suzanne Staggs, Aritoki Suzuki, Grant Teply, Joel N. Ullom, Benjamin Westbrook, Zhilei Xu, and Ningfeng Zhu. BoloCalc: a sensitivity calculator for the design of Simons Observatory. In Jonas Zmuidzinas and Jian-Rong Gao, editors, *Millimeter, Submillimeter, and Far-Infrared Detectors and Instrumentation for Astronomy IX*, volume 10708, pages 698 – 718. International Society for Optics and Photonics, SPIE, 2018.

[105] René e Hlozek, Daniel Grin, David J. E. Marsh, and Pedro G. Ferreira. A search for ultralight axions using precision cosmological data. *Physical Review D*, 91(10), may 2015.

[106] René e Hložek, David J E Marsh, and Daniel Grin. Using the full power of the cosmic microwave background to probe axion dark matter. *Monthly Notices of the Royal Astronomical Society*, 476(3):3063–3085, feb 2018.

[107] F. Hofmann, J. S. Sanders, K. Nandra, N. Clerc, and M. Gaspari. 7.1 keV sterile neutrino constraints from X-ray observations of 33 clusters of galaxies with Chandra ACIS. *Astron. Astrophys.*, 592:A112, 2016.

[108] F. Hofmann and C. Wegg. 7.1 keV sterile neutrino dark matter constraints from a deep

Chandra X-ray observation of the Galactic bulge Limiting Window. *Astron. Astrophys.*, 625:L7, 2019.

[109] Shunsaku Horiuchi, Philip J. Humphrey, Jose Onorbe, Kevork N. Abazajian, Manoj Kaplinghat, and Shea Garrison-Kimmel. Sterile neutrino dark matter bounds from galaxies of the Local Group. *Phys. Rev. D*, 89(2):025017, 2014.

[110] Emma L. Horner, Francisco Mungia Wulftange, Isabella A. Ianora, and Chad T. Kishimoto. Exploring resonantly produced mixed sterile neutrino dark matter models. *Phys. Rev. D*, 108(8):083503, 2023.

[111] Wayne Hu, Rennan Barkana, and Andrei Gruzinov. Fuzzy cold dark matter: The wave properties of ultralight particles. *Physical Review Letters*, 85(6):1158–1161, aug 2000.

[112] Zachary B. Huber, Yaqiong Li, Eve M. Vavagiakis, Steve K. Choi, Nicholas F. Cothard, Cody J. Duell, Nicholas Galitzki, Erin Healy, Johannes Hubmayr, R. Johnson, Bradley, Benjamin Keller, Heather McCarrick, Michael D. Niemack, Yuhan Wang, Zhilei Xu, and Kaiwen Zheng. The Simons Observatory: Magnetic Shielding Measurements for the Universal Multiplexing Module. *Submitted to JLTP*, 2021.

[113] Lam Hui. Wave Dark Matter. *Ann. Rev. Astron. Astrophys.*, 59:247–289, 2021.

[114] Lam Hui, Jeremiah P. Ostriker, Scott Tremaine, and Edward Witten. Ultralight scalars as cosmological dark matter. *Physical Review D*, 95(4), feb 2017.

[115] Igor G. Irastorza and Javier Redondo. New experimental approaches in the search for axion-like particles. *Progress in Particle and Nuclear Physics*, 102:89–159, sep 2018.

[116] Vid Iršič, Matteo Viel, Martin G. Haehnelt, James S. Bolton, and George D. Becker. First constraints on fuzzy dark matter from lyman-α forest data and hydrodynamical simulations. *Phys. Rev. Lett.*, 119:031302, Jul 2017.

[117] M.M. Ivanov, Y.Y. Kovalev, M.L. Lister, A.G. Panin, A.B. Pushkarev, T. Savolainen, and S.V. Troitsky. Constraining the photon coupling of ultra-light dark-matter axion-like particles by polarization variations of parsec-scale jets in active galaxies. *Journal of Cosmology and Astroparticle Physics*, 2019(02):059–059, feb 2019.

[118] Lucas Johns and George M. Fuller. Self-interacting sterile neutrino dark matter: the heavy-mediator case. *Phys. Rev. D*, 100(2):023533, 2019.

[119] Yonatan Kahn, Benjamin R. Safdi, and Jesse Thaler. Broadband and resonant approaches to axion dark matter detection. *Physical Review Letters*, 117(14), sep 2016.

[120] Brian G. Keating, Meir Shimon, and Amit P. S. Yadav. Self-calibration of cosmic

microwave background polarization experiments. *The Astrophysical Journal*, 762(2):L23, Dec 2012.

[121] Zigmund D. Kermish, Peter Ade, Aubra Anthony, Kam Arnold, Darcy Barron, David Boettger, Julian Borrill, Scott Chapman, Yuji Chinone, Matt A. Dobbs, Josquin Errard, Giulio Fabbian, Daniel Flanigan, George Fuller, Adnan Ghribi, Will Grainger, Nils Halverson, Masaya Hasegawa, Kaori Hattori, Masashi Hazumi, William L. Holzapfel, Jacob Howard, Peter Hyland, Andrew Jaffe, Brian Keating, Theodore Kisner, Adrian T. Lee, Maude Le Jeune, Eric Linder, Marius Lungu, Frederick Matsuda, Tomotake Matsumura, Xiaofan Meng, Nathan J. Miller, Hideki Morii, Stephanie Moyerman, Mike J. Myers, Haruki Nishino, Hans Paar, Erin Quealy, Christian L. Reichardt, Paul L. Richards, Colin Ross, Akie Shimizu, Meir Shimon, Chase Shimmin, Mike Sholl, Praween Siritanasak, Helmuth Spieler, Nathan Stebor, Bryan Steinbach, Radek Stompor, Aritoki Suzuki, Takayuki Tomaru, Carole Tucker, and Oliver Zahn. The POLARBEAR experiment. In Wayne S. Holland and Jonas Zmuidzinas, editors, *Millimeter, Submillimeter, and Far-Infrared Detectors and Instrumentation for Astronomy VI*, volume 8452 of *Society of Photo-Optical Instrumentation Engineers (SPIE) Conference Series*, page 84521C, September 2012.

[122] Chad T. Kishimoto and George M. Fuller. Lepton Number-Driven Sterile Neutrino Production in the Early Universe. *Phys. Rev. D*, 78:023524, 2008.

[123] Chad T. Kishimoto, George M. Fuller, and Christel J. Smith. Coherent Active-Sterile Neutrino Flavor Transformation in the Early Universe. *Phys. Rev. Lett.*, 97:141301, 2006.

[124] Kenji Kiuchi, Shunsuke Adachi, Aamir M. Ali, Kam Arnold, Peter Ashton, Jason E. Austermann, Andrew Bazako, James A. Beall, Yuji Chinone, Gabriele Coppi, Kevin D. Crowley, Kevin T. Crowley, Simon Dicker, Bradley Dober, Shannon M. Duff, Giulio Fabbian, Nicholas Galitzki, Joseph E. Golec, Jon E. Gudmundsson, Kathleen Harrington, Masaya Hasegawa, Makoto Hattori, Charles A. Hill, Shuay-Pwu Patty Ho, Johannes Hubmayr, Bradley R. Johnson, Daisuke Kaneko, Nobuhiko Katayama, Brian Keating, Akito Kusaka, Jack Lashner, Adrian T. Lee, Frederick Matsuda, Heather McCarrick, Masaaki Murata, Federico Nati, Yume Nishinomiya, Lyman Page, Mayuri Sathyanarayana Rao, Christian L. Reichardt, Kana Sakaguri, Yuki Sakurai, Joseph Sibert, Jacob Spisak, Osamu Tajima, Grant P. Teply, Tomoki Terasaki, Tran Tsan, Samantha Walker, Edward J. Wollack, Zhilei Xu, Kyohei Yamada, Mario Zannoni, and Ningfeng Zhu. Simons Observatory Small Aperture Telescope overview. In *Society of Photo-Optical Instrumentation Engineers (SPIE) Conference Series*, volume 11445 of *Society of Photo-Optical Instrumentation Engineers (SPIE) Conference Series*, page 114457L, December 2020.

[125] Brian J. Koopman, Jack Lashner, Lauren J. Saunders, Matthew Hasselfield, Tanay Bhandarkar, Sanah Bhimani, Steve K. Choi, Cody J. Duell, Nicholas Galitzki, Kathleen Harrington, Adam D. Hincks, Shuay-Pwu Patty Ho, Laura Newburgh, Christian L. Reichardt, Joseph Seibert, Jacob Spisak, Benjamin Westbrook, Zhilei Xu, and Ningfeng Zhu. The Simons Observatory: overview of data acquisition, control, monitoring, and

computer infrastructure. In Juan C. Guzman and Jorge Ibsen, editors, *Software and Cyberinfrastructure for Astronomy VI*, volume 11452, pages 35 – 53. International Society for Optics and Photonics, SPIE, 2020.

[126] Alexander Kusenko. Sterile neutrinos: The Dark side of the light fermions. *Phys. Rept.*, 481:1–28, 2009.

[127] Tao Liu, George Smoot, and Yue Zhao. Detecting axionlike dark matter with linearly polarized pulsar light. *Physical Review D*, 101(6), mar 2020.

[128] Michael Loewenstein, Alexander Kusenko, and Peter L. Biermann. New Limits on Sterile Neutrinos from Suzaku Observations of the Ursa Minor Dwarf Spheroidal Galaxy. *Astrophys. J.*, 700:426–435, 2009.

[129] Kristin K. Madsen, Javier A. García, Daniel Stern, Rashied Armini, Stefano Basso, Diogo Coutinho, Brian W. Grefenstette, Steven Kenyon, Alberto Moretti, Patrick Morrisey, Kirpal Nandra, Giovanni Pareschi, Peter Predehl, Arne Rau, Daniele Spiga, Jörn Willms, and William W. Zhang. The high energy x-ray probe (hex-p): Instrument and mission profile, 2023.

[130] David J.E. Marsh. Axion cosmology. *Physics Reports*, 643:1–79, jul 2016.

[131] C. J. Martoff et al. HUNTER: precision massive-neutrino search based on a laser cooled atomic source. *Quantum Sci. Technol.*, 6(2):024008, 2021.

[132] Nick E. Mavromatos, Carlos R. Argüelles, Remo Ruffini, and Jorge A. Rueda. Self-interacting dark matter. In *14th Marcel Grossmann Meeting on Recent Developments in Theoretical and Experimental General Relativity, Astrophysics, and Relativistic Field Theories*, volume 1, pages 639–666, 2017.

[133] Heather McCarrick, Zachary Atkins, Jason Austermann, Tanay Bhandarkar, Steve K. Choi, Cody J. Duell, Shannon M. Duff, Daniel Dutcher, Nicholas Galitzki, Erin Healy, Zachary B. Huber, Johannes Hubmayr, R. Johnson, Bradley, Michael D. Niemack, Joseph Seibert, Rita F. Sonka, Suzanne T. Staggs, Eve M. Vavagiakis, Yuhan Wang, Zhilei Xu, Kaiwen Zheng, and Ningfeng Zhu. The 90 and 150 GHz universal focal-plane modules for theSimons Observatory. *Submitted to JLTP*, 2021.

[134] Heather McCarrick, Erin Healy, Zeeshan Ahmed, Kam Arnold, Zachary Atkins, Jason E. Austermann, Tanay Bhandarkar, Jim A. Beall, Sarah Marie Bruno, Steve K. Choi, Jake Connors, Nicholas F. Cothard, Kevin D. Crowley, Simon Dicker, Bradley Dober, Cody J. Duell, Shannon M. Duff, Daniel Dutcher, Josef C. Frisch, Nicholas Galitzki, Megan B. Gralla, Jon E. Gudmundsson, Shawn W. Henderson, Gene C. Hilton, Shuay-Pwu Patty Ho, Zachary B. Huber, Johannes Hubmayr, Jeffrey Iuliano, Bradley R. Johnson, Anna M. Kofman, Akito Kusaka, Jack Lashner, Adrian T. Lee, Yaqiong Li, Michael J. Link, Tammy J.

Lucas, Marius Lungu, J. A. B. Mates, Jeffrey J. McMahon, Michael D. Niemack, John Orlowski-Scherer, Joseph Seibert, Maximiliano Silva-Feaver, Sara M. Simon, Suzanne Staggs, Aritoki Suzuki, Tomoki Terasaki, Joel N. Ullom, Eve M. Vavagiakis, Leila R. Vale, Jeff Van Lanen, Michael R. Vissers, Yuhan Wang, Edward J. Wollack, Zhilei Xu, Edward Young, Cyndia Yu, Kaiwen Zheng, and Ningfeng Zhu. The Simons Observatory microwave SQUID multiplexing detector module design. *arXiv e-prints*, page arXiv:2106.14797, June 2021.

[135] Alexander Merle, Viviana Niro, and Daniel Schmidt. New Production Mechanism for keV Sterile Neutrino Dark Matter by Decays of Frozen-In Scalars. *Journal of Cosmology and Astroparticle Physics*, 2014(03):028, 2014.

[136] Susanne Mertens et al. A novel detector system for KATRIN to search for keV-scale sterile neutrinos. *J. Phys. G*, 46(6):065203, 2019.

[137] Yuto Minami and Eiichiro Komatsu. New extraction of the cosmic birefringence from the planck 2018 polarization data. *Physical Review Letters*, 125(22), November 2020.

[138] B. Moore. Evidence against dissipationless dark matter from observations of galaxy haloes. *Nature*, 370:629, 1994.

[139] Masaaki Murata, Hironobu Nakata, Kengo Iijima, Shunsuke Adachi, Yudai Seino, Kenji Kiuchi, Frederick Matsuda, Michael J. Randall, Kam Arnold, Nicholas Galitzki, Bradley R. Johnson, Brian Keating, Akito Kusaka, John B. Lloyd, Joseph Seibert, Maximiliano Silva-Feaver, Osamu Tajima, Tomoki Terasaki, and Kyohei Yamada. The Simons Observatory: A fully remote controlled calibration system with a sparse wire grid for cosmic microwave background telescopes. *arXiv e-prints*, page arXiv:2309.02035, September 2023.

[140] E. O. Nadler et al. Milky Way Satellite Census. III. Constraints on Dark Matter Properties from Observations of Milky Way Satellite Galaxies. *Phys. Rev. Lett.*, 126:091101, 2021.

[141] Ethan O. Nadler, Simon Birrer, Daniel Gilman, Risa H. Wechsler, Xiaolong Du, Andrew Benson, Anna M. Nierenberg, and Tommaso Treu. Dark matter constraints from a unified analysis of strong gravitational lenses and milky way satellite galaxies. *The Astrophysical Journal*, 917(1):7, aug 2021.

[142] Toshiya Namikawa, Yilun Guan, Omar Darwish, Blake D. Sherwin, Simone Aiola, Nicholas Battaglia, James A. Beall, Daniel T. Becker, J. Richard Bond, Erminia Calabrese, Grace E. Chesmore, Steve K. Choi, Mark J. Devlin, Joanna Dunkley, Rolando Dünner, Anna E. Fox, Patricio A. Gallardo, Vera Gluscevic, Dongwon Han, Matthew Hasselfield, Gene C. Hilton, Adam D. Hincks, Renée Hložek, Johannes Hubmayr, Kevin Huffenberger, John P. Hughes, Brian J. Koopman, Arthur Kosowsky, Thibaut Louis, Marius Lungu, Amanda MacInnis, Mathew S. Madhavacheril, Maya Mallaby-Kay, Loïc Maurin, Jeffrey McMahon, Kavilan Moodley, Sigurd Naess, Federico Nati, Laura B. Newburgh,

John P. Nibarger, Michael D. Niemack, Lyman A. Page, Frank J. Qu, Naomi Robertson, Alessandro Schillaci, Neelima Sehgal, Cristóbal Sifón, Sara M. Simon, David N. Spergel, Suzanne T. Staggs, Emilie R. Storer, Alexander van Engelen, Jeff van Lanen, and Edward J. Wollack. Atacama cosmology telescope: Constraints on cosmic birefringence. *Phys. Rev. D*, 101:083527, Apr 2020.

[143] Kirpal Nandra et al. The hot and energetic universe: A white paper presenting the science theme motivating the athena+ mission, 2013.

[144] Federico Nati, Mark J. Devlin, Martina Gerbino, Bradley R. Johnson, Brian Keating, Luca Pagano, and Grant Teply. Polocalc: A novel method to measure the absolute polarization orientation of the cosmic microwave background. *Journal of Astronomical Instrumentation*, 06(02), May 2017.

[145] Kenny C. Y. Ng, Shunsaku Horiuchi, Jennifer M. Gaskins, Miles Smith, and Robert Preece. Improved Limits on Sterile Neutrino Dark Matter using Full-Sky Fermi Gamma-Ray Burst Monitor Data. *Phys. Rev. D*, 92(4):043503, 2015.

[146] Kenny C. Y. Ng, Brandon M. Roach, Kerstin Perez, John F. Beacom, Shunsaku Horiuchi, Roman Krivonos, and Daniel R. Wik. New Constraints on Sterile Neutrino Dark Matter from *NuSTAR* M31 Observations. *Phys. Rev. D*, 99:083005, 2019.

[147] Dirk Notzold and Georg Raffelt. Neutrino Dispersion at Finite Temperature and Density. *Nucl. Phys. B*, 307:924–936, 1988.

[148] Se-Heon Oh, W. J. G. de Blok, Fabian Walter, Elias Brinks, and Robert C. Kennicutt, Jr. High-resolution dark matter density profiles of THINGS dwarf galaxies: Correcting for non-circular motions. *Astron. J.*, 136:2761, 2008.

[149] Se-Heon Oh et al. High-resolution mass models of dwarf galaxies from LITTLE THINGS. *Astron. J.*, 149:180, 2015.

[150] Palash B. Pal and Lincoln Wolfenstein. Radiative Decays of Massive Neutrinos. *Phys. Rev. D*, 25:766, 1982.

[151] Amol V. Patwardhan, George M. Fuller, Chad T. Kishimoto, and Alexander Kusenko. Diluted equilibrium sterile neutrino dark matter. *Phys. Rev. D*, 92(10):103509, 2015.

[152] Alexandre Payez, Carmelo Evoli, Tobias Fischer, Maurizio Giannotti, Alessandro Mirizzi, and Andreas Ringwald. Revisiting the SN1987a gamma-ray limit on ultralight axion-like particles. *Journal of Cosmology and Astroparticle Physics*, 2015(02):006–006, feb 2015.

[153] R. D. Peccei and Helen R. Quinn. Constraints imposed by CP conservation in the presence of pseudoparticles. *Phys. Rev. D*, 16:1791–1797, Sep 1977.

[154] R. D. Peccei and Helen R. Quinn. CP conservation in the presence of pseudoparticles. *Phys. Rev. Lett.*, 38:1440–1443, Jun 1977.

[155] A. A. Penzias and R. W. Wilson. A Measurement of Excess Antenna Temperature at 4080 Mc/s. *The Astrophysical Journal*, 142:419–421, July 1965.

[156] Kerstin Perez, Kenny C. Y. Ng, John F. Beacom, Cora Hersh, Shunsaku Horiuchi, and Roman Krivonos. Almost closing the νMSM sterile neutrino dark matter window with NuSTAR. *Phys. Rev. D*, 95(12):123002, 2017.

[157] Kalliopi Petraki and Alexander Kusenko. Dark-matter sterile neutrinos in models with a gauge singlet in the Higgs sector. *Phys. Rev. D*, 77:065014, 2008.

[158] C. Quimbay and S. Vargas-Castrillón. Fermionic dispersion relations in the standard model at finite temperature. *Nuclear Physics B*, 451(1-2):265–302, sep 1995.

[159] Hannah Rasmussen, Alex McNichol, George M. Fuller, and Chad T. Kishimoto. Effects of an intermediate mass sterile neutrino population on the early Universe. *Phys. Rev. D*, 105(8):083513, 2022.

[160] Anupam Ray and Yong-Zhong Qian. Evolution of tau-neutrino lepton number in protoneutron stars due to active-sterile neutrino mixing. *Phys. Rev. D*, 108(6):063025, 2023.

[161] Britt Reichborn-Kjennerud, Asad M. Aboobaker, Peter Ade, François Aubin, Carlo Baccigalupi, Chaoyun Bao, Julian Borrill, Christopher Cantalupo, Daniel Chapman, Joy Didier, Matt Dobbs, Julien Grain, William Grainger, Shaul Hanany, Seth Hillbrand, Johannes Hubmayr, Andrew Jaffe, Bradley Johnson, Terry Jones, Theodore Kisner, Jeff Klein, Andrei Korotkov, Sam Leach, Adrian Lee, Lorne Levinson, Michele Limon, Kevin MacDermid, Tomotake Matsumura, Xiaofan Meng, Amber Miller, Michael Milligan, Enzo Pascale, Daniel Polsgrove, Nicolas Ponthieu, Kate Raach, Ilan Sagiv, Graeme Smecher, Federico Stivoli, Radek Stompor, Huan Tran, Matthieu Tristram, Gregory S. Tucker, Yury Vinokurov, Amit Yadav, Matias Zaldarriaga, and Kyle Zilic. EBEX: a balloon-borne CMB polarization experiment. In Wayne S. Holland and Jonas Zmuidzinas, editors, *Millimeter, Submillimeter, and Far-Infrared Detectors and Instrumentation for Astronomy V*, volume 7741 of *Society of Photo-Optical Instrumentation Engineers (SPIE) Conference Series*, page 77411C, July 2010.

[162] S. Riemer-Sørensen et al. Dark matter line emission constraints from NuSTAR observations of the Bullet Cluster. *Astrophys. J.*, 810(1):48, 2015.

[163] Signe Riemer-Sørensen, Steen H. Hansen, and Kristian Pedersen. Sterile neutrinos in the Milky Way: Observational constraints. *Astrophys. J. Lett.*, 644:L33–L36, 2006.

[164] Brandon M. Roach, Kenny C. Y. Ng, Kerstin Perez, John F. Beacom, Shunsaku Horiuchi,

Roman Krivonos, and Daniel R. Wik. NuSTAR Tests of Sterile-Neutrino Dark Matter: New Galactic Bulge Observations and Combined Impact. *Phys. Rev. D*, 101(10):103011, 2020.

[165] Brandon M. Roach, Steven Rossland, Kenny C. Y. Ng, Kerstin Perez, John F. Beacom, Brian W. Grefenstette, Shunsaku Horiuchi, Roman Krivonos, and Daniel R. Wik. Long-exposure nustar constraints on decaying dark matter in the galactic halo. *Physical Review D*, 107(2), January 2023.

[166] Brandon M. Roach, Steven Rossland, Kenny C. Y. Ng, Kerstin Perez, John F. Beacom, Brian W. Grefenstette, Shunsaku Horiuchi, Roman Krivonos, and Daniel R. Wik. Long-exposure NuSTAR constraints on decaying dark matter in the Galactic halo. *Phys. Rev. D*, 107(2):023009, 2023.

[167] Miguel Rocha, Annika H. G. Peter, James S. Bullock, Manoj Kaplinghat, Shea Garrison-Kimmel, Jose Onorbe, and Leonidas A. Moustakas. Cosmological Simulations with Self-Interacting Dark Matter I: Constant Density Cores and Substructure. *Mon. Not. Roy. Astron. Soc.*, 430:81–104, 2013.

[168] Keir K. Rogers and Hiranya V. Peiris. Strong bound on canonical ultralight axion dark matter from the lyman-alpha forest. *Physical Review Letters*, 126(7), feb 2021.

[169] POLARBEAR Collaboration, P. A. R. Ade, M. Aguilar, Y. Akiba, K. Arnold, C. Baccigalupi, D. Barron, D. Beck, F. Bianchini, D. Boettger, J. Borrill, S. Chapman, Y. Chinone, K. Crowley, A. Cukierman, R. Dünner, M. Dobbs, A. Ducout, T. Elleflot, J. Errard, G. Fabbian, S. M. Feeney, C. Feng, T. Fujino, N. Galitzki, A. Gilbert, N. Goeckner-Wald, J. C. Groh, G. Hall, N. Halverson, T. Hamada, M. Hasegawa, M. Hazumi, C. A. Hill, L. Howe, Y. Inoue, G. Jaehnig, A. H. Jaffe, O. Jeong, D. Kaneko, N. Katayama, B. Keating, R. Keskitalo, T. Kisner, N. Krachmalnicoff, A. Kusaka, M. Le Jeune, A. T. Lee, E. M. Leitch, D. Leon, E. Linder, L. Lowry, F. Matsuda, T. Matsumura, Y. Minami, J. Montgomery, M. Navaroli, H. Nishino, H. Paar, J. Peloton, A. T. P. Pham, D. Poletti, G. Puglisi, C. L. Reichardt, P. L. Richards, C. Ross, Y. Segawa, B. D. Sherwin, M. Silva-Feaver, P. Siritanasak, N. Stebor, R. Stompor, A. Suzuki, O. Tajima, S. Takakura, S. Takatori, D. Tanabe, G. P. Teply, T. Tomaru, C. Tucker, N. Whitehorn, and A. Zahn. A Measurement of the Cosmic Microwave Background B-mode Polarization Power Spectrum at Subdegree Scales from Two Years of POLARBEAR Data. *The Astrophysical Journal*, 848(2):121, October 2017.

[170] POLARBEAR Collaboration, P. A. R. Ade, Y. Akiba, A. E. Anthony, K. Arnold, M. Atlas, D. Barron, D. Boettger, J. Borrill, S. Chapman, Y. Chinone, M. Dobbs, T. Elleflot, J. Errard, G. Fabbian, C. Feng, D. Flanigan, A. Gilbert, W. Grainger, N. W. Halverson, M. Hasegawa, K. Hattori, M. Hazumi, W. L. Holzapfel, Y. Hori, J. Howard, P. Hyland, Y. Inoue, G. C. Jaehnig, A. H. Jaffe, B. Keating, Z. Kermish, R. Keskitalo, T. Kisner, M. Le Jeune, A. T. Lee, E. M. Leitch, E. Linder, M. Lungu, F. Matsuda, T. Matsumura,

X. Meng, N. J. Miller, H. Morii, S. Moyerman, M. J. Myers, M. Navaroli, H. Nishino, A. Orlando, H. Paar, J. Peloton, D. Poletti, E. Quealy, G. Rebeiz, C. L. Reichardt, P. L. Richards, C. Ross, I. Schanning, D. E. Schenck, B. D. Sherwin, A. Shimizu, C. Shimmin, M. Shimon, P. Siritanasak, G. Smecher, H. Spieler, N. Stebor, B. Steinbach, R. Stompor, A. Suzuki, S. Takakura, T. Tomaru, B. Wilson, A. Yadav, and O. Zahn. A Measurement of the Cosmic Microwave Background B-mode Polarization Power Spectrum at Sub-degree Scales with POLARBEAR. *The Astrophysical Journal*, 794(2):171, October 2014.

[171] Mikhail Shaposhnikov. The nuMSM, leptonic asymmetries, and properties of singlet fermions. *Journal of High Energy Physics*, 2008(08):008, 2008.

[172] Mikhail Shaposhnikov and Igor Tkachev. The nuMSM, inflation, and dark matter. *Phys. Lett. B*, 639:414–417, 2006.

[173] Xiang-Dong Shi and George M. Fuller. A New dark matter candidate: Nonthermal sterile neutrinos. *Phys. Rev. Lett.*, 82:2832–2835, 1999.

[174] Meir Shimon, Brian Keating, Nicolas Ponthieu, and Eric Hivon. CMB polarization systematics due to beam asymmetry: Impact on inflationary science. *Physical Review D*, 77(8), apr 2008.

[175] Brian Shuve and Itay Yavin. Dark matter progenitor: Light vector boson decay into sterile neutrinos. *Phys. Rev. D*, 89(11):113004, 2014.

[176] S. M. Simon, J. W. Appel, L. E. Campusano, S. K. Choi, K. T. Crowley, T. Essinger-Hileman, P. Gallardo, S. P. Ho, A. Kusaka, F. Nati, G. A. Palma, L. A. Page, S. Raghunathan, and S. T. Staggs. Characterizing Atacama B-mode Search Detectors with a Half-Wave Plate. *Journal of Low Temperature Physics*, 184(3-4):534–539, August 2016.

[177] Júlia Sisk-Reynés, James H Matthews, Christopher S Reynolds, Helen R Russell, Robyn N Smith, and M C David Marsh. New constraints on light axion-like particles using Chandra transmission grating spectroscopy of the powerful cluster-hosted quasar H1821+643. *Monthly Notices of the Royal Astronomical Society*, 510(1):1264–1277, 12 2021.

[178] Kendrick M. Smith. Pseudo-C_ℓ estimators which do not mix e and b modes. *Phys. Rev. D*, 74:083002, Oct 2006.

[179] David N. Spergel and Paul J. Steinhardt. Observational evidence for selfinteracting cold dark matter. *Phys. Rev. Lett.*, 84:3760–3763, 2000.

[180] Jacob Spisak, Edison Liang, Wen Fu, and Markus Boettcher. Relativistic shear boundary layer and the gamma-ray emission of GW170817. *The Astrophysical Journal*, 903(2):120, Nov 2020.

[181] Jason R. Stevens, Nicholas F. Cothard, Eve M. Vavagiakis, Aamir Ali, Kam Arnold, Jason E. Austermann, Steve K. Choi, Bradley J. Dober, Cody Duell, Shannon M. Duff, Gene C. Hilton, Shuay-Pwu Patty Ho, Thuong D. Hoang, Johannes Hubmayr, Adrian T. Lee, Aashrita Mangu, Federico Nati, Michael D. Niemack, Christopher Raum, Mario Renzullo, Maria Salatino, Trevor Sasse, Sara M. Simon, Suzanne Staggs, Aritoki Suzuki, Patrick Truitt, Joel Ullom, John Vivalda, Michael R. Vissers, Samantha Walker, Benjamin Westbrook, Edward J. Wollack, Zhilei Xu, and Daniel Yohannes. Characterization of Transition Edge Sensors for the Simons Observatory. *Journal of Low Temperature Physics*, 199(3-4):672–680, February 2020.

[182] Anna M. Suliga, Irene Tamborra, and Meng-Ru Wu. Lifting the core-collapse supernova bounds on keV-mass sterile neutrinos. *Journal of Cosmology and Astroparticle Physics*, 2020(08):018, 2020.

[183] A. Suzuki, P. Ade, Y. Akiba, C. Aleman, K. Arnold, C. Baccigalupi, B. Barch, D. Barron, A. Bender, D. Boettger, J. Borrill, S. Chapman, Y. Chinone, A. Cukierman, M. Dobbs, A. Ducout, R. Dunner, T. Elleflot, J. Errard, G. Fabbian, S. Feeney, C. Feng, T. Fujino, G. Fuller, A. Gilbert, N. Goeckner-Wald, J. Groh, T. De Haan, G. Hall, N. Halverson, T. Hamada, M. Hasegawa, K. Hattori, M. Hazumi, C. Hill, W. Holzapfel, Y. Hori, L. Howe, Y. Inoue, F. Irie, G. Jaehnig, A. Jaffe, O. Jeong, N. Katayama, J. Kaufman, K. Kazemzadeh, B. Keating, Z. Kermish, R. Keskitalo, T. Kisner, A. Kusaka, M. Le Jeune, A. Lee, D. Leon, E. Linder, L. Lowry, F. Matsuda, T. Matsumura, N. Miller, K. Mizukami, J. Montgomery, M. Navaroli, H. Nishino, J. Peloton, D. Poletti, G. Puglisi, G. Rebeiz, C. Raum, C. Reichardt, P. Richards, C. Ross, K. Rotermund, Y. Segawa, B. Sherwin, I. Shirley, P. Siritanasak, N. Stebor, R. Stompor, J. Suzuki, O. Tajima, S. Takada, S. Takakura, S. Takatori, A. Tikhomirov, T. Tomaru, B. Westbrook, N. Whitehorn, T. Yamashita, A. Zahn, and O. Zahn. The POLARBEAR-2 and the simons array experiments. *Journal of Low Temperature Physics*, 184(3-4):805–810, jan 2016.

[184] Peter Svrcek and Edward Witten. Axions in string theory. *Journal of High Energy Physics*, 2006(06):051–051, jun 2006.

[185] Takayuki Tamura, Ryo Iizuka, Yoshitomo Maeda, Kazuhisa Mitsuda, and Noriko Y. Yamasaki. An X-ray Spectroscopic Search for Dark Matter in the Perseus Cluster with Suzaku. *Publ. Astron. Soc. Jap.*, 67:23, 2015.

[186] The Simons Observatory Collaboration, Fabbian, Stephen Feeney, Simone Ferraro, Pedro Fluxà, Katherine Freese, Josef C. Frisch, Andrei Frolov, George Fuller, Brittany Fuzia, Nicholas Galitzki, Patricio A. Gallardo, Jose Tomas Galvez Ghersi, Jiansong Gao, Eric Gawiser, Martina Gerbino, Vera Gluscevic, Neil Goeckner-Wald, Joseph Golec, Sam Gordon, Megan Gralla, Daniel Green, Arpi Grigorian, John Groh, Chris Groppi, Yilun Guan, Jon E. Gudmundsson, Dongwon Han, Peter Hargrave, Masaya Hasegawa, Matthew Hasselfield, Makoto Hattori, Victor Haynes, Masashi Hazumi, Yizhou He, Erin Healy, Shawn W. Henderson, Carlos Hervias-Caimapo, Charles A. Hill, J. Colin Hill, Gene Hilton, Matt Hilton,

Adam D. Hincks, Gary Hinshaw, Renée Hložek, Shirley Ho, Shuay-Pwu Patty Ho, Logan Howe, Zhiqi Huang, Johannes Hubmayr, Kevin Huffenberger, John P. Hughes, Anna Ijjas, Margaret Ikape, Kent Irwin, Andrew H. Jaffe, Bhuvnesh Jain, Oliver Jeong, Daisuke Kaneko, Ethan D. Karpel, Nobuhiko Katayama, Brian Keating, Sarah S. Kernasovskiy, Reijo Keskitalo, Theodore Kisner, Kenji Kiuchi, Jeff Klein, Kenda Knowles, Brian Koopman, Arthur Kosowsky, Nicoletta Krachmalnicoff, Stephen E. Kuenstner, Chao-Lin Kuo, Akito Kusaka, Jacob Lashner, Adrian Lee, Eunseong Lee, David Leon, Jason S.-Y. Leung, Antony Lewis, Yaqiong Li, Zack Li, Michele Limon, Eric Linder, Carlos Lopez-Caraballo, Thibaut Louis, Lindsay Lowry, Marius Lungu, Mathew Madhavacheril, Daisy Mak, Felipe Maldonado, Hamdi Mani, Ben Mates, Frederick Matsuda, Loïc Maurin, Phil Mauskopf, Andrew May, Nialh McCallum, Chris McKenney, Jeff McMahon, P. Daniel Meerburg, Joel Meyers, Amber Miller, Mark Mirmelstein, Kavilan Moodley, Moritz Munchmeyer, Charles Munson, Sigurd Naess, Federico Nati, Martin Navaroli, Laura Newburgh, Ho Nam Nguyen, Michael Niemack, Haruki Nishino, John Orlowski-Scherer, Lyman Page, Bruce Partridge, Julien Peloton, Francesca Perrotta, Lucio Piccirillo, Giampaolo Pisano, Davide Poletti, Roberto Puddu, Giuseppe Puglisi, Chris Raum, Christian L. Reichardt, Mathieu Remazeilles, Yoel Rephaeli, Dominik Riechers, Felipe Rojas, Anirban Roy, Sharon Sadeh, Yuki Sakurai, Maria Salatino, Mayuri Sathyanarayana Rao, Emmanuel Schaan, Marcel Schmittfull, Neelima Sehgal, Joseph Seibert, Uros Seljak, Blake Sherwin, Meir Shimon, Carlos Sierra, Jonathan Sievers, Precious Sikhosana, Maximiliano Silva-Feaver, Sara M. Simon, Adrian Sinclair, Praween Siritanasak, Kendrick Smith, Stephen R. Smith, David Spergel, Suzanne T. Staggs, George Stein, Jason R. Stevens, Radek Stompor, Aritoki Suzuki, Osamu Tajima, Satoru Takakura, Grant Teply, Daniel B. Thomas, Ben Thorne, Robert Thornton, Hy Trac, Calvin Tsai, Carole Tucker, Joel Ullom, Sunny Vagnozzi, Alexander van Engelen, Jeff Van Lanen, Daniel D. Van Winkle, Eve M. Vavagiakis, Clara Vergès, Michael Vissers, Kasey Wagoner, Samantha Walker, Jon Ward, Ben Westbrook, Nathan Whitehorn, Jason Williams, Joel Williams, Edward J. Wollack, Zhilei Xu, Byeonghee Yu, Cyndia Yu, Fernando Zago, Hezi Zhang, and Ningfeng Zhu and. The simons observatory: science goals and forecasts. *Journal of Cosmology and Astroparticle Physics*, 2019(02):056–056, feb 2019.

[187] Tran Tsan, Nicholas Galitzki, Aamir M. Ali, Kam Arnold, Gabriele Coppi, Tamar Ervin, Logan Foote, Brian Keating, Jack Lashner, and Orlowski-Scherer et al. The effects of inclination on a two stage pulse tube cryocooler for use with a ground based Observatory. *Cryogenics*, 117:103323, July 2021.

[188] Sean Tulin and Hai-Bo Yu. Dark Matter Self-interactions and Small Scale Structure. *Phys. Rept.*, 730:1–57, 2018.

[189] Eve M. Vavagiakis, Zeeshan Ahmed, Aamir Ali, Kam Arnold, Jason Austermann, Sarah Marie Bruno, Steve K. Choi, Jake Connors, Nicholas F. Cothard, Simon Dicker, Brad Dober, Shannon Duff, Valentina Fanfani, Erin Healy, Shawn Henderson, Shuay-Pwu Patty Ho, Duc-Thuong Hoang, Gene Hilton, Johannes Hubmayr, Nicoletta Krachmalnicoff, Yaqiong Li, John Mates, Heather McCarrick, Federico Nati, Michael Niemack,

Maximiliano Silva-Feaver, Suzanne Staggs, Jason Stevens, Michael Vissers, Joel Ullom, Kasey Wagoner, Zhilei Xu, and Ningfeng Zhu. The Simons Observatory: Magnetic Sensitivity Measurements of Microwave SQUID Multiplexers. *arXiv e-prints*, page arXiv:2012.04532, December 2020.

[190] Tejaswi Venumadhav, Francis-Yan Cyr-Racine, Kevork N. Abazajian, and Christopher M. Hirata. Sterile neutrino dark matter: Weak interactions in the strong coupling epoch. *Phys. Rev. D*, 94(4):043515, 2016.

[191] Jones Reginald Victor and Richards J. C. S. The polarization of light by narrow slits. *Proc. R. Soc. Lond. A*, 225:122–135, 1954.

[192] Casey R. Watson, Zhi-Yuan Li, and Nicholas K. Polley. Constraining Sterile Neutrino Warm Dark Matter with Chandra Observations of the Andromeda Galaxy. *Journal of Cosmology and Astroparticle Physics*, 2012(03):018, 2012.

[193] Steven Weinberg. A new light boson? *Phys. Rev. Lett.*, 40:223–226, Jan 1978.

[194] Steven Weinberg. *Cosmology*. Oxford University Press, 2008.

[195] F. Wilczek. Problem of strong p and t invariance in the presence of instantons. *Phys. Rev. Lett.*, 40:279–282, Jan 1978.

[196] R. L. Workman and Others. Review of Particle Physics. *PTEP*, 2022:083C01, 2022.

[197] XRISM Science Team. Science with the x-ray imaging and spectroscopy mission (xrism), 2020.

[198] K. Yamada, B. Bixler, Y. Sakurai, P. C. Ashton, J. Sugiyama, K. Arnold, J. Begin, L. Corbett, S. Day-Weiss, and N. Galitzki et al. The Simons Observatory: Cryogenic half wave plate rotation mechanism for the small aperture telescopes, 2023. Submitted to RSI.

[199] Cyndia Yu, Zeeshan Ahmed, Josef C. Frisch, Shawn W. Henderson, Max Silva-Feaver, Kam Arnold, David Brown, Jake Connors, Ari J. Cukierman, J. Mitch D'Ewart, Bradley J. Dober, John E. Dusatko, Gunther Haller, Ryan Herbst, Gene C. Hilton, Johannes Hubmayr, Kent D. Irwin, Chao-Lin Kuo, John A. B. Mates, Larry Ruckman, Joel Ullom, Leila Vale, Daniel D. Van Winkle, Jesus Vasquez, and Edward Young. Slac microresonator rf (smurf) electronics: A tone-tracking readout system for superconducting microwave resonator arrays. *Review of Scientific Instruments*, 94(1), January 2023.

[200] Guan-Wen Yuan, Zi-Qing Xia, Chengfeng Tang, Yaqi Zhao, Yi-Fu Cai, Yifan Chen, Jing Shu, and Qiang Yuan. Testing the ALP-photon coupling with polarization measurements of Sagittarius A*. *Journal of Cosmology and Astroparticle Physics*, 2021(03):018, 2021.

[201] Hasan Yuksel, John F. Beacom, and Casey R. Watson. Strong Upper Limits on Sterile Neutrino Warm Dark Matter. *Phys. Rev. Lett.*, 101:121301, 2008.

[202] Hasan Yüksel and Matthew D. Kistler. Circumscribing late dark matter decays model-independently. *Physical Review D*, 78(2), July 2008.

[203] Ioana A. Zelko, Tommaso Treu, Kevork N. Abazajian, Daniel Gilman, Andrew J. Benson, Simon Birrer, Anna M. Nierenberg, and Alexander Kusenko. Constraints on Sterile Neutrino Models from Strong Gravitational Lensing, Milky Way Satellites, and the Lyman-α Forest. *Phys. Rev. Lett.*, 129(19):191301, 2022.